

Washington University in St. Louis

Washington University Open Scholarship

All Theses and Dissertations (ETDs)

1-1-2011

Quantitative Assessment of Lung Microstructure in Healthy Mice Using an MR-based ^3He Lung Morphometry Technique

Emir Osmanagic

Washington University in St. Louis

Follow this and additional works at: <https://openscholarship.wustl.edu/etd>

Recommended Citation

Osmanagic, Emir, "Quantitative Assessment of Lung Microstructure in Healthy Mice Using an MR-based ^3He Lung Morphometry Technique" (2011). *All Theses and Dissertations (ETDs)*. 629.

<https://openscholarship.wustl.edu/etd/629>

This Dissertation is brought to you for free and open access by Washington University Open Scholarship. It has been accepted for inclusion in All Theses and Dissertations (ETDs) by an authorized administrator of Washington University Open Scholarship. For more information, please contact digital@wumail.wustl.edu.

WASHINGTON UNIVERSITY IN ST. LOUIS
School of Engineering and Applied Science
Department of Electrical and Systems Engineering

Dissertation Examination Committee:

R. Martin Arthur, Chair
Mark S. Conradi
Jr-Shin Li
Robert E. Morley
Joseph A. O'Sullivan
Dmitriy A. Yablonskiy

Quantitative Assessment of Lung Microstructure in Healthy Mice Using an MR-based ^3He
Lung Morphometry Technique
by
Emir Osmanagić

A dissertation presented to the Graduate School of Arts and Sciences
of Washington University in partial fulfillment of the
requirements for the degree of

DOCTOR OF PHILOSOPHY

August 2011
Saint Louis, Missouri

copyright by

Emir Osmanagić

2011

ABSTRACT OF THE DISSERTATION

Quantitative Assessment of Lung Microstructure in Healthy Mice using an MR-based ^3He
Gas Lung Morphometry Technique

by

Emir Osmanagić

Doctor of Philosophy in Electrical Engineering

Washington University in St. Louis, July 2011

Research Advisor: Dmitriy Yablonskiy, PhD, Mallinckrodt Institute of Radiology, School of
Medicine

Academic Advisor: Martin Arthur, PhD, Electrical and Systems Engineering, School of
Engineering and Applied Science

Recently developed in our laboratory the MRI-based technique – ^3He Lung Morphometry – is a unique tool allowing *in vivo* measurements of lung microstructural parameters such as alveolar volume, surface-to-volume ratio and alveolar density. These parameters are commonly used by lung physiologists and pathologists but were previously available only from invasive biopsy studies. ^3He Lung Morphometry was originally developed for human studies but there is a need to expand it for studies of small animals like mice and rats that are used to advance our knowledge of lung physiology in health and disease and for development of drugs. Such an expansion of the ^3He Lung Morphometry technique is the subject of this dissertation. To achieve this goal we have developed a theory of ^3He gas diffusion in lung airways and alveoli and tested this theory in two distinct experiments.

In the first experiment, using a Stejskal-Tanner method, we examine the diffusion of ^3He atoms as it occurs in tiny airways of mouse lungs. Through a series of magnetic resonance (MR) measurements we study the pattern of signal decay over very short periods of time. This decay crucially depends on the confining effects of the spins in very small compartments, lung acinar airways and alveoli. The signal decay is mathematically modeled after the theory developed in our laboratory that describes ^3He gas diffusion in the compartments that are at the scale of mouse lung airways ($\sim 100 \mu\text{m}$). Applying our MR diffusion decay measurements in the mouse lung mathematical model allowed us to provide close estimation of lung microstructural parameters at the alveolar level. The values obtained for those parameters are in agreement with various histological findings published in the literature, as well as our own histological findings. These values are also in agreement with an *in vivo* mouse lung ^3He MR experiment also conducted in our laboratory.

Our theory of ^3He gas diffusion in lungs relies on an assumption that diffusion in the lung acinar airways is anisotropic. Thus, a set of experiments were performed to demonstrate that the gas diffusion in mouse lungs is indeed anisotropic. The MR measurements that demonstrate anisotropy of the ^3He gas diffusion in mouse lung also use a series of MR diffusion measurements. These MR measurements are directionally interrelated in such a way that the results unequivocally demonstrate diffusion anisotropy, one of the founding assumptions for our mathematical mouse lung model.

These two studies examined healthy lungs and allowed us to develop a robust and reliable tool to measure mouse lung parameters. We applied this tool and provided the first *in vivo* measurements of changes in lung microstructure that occur as a result of smoking.

Acknowledgements

First of all, I would like to express my gratitude to my Research Advisor, Dr. Dmitriy Yablonskiy, for his continued mentoring, patient and passionate teaching. Under his valuable guidance I had the chance and privilege to be a part of a great research team and work on many exciting research topics and have vastly expanded my horizons in understanding theoretical physics and applied mathematics. His knowledge and approach in applying it with a high rate of scientific professionalism is life-long inspiring.

I wish to thank the members of my dissertation committee, Research Co-Advisor Dr. R. Martin Arthur, Dr. Joseph O'Sullivan, Dr. Robert Morley and Dr. Jr-Shin Li for their time and constructive comments to improve the quality of this dissertation.

I cannot forget to thank Dr. Alex Sukstanskii for his relentless exploration of best mathematical models and theoretical approaches in setting up experiments to test scientific hypothesis. Dr. James Quirk was a constant help of large magnitude in onboarding me to navigate through all the equipment as well as understanding the physics behind NMR/MRI. Both Dr. Joel Garbow and Dr. James Quirk have been a major part in my transition from theory to practice on the MRI scanner.

Through my PhD journey, I'd like to thank Dr. Mark Conradi, Dr. Jason Woods, and Dr. Joseph O'Sullivan as they provided me with the opportunity to learn from the best, and to develop needed scientific rigor - I am grateful to them. I would also like to thank all the staff members of the School of Medicine Department of Radiology and the Electrical & Systems Engineering Department at Washington University for their time, guidance and help.

The students I worked with and shared thoughts and challenges with played an important role in the development and execution of the ideas that contributed to this work.

Last but not least, my sincere gratitude goes to my family, my parents Ibrahim i Muša, my wife Kimberly and sons Kenan and Aldin, for their endless love and unconditional support. This dissertation is dedicated to them.

Emir Osmanagić

Washington University in Saint Louis
July 2011

Contents

ABSTRACT OF THE DISSERTATION	ii
Acknowledgements	v
Contents	vi
List of Tables	ix
List of Figures	xi
List of Abbreviations	xxii
List of Notations	xxiii
Chapter 1 - Introduction.....	1
1.1 Project Overview and Aims	1
1.2 Conventional and Hyperpolarized ^3He Magnetic Resonance Imaging	5
1.3 ^3He Gas Apparent Diffusion Coefficient in Mouse Lungs.....	7
1.4 Hyperpolarized ^3He Measurements in Mouse Lungs.....	8
1.5 Main Project Steps	10
1.6 Dissertation Overview.....	12
1.7 References	16
Chapter 2 - Physics of Magnetic Resonance Imaging with Hyperpolarized ^3He.....	19
2.1 Theoretical Nuclear Spin Physics.....	19
2.1.1 Nuclear Spins in Magnetic Fields	19
2.1.2 Hyperpolarization	21
2.2 Spin Exchange – Optical Polarization of ^3He Gas.....	22
2.2.1 Optical Pumping of Rubidium Electrons	23
2.2.2 Polarization Transfer from Rb to ^3He	25
2.3 Design of a HP ^3He MRI Diffusion Experiment: Critical Components	26
2.3.1 RF Coil and Tuning Box	27
2.3.2 Flip Angle.....	30
2.6 References	32
Chapter 3 - Materials and Methods: MR Diffusion Procedure for Mouse Lungs	33
3.1 MR Measurements of Lung Microstructure	33
3.1.1 MR Diffusion Experiment	34
3.1.2 Gradient relationship to b-value.....	37
3.1.3 Theory of Gas Diffusion in Mouse Lungs.....	39

3.1.4 Diffusion Anisotropy in the Lung Model.....	43
3.2 SNR Optimization of MR in Mouse Lungs	46
3.3 References	48
Chapter 4 - Materials and Methods: Hyperpolarized ³He Gas Delivery	49
4.1 Delivery of ³ He Gas.....	49
4.1.1 Gas Delivery Apparatus.....	49
4.1.2 Delivery Method and practice.....	51
4.2 Animal Preparation	54
4.2.1 Animal surgery to remove lungs.....	54
4.2.2 Intubating lungs, fixing in the coil.....	56
4.2.3 Problems incurred during animal procedures	57
4.3 References	59
Chapter 5 - Materials and Methods: Gradients Calibration, Eddy Currents and RF Coil	60
5.1 Varian MRI System	60
5.2 Gradient Pick-up Coil and Oscilloscope	60
5.3 External Tuning Box	65
5.4 Eddy Currents.....	67
5.5 RF Coil for ³ He.....	72
5.5.1 Network Analyzer.....	74
5.6 Polarization Equipment for ³ He	75
5.6.1 Hyperpolarizing Hardware.....	75
5.6.1 Controls and Diagnostics	77
5.7 References	79
Chapter 6 - Mouse Lung MR Diffusion Experiment	80
6.1 MR Diffusion Experiment.....	80
6.1.1 Bi-Polar Stejskal-Tanner Sequence for Diffusion Measurements	80
6.1.2 b-values and Diffusion Gradient Direction.....	82
6.1.3 Residual Magnetization	84
6.1.4 Diffusion Pulse Sequence Details	85
6.2 MR Experiment for Anisotropy.....	87
6.2.1 Pulse Sequence.....	87
6.2.2 b-values	89
6.2.3 Anisotropy Sequence Details	90
6.3 MR Data Processing	92
6.4 References	100
Chapter 7 - Summary of Results	101
7.1 MR Measurements of Key Lung Parameters	101
7.2 MR Measurements of Lung Anisotropy	108
7.3 Results from <i>in vivo</i> Studies	111
7.4 References	115

Chapter 8 - Conclusion	117
8.1 Accomplishments.....	117
8.1.1 Mouse Lung Microstructure Measurements.....	117
8.1.2 Anisotropic Nature of Mouse Lungs.....	117
8.1.3 Adaptive MR Sequence for Optimal use of Gradient Budget.....	118
8.2 Directions for Future Study.....	118
8.2.1 Known Experiment Limitations	118
8.2.2 This Study and Future Work.....	119
8.3 References	121
Appendix A - Source Code for Flip Angle and Eddy Currents Measurements.....	122
A1 Flip Angle Measurement and Calibration.....	122
A2 Eddy Current Pulse Sequence.....	122
Appendix B - Source Code for Lung Microstructure and Anisotropy Experiments.	132
B1 Pulse Sequence for Determining Mouse Lung Microstructure.....	132
B2 Pulse Sequence for Demonstrating Anisotropy	141
Vita	150

List of Tables

Table 4.1: The block diagram of MRI-compatible (with the exception of the low-pressure pressure gauge), manual ^3He gas delivery six-valve apparatus. The purpose is to purge the lungs of air multiple times using ^3He (at thermal equilibrium). After that, the lungs are filled with the HP ^3He gas first and topped with $\sim 150 \mu\text{l}$ of N_2 for the NMR measurement of diffusion. The 180 cm long line keeps the pressure gauge containing ferromagnetic parts out of the scanner's fringe field.53

Table 4.2: The CL57BL/6N mouse strain, euthanized and secured on the surgery table: after the light anesthetic, the mouse is delivered an over dose of Ketamine cocktail (0.15 ml of Xylazine, 1.0 ml of Ketamine and 4.6 ml of sterile saline) and euthanized. The animal is ready for the lungs to be extracted and intubated with a plastic needle.55

Table 6.1: The comprehensive list of sequence parameters used for acquiring lung diffusion data, used for estimation of the lung internal physical parameters.86

Table 6.2: Comprehensive list of anisotropy sequence parameters used for acquiring lung diffusion data after applying successive gradients, used for establishing the link between the anisotropy of the diffusion and the lung tissue.90

Table 7.1: Summary of geometrical and diffusion parameters from excised lungs of six mice. The table gives values of key parameters in our model: major airway radius R , the depth of alveolar sleeve h , alveolar surface-to-volume ratio S/V , mean chord length L_m and alveolar density N_a , where the error bars are the fit uncertainties. Average diffusion along and perpendicular to the airways is $0.7 \text{ cm}^2/\text{s}$ and $0.0143 \text{ cm}^2/\text{s}$,

respectively. Both diffusion parameters, D_L and D_T are sharply reduced from ^3He free diffusion ($D_0=1.76 \text{ cm}^2/\text{s}$) as the alveolar ducts and walls present obstacles to diffusing ^3He atoms. Quantity β_L is kurtosis factor for longitudinal diffusivity.102

Table 7.2: Morphometric data from microscopic studies from various literature sources obtained by stereological analysis of mouse lungs using animals of different strain, age and size. The measured lung volumes varied by a factor of 3, some of which may be due to different inflation levels achieved in fixation.103

Table 7.3: Summary of morphometric parameters obtained via ^3He MRI from 7 normal mice with histological comparison (not available for mice 6 and 7). The table gives values of key parameters for our model: acinar airway radius R , alveolar depth b , mean linear intercept L_m , alveolar density Na and alveolar surface-to-volume ratio S/V . Since there is not much variation from slice to slice in the same mouse, only mean values of the parameters for each mouse are shown here.114

List of Figures

Figure 2.1: Illustrative comparison of Thermal (Boltzmann) equilibrium of several ppm polarization of ^3He gas (nuclear spin number $I=1/2$) versus the high level of nuclear spin polarization reached by optical pumping, $\sim 40\%$	22
Figure 2.2: Vaporized Rb illuminated using circularly polarized laser light. The light excites the electron transitions from $5s_{1/2}$ ground state into $5p_{1/2}$ excited state. Collisional mixing provides near even re-population of both sub-levels of the excited state. Electrons falling into $m=-1/2$ excited state sub-level eventually decay to the ground state where they are re-pumped, resulting in extremely high polarization of Rb electrons into $m=1/2$ state.....	24
Figure 2.3: Polarization transfer process during binary collisions of the ^3He nuclei and Rb electrons. Spin polarization is continuously exchanged leaving the Rb electron spin-down while the ^3He nuclei get hyperpolarized.....	25
Figure 2.4: Typical RF coil can be represented as a series connection of R-L-C oscillating at the resonant angular frequency ω	27
Figure 2.5: When tuning box placed between the RF coil and the amplifier, the equivalent schematic looks as shown, resonant circuitry for dual frequency is a parallel L-C circuit in series with the connection of R-L-C circuitry.....	29
Figure 2.6: The schematic shows typical RF RLC resonant circuit inductively coupled to RF amplifier.	29

Figure 2.7: The magnetization, M , precesses about the Z axis with the tip angle α , and it is divided into the longitudinal component, M_z and transverse component, M_{xy} . A RF coil is placed in the Y axis direction to collect the MR signal.....31

Figure 3.1: Schematic structure of an acinar airway with eight alveoli distributed along the annular ring (eight-alveolar model). Left is a cross section of the airway perpendicular to its length and the right is a cross section along the length of the airway. Each airway (duct or sac) can be considered geometrically as a cylindrical object consisting of an alveolar sleeve with alveoli opening toward the internal cylindrical air passage. The diagram defines inner (r) and outer (R) airway radii (as in Fig. 1 in [4] and [2]) and the depth of the alveolar sleeves (b). The ratio $L=0.765*R$ is chosen so that the alveolar size is the same along the airway and along the circumference [3]. The shaded area shows lung air volume per alveolus V_a that comprises both the volume of alveolus proper and the immediately associated duct volume.....34

Figure 3.2: Bi-polar pulsed gradients. Stejskal-Tanner were first to propose the idea of measuring restricted diffusion by varying the Δ between gradient pulses.....36

Figure 3.3: Gradient slew rate (time τ) is dynamically controlled to satisfy Equation (3.4) and not to exceed maximum hardware capabilities.....38

Figure 3.4: Weibel's lung model [7] [8] (based on biological structure), shown as branching acinar airways, covered with alveolar sleeve of depth $R-r$. Diffusion calculations and mathematical model is based on this lung model.40

Figure 3.5: The sequence in (a) has three consecutive bi-polar gradients along the x axis, referred to as the XXX sequence, exploiting only diffusion along the X axis.

Similarly, the sequence in (b) is the XYZ sequence, and exploits diffusion along all three spatial axes.44

Figure 3.6: If alveolar structure in the lungs can be mimicked as a series of spherical compartments of various sizes, (a), the diffusion in all directions will be equal. If lung microstructure is modeled as cylinders (acinar airways), as in (b), the diffusion will be anisotropic.45

Figure 4.1: The block diagram of MRI-compatible (with the exception of the low-pressure pressure gauge), manual ^3He gas delivery six-valve apparatus. The purpose is to allow the lungs to be purged of air multiple times using N_2 and then filled with the ^3He for the NMR measurement of diffusion. The 180 cm long line keeps the pressure gauge containing ferromagnetic parts out of the scanner's fringe field.50

Figure 4.2: The ^3He gas, six-valve delivery apparatus. The image shows manifold with three color-coded valves (as described in the block diagram), the plastic cannula connected with the lung valve, long line to connect the low pressure gauge and the Tedlar bag connected with the bag valve.51

Figure 4.3: On the left hand side is freshly extracted mouse lungs with heart and all excess tissue removed. Size relation to a US quarter demonstrates the challenge of size when working with mouse lungs. On the right hand side, the same lung intubated, double ligated, and inflated with 1 ml of air, approximately the total volume of mouse lungs.56

Figure 5.1: Home-built gradient pick up coil. The two pairs of coils are offset spatially along the Z axis (along the cylinder) while the other pair is offset in a perpendicular direction. The Z-gradient is obtained from Z (Z1 and Z2) coil-pair, while X- or Y-

gradient are obtained from the Y (Y1 and Y2), coil pair, depending on a physical alignment of the Y coil pair inside the magnet bore, either with X axis or with the Y axis. Due to this nature of the design of the gradient coil, and given the two channel amplification in the accompanied electronic box (see Figure 5.2), one could simultaneously observe Z-X or Z-Y gradients.....61

Figure 5.2: Electronic schematic of the circuitry that processes signal from one pair of gradient coils. There are two identical circuits in the electronic box, for both gradient coil pairs. In principle, L1 and L2 can represent Z1 and Z2 of Y1 and Y2 from Figure 5.1.62

Figure 5.3: The rise times of gradient pulses through the entire range of gradient strengths. Results were identical for all three axes as for the negative gradient amplitudes. The solid curve is a fit to the data with the linear expression shown.63

Figure 5.4: Images show the gradient pulse shapes for various rise times for X axis. Results demonstrate an excellent slope control, no ringing and the identical fall. The other two axes, Y, and Z, exhibited identical gradient pulse shapes. Some of the curvature can be noticed in the first image (top left) at the end of the fall cycle. The amount of the curvature is negligible to make a difference in our calculations. Additionally, this is the image obtained for the maximum slew rate, which we never use in our sequence, e.g. we always force the slope, particularly we used rise times in order of 100-200 μ s.....64

Figure 5.5: The bi-polar gradient transition region behaves well: gradient follows the prescribed waveform for both, positive and negative side. The gradient moves through the transition points without ringing or soft corners, allowing us to apply the

mathematical theory for the gas diffusion in lungs with the required accuracy and confidence in results.....65

Figure 5.6: External tuning box, consisting of one inductor and two capacitors, one fixed one adjustable. The adjustable capacitor is there to tune the box to the right resonance, in this case the frequency of proton (^1H).....66

Figure 5.7: Images a-d are coronal mouse proton images, obtained using ^3He RF coil with the external tuning box connected in series, effectively re-tuning the RF coil to the proton frequency. These images are used to locate the lung cavity. The image e is the ^3He gas image of the same mouse lungs in the transverse plane, obtained using the same RF ^3He coil. All imaging planes are cited with the respect to the magnet bore.67

Figure 5.8: Image a shows the sequence used to explore eddy current effect while changing the ramp up/ramp down time of the gradient pulse, $grise$ [ms] =125, 150, 175, 200, 225, 250, 275, 300, 325, 350, followed by a fixed $d2=3$ ms delay and $150 \mu\text{s}$ RF pulse. Image b shows the MR signal for the ten RF pulses. Image c shows the result of the same sequence, now with the RF pulse of 50 ms. Image d employs the sequence with 3 s long RF pulse and reveals no eddy current effect. Images b, c, and d look exactly the same for X, Y and Z direction.....69

Figure 5.9: Similar to Figure 5.8, image a shows the sequence used to explore eddy current effect while changing the ramp up/ramp down time of the bi-polar gradient pulses, $grise$ [ms] =125, 150, 175, 200, 225, 250, 275, 300, 325, 350, followed by a fixed $d2=3$ ms delay and $150 \mu\text{s}$ RF pulse. Image b shows the MR signal for the ten RF pulses. Image c shows the result of the same sequence, now with the RF pulse of 50 ms.

Image d employs the sequence with 3 seconds long RF pulse and reveals no eddy current effect. All MR signal images look identical for all three axes: X, Y and Z.....70

Figure 5.10: As before, image a shows the sequence used to explore eddy current effect while changing the $d2$ delay (3, 10, 50, 100, 150, 300, 600, 1000, 2000, 3000 ms), followed by a 10 μ s RF pulse and a 300 ms acquisition. Image b shows the MR signal for the ten RF pulses in X direction. Image c shows the result of the same sequence, now with in Y direction and d shows the Z direction.71

Figure 5.11: Image a shows sequence with fixed rise-time bi-polar gradients with changing the $d2$ delay (3, 10, 50, 100, 150, 300, 600, 1000, 2000, 3000 ms), followed by a 150 μ s RF pulse and a 200 ms acquisition. Image b shows the MR signal for the ten RF pulses in X direction. Image c shows the result of the same sequence, now with in Y direction and d shows the Z direction.....72

Figure 5.12: The lab-built RF coil, tuned to ^3He nuclei frequency. The coil consists of four copper plates acting as inductors connected in series with capacitors: three fixed and one adjustable capacitor. The RF coil is inductively coupled to RF amplifier using a LC circuitry: a single loop (L) terminated with a capacitor (C). The coupling is adjusted using both, the adjustable coupling capacitor and distance between the loop and the RF coil.....73

Figure 5.13: Network Analyzer, HP 8720A, used to tune the RF coil to the ^3He nuclei frequency and to adjust the inductive coupling, with the load present in the coil.....75

Figure 5.14: Schematic diagram of the laser source (diode array) that emits linearly polarized laser light, series of collimating lenses (to focus the light at infinity, to make the laser rays collinear) after which it is passed through the $1/4\lambda$ plate to make the light

polarization circular. This light irradiates the cell with ^3He and Rb vapor. A fan circulates warm air around the cell in a chamber, to elevate its temperature to 170°C . The chamber is located between two Helmholtz coils that generate nearly homogeneous magnetic field.76

Figure 5.15: The commercial GE polarizer with its key components boxed in red. The control PC runs the laser diode array, measures the light absorption, its wavelength and can inspect the polarization level.78

Figure 6.1: The bi-polar diffusion sensitizing gradient sequence used in all diffusion MR measurements. The sequence is run 12 times back to back for different b-values ($b[\text{s}/\text{cm}^2]=0, 10, 9, 8, 7, 6, 5, 4, 3, 2, 1, 0$). The purple italics denote main sequence parts: crusher gradients followed by the RF pulse and the bi-polar set of gradients, only in one axial direction for one 12-sequence set.....82

Figure 6.2: A set of typical 12 MR signals collected from the b-value descending sequence for $b[\text{s}/\text{cm}^2]=0, 10, 9, \dots, 2, 1, 0$. The first and the last pulse of $b=0$ value are used to calculate actual flip angle α83

Figure 6.3: The X, Y, Z diffusion sensitizing gradient sequence used in all anisotropy MR experiments. The sequence utilized the descending set of b-values, $b[\text{s}/\text{cm}^2]=0, 4, 3, 2, 1, 0$. The purple italics denote the main sequence parts: crusher gradients followed by the RF pulse and all three consecutive bi-polar gradients, X, Y and Z.....88

Figure 6.4: The X, X, X anisotropy sequence. The graph is for illustration purpose of the three consecutive uni-axial gradients. The sequence otherwise has the same timings and works in tandem with X, Y, Z sequence to confirm the anisotropy of the gas diffusion in mouse lungs. The purple italics denote the main sequence parts: crusher

gradients followed by the RF pulse and the set of three bi-polar gradients all applied in one axial direction, X direction.89

Figure 6.5: MR signal obtained by shimming on the water phantom with the volume similar to inflated mouse lungs, 17 mm in diameter. Very narrow Lorentzian signal has the width of less than 20 Hz.92

Figure 6.6: A broad MR signal with many peaks (lungs inside chest cavity make for very inhomogeneous magnetic field). The full scale is 3000 Hz wide, and shows real part of the signal. The MR signal from excised lungs, shown at the same frequency scale, 3000 Hz, was of much better shape (see Figure 6.8) and SNR.93

Figure 6.7: A typical FID signal collected for 50 ms, immediately after the RF excitation pulse and the Stejskal-Tanner gradients in our sequence, 5000 real and 500 imaginary data points. The red line is the real while the blue is imaginary part of the MR signal.94

Figure 6.8: After the FID signal is passed through the FFT transform, the spectral signal is obtained. The tails of the signal never go to zero due to noise floor level, making it hard or impossible to calculate the area under the curve in a meaningful way. The horizontal axis is 3000 Hz wide, same as Figure 6.6. Signal obtained from the excised lungs is about twice as narrow with vastly improved SNR, in this case around three times. The deviation of this curve from a Lorentzian behavior seen in Figure 6.5 is due to imperfect shimming and the specific structure reflects the distribution of field inhomogeneities.95

Figure 6.9: The line on the bottom represents an original MR spectrum; line in the middle is its Bayesian representation (using three Bayesian resonances), while the first line is

the residual between the two signals: original MR signal and its Bayesian representation.....96

Figure 6.10: Original MR signal (arbitrary units) amplitude, using the order of b-values as they were collected in the experiment, in $[s/cm^2]$. Two $b=0$ signals, at the beginning and the end of the sequence, have different amplitudes as polarization is consumed by RF pulses during the measurement. These two signals are used to determine the RF pulse flip angle for later correction of the amplitudes. Dotted line shows the signal decay path that would occur in case of no gradients, all $b=0$97

Figure 6.11: Typical dependence of adjusted MR signal amplitude (logarithmic scale) on b-value (symbols) and the fitting curves (solid lines) for X, Y, Z and their average. Results demonstrate an excellent fit with $\chi^2=0.045$. A very important feature is the substantial deviation from mono-exponential behavior (deviation from straight line), in agreement with theoretical prediction, in [1] and the theory presented in this paper.98

Figure 6.12: The figure gives a complete data processing path spanning the MR experiment until the data are ready for the curve fitting and lung physical parameters extraction.99

Figure 7.1: (A, left) Scanning electron micrograph of segment of a partly dissected silicone-rubber cast of an acinus of a mouse lung showing the transitional bronchiole (trb) as entrance airway and alveoli (a) grouped around alveolar ducts which have been partly separated. Asterisk marks a transected alveolar duct with diameter $2r$. Bars mark approximate outer diameter $2R$. (B, right) Scanning electron micrograph of a perfusion-fixed mouse lung air-inflated to about 60% TLC showing a transitional bronchiole (trb) that opens into the acinus (arrow). Double-pointed arrows mark the

inner diameter $2r$ of alveolar ducts that are wide in the first generations of branching and taper somewhat towards the periphery; the bar marks the outer diameter $2R$ that comprises the sleeve of alveoli (a). Range of measured values: $R = 70\text{-}100\ \mu\text{m}$. $r = 40\text{-}75\ \mu\text{m}$, $b = 30\text{-}55\ \mu\text{m}$105

Figure 7.2: Raw data are shown in the order they were acquired. After the first $b=0$ acquisition, the descending order of b-values was chosen to better use the naturally decreasing SNR in ^3He gas experiments: apply the large b-values first while the ^3He gas has strong polarization and apply the weakest b-values last.....109

Figure 7.3: Typical XYZ and XXX data comparison for one mouse lungs. The S_{xxx} stays above S_{xyz} throughout the range of different b-values used in the experiment. This consistent inconsistency indeed demonstrates the ^3He gas diffusion anisotropy at the microscopic level in the mouse lungs.110

Figure 7.4: Summary of comparison of S_{xxx} and S_{xyz} signals for all six mice, as in Table 7.1, for the anisotropy experiment. MR signal S_{xxx} is consistently higher than S_{xyz} for all scanned b-values, demonstrating the gas diffusion anisotropy in the mouse lungs, due to the cylindrical shape of airways in the mouse lungs.111

Figure 7.5: a: Representative geometric parameter (R , b , and L_m) maps obtained from one healthy mouse lung. Major airways are red in the maps of R . The pixel size is $0.63\ \text{mm} \times 0.63\ \text{mm}$ and slice thickness is $2\ \text{mm}$. The slightly elevated R and L_m values in the ventral and dorsal lung periphery are fairly consistent from mouse to mouse. **b:** corresponding ^1H images showing anatomical positions. **c:** Corresponding HP ^3He ventilation images ($b=0$)113

List of Abbreviations

ADC	Apparent Diffusion Coefficient
BALB	Bagg Albino (inbred mouse strain)
FFT	Fast Fourier Transform
FID	Free Induction Decay
GE	Gradient Echo
HP ^3He	Hyperpolarized ^3He
MRI	Magnetic Resonance Imaging
MR	Magnetic Resonance
NMR	Nuclear Magnetic Resonance
RF	Radio Frequency
RLC	Resistor, Inductor, Capacitor
SNR	Signal to Noise Ratio
Std dev	Standard deviation
TLC	Total Lung Capacity
VnmrJ	Varian NMR System Software in Java

List of Notations

b	b-value, closely related to gradient strength and its waveform
B_0	main magnetic field, generated by NMR/MRI
B_1	RF field, perpendicular to B_0
D	diffusion coefficient
G	gradient strength
h	depth of alveolar sleeve
j	lower case j denotes imaginary quantity
L	alveolar diameter
L_m	mean chord length
M	magnetization
N_a	number of alveoli
P	polarization
R	lung acinar airway outer radii
r	lung acinar airway inner radii
S	MR echo signal
S/V	surface over volume ratio
T_1	spin's longitudinal relaxation time constant in FID
T_2^*	spin's transverse relaxation time constant in FID
Z	Impedance
$5s_{1/2}$	Rb electron ground state
$5p_{1/2}$	Rb electron excited state
α	nuclear spin flip angle
β_L	kurtosis factor for longitudinal diffusivity
γ	gyromagnetic ratio
Φ	error function
k_B	Boltzmann's constant
$\lambda/4$	quarter-wave
μ	non-zero magnetic moment, micro
\hbar	Planck constant
χ^2	Chi-squared test for goodness of fit

Chapter 1 - Introduction

1.1 Project Overview and Aims

The efficiency of oxygen delivery through the lung airspaces to the blood vessel network occupying the alveolar walls depends mostly on the structure, integrity and functioning of the pulmonary acinar airways. The morphometry of the pulmonary acinus, both in health and disease, has been studied in numerous publications. These studies provided invaluable information on lung microstructure that is the basis of the current knowledge on the lung structure and function (see for example [1-5]). Understanding changes in lung microstructure in different illnesses is crucial for phenotyping disease progression and developing new medicines. One of the lung diseases that is mostly related to changes in lung alveolation and affects millions of Americans and people worldwide is emphysema.

The study of lung emphysema dates back to the beginning of the 17th century. Nevertheless, a number of important questions remain unanswered because a quantitative localized characterization of emphysema requires knowledge of lung structure at the alveolar level in the intact living lung [6]. Lung stereology, the extraction of the lung spatial geometry from two dimensional planar sections of biopsied tissue, is considered the “gold standard” for the lung morphometry [7]; however its clinical applications are limited by its invasive nature. The introduction of hyperpolarized gas MR [8, 9] has opened the door to applications for which gaseous agents are uniquely suited, such as lung magnetic resonance imaging (MRI) [10]. One direction in hyperpolarized ^3He gas MRI is lung morphometry that is based on measuring the random atomic motion (diffusion) of ^3He gas that is inhaled by a subject. To

diffusing ^3He atoms, the alveolar walls, alveolar ducts, sacs and respiratory bronchioles serve as obstacles - they reduce and restrict the ^3He gas diffusivity. Thus, the measured atomic diffusion strongly relates to the lung microstructure. Already initial publications [6, 11-13] have demonstrated that the apparent diffusion coefficient (ADC) of hyperpolarized ^3He gas in the lungs is much smaller than in the free space but dramatically increases in emphysema, suggesting a large potential as a diagnostic tool for clinical applications.

While very encouraging, the ^3He gas ADC measurements substantially depend on the details of the technique that is used in the MR experiments. Also, ADC does not provide direct measurement of lung geometrical parameters, even though ADC showed correlation with direct morphometric measurements in rats [14, 15], humans [16] and rabbits [17]. The ^3He gas lung morphometry technique developed in our laboratory by Yablonskiy and colleagues [6, 18, 19] allows MRI-based diffusion measurements to provide unique *in vivo* information on the lung microstructure at the alveolar level: 3D tomographic images of such geometrical parameters as mean airspace chord length (L_m), lung parenchyma surface-to-volume ratio (S/V) and the number of alveoli per unit lung volume (Na) can be estimated from a rather short (several seconds) MRI scan. These parameters are most commonly used by lung physiologists to characterize lung morphometry [7] but were not previously available from *in vivo* studies.

To date, the ^3He gas lung morphometry technique with hyperpolarized ^3He gas diffusion MRI has been developed and exploited for human lungs [19]. In this study we further develop and use the ^3He gas lung morphometry to study lungs in mice. As mouse lungs have vastly smaller physical parameters, this requires modification of the theoretical equations that

relate MRI diffusion measurements to lung microstructural parameters [19]. While the general MRI morphometry theory remains valid, the specific relationships between lung microstructure parameters and diffusion attenuated MR signal must be modified for parameters of mouse lungs, which is one of the objectives of this study. Thus, one of the goals of this work is to take the theoretical model used in human lung experiments and generalize it for the small physical size of mouse lung airways. Also because the length of the acinar airways in mouse lung is much shorter than in humans, the diffusion gradient encoding duration should be shortened to minimize effects of ^3He atoms escaping into adjoining airways and distorting the lung morphometry measurements. The mathematical gas diffusion model for the human lungs cannot simply be scaled down for the mouse lungs as number of physical parameters differ in a non-linear fashion and different gradient pulses will be used. In this study we use very short bipolar diffusion sensitizing gradient pulses ($\Delta t=440 \mu\text{s}$), as compared to $1800 \mu\text{s}$ in human experiments.

To achieve the overall goal of non-invasively obtaining mouse lung microstructure parameters comparable to those obtained using direct method (histology), we pursued the following specific aims:

AIM 1. To Develop Animal Model And Lung Scanning Protocol

The core of this aim is to develop an animal scanning model to study lung microstructure using MRI techniques described in [6] and [18] to measure the lung physical parameters based on *in vivo* lung morphometry technique proposed by Sukstanskii and Yablonskiy [18, 20].

Previous studies used an *in vivo* model which, due to the lung dimensions and the limiting factors imposed by hyperpolarized ^3He gas, introduced various motion artifacts. To eliminate them and focus specifically on the lung, an object of this study is an MR experiment on the lungs of a freshly sacrificed animal. Using this model, a number of variables are contemplated and tested: scanning lungs in the chest cavity or excised, oral vs. tracheal intubations, age of the animals, size, period between intubation and data collection, various purging techniques, suppressing the ^3He gas MR signal from large airways, various ^3He gas delivery techniques as well as the tradeoff between the richness of the ^3He gas mixture, lung airway sizes, diffusion speed in the lungs and the administration of diffusion weighing (b-values) MR pulse sequence.

AIM 2. To Determine Lung Microstructure Using The ^3He Morphometry Technique

The objective here is to establish lung morphometry parameters for normal (non-diseased) lungs, to measure the lung microstructure and to compare it with the histology Lm method using fifteen freshly sacrificed mice. The Lm , or Mean Linear Intercept method, is a standard histology measurement technique used to quantify the average size of alveoli [20].

To quantify lung morphological parameters from the diffusion measurements on the acinar level in healthy mice, we have developed and/or adapted a number of data processing mathematical methods and tools. Namely, to assess the MR signal strength, we use a Bayesian Analysis software package to describe the frequency spectral data. The mathematical model developed in [6] and subsequently optimized for the mouse lungs is used in a mathematical analysis software package to curve fit sets of MR diffusion data to extract morphometric parameters.

AIM 3. To Validate MR measurements Through Histology in Mice With Emphysema

The final objective is to establish lung morphometry parameters for emphysema diseased lung, to measure its microstructure and to compare it with the histology *Lm* method using freshly sacrificed mice. As in the previous aim, to attain this objective, a diseased lungs model with smoking-induced emphysema will be used.

1.2 Conventional and Hyperpolarized ^3He Magnetic Resonance Imaging

Conventional MRI uses the water hydrogen nuclei present in the body as a signal source. The low density of the lung (tissue of the lung comprises only 10-20% of the lung volume) drastically reduces the nuclear spin density making conventional MRI of lungs very difficult [11]. Spin density is defined as the number of nuclei per volume that will provide an MRI signal when excited by an RF pulse of the resonant frequency of the imaged nuclei for a given strength of the permanent magnetic field. The MRI signal is proportional to the spin density, thus imaging low density tissue results in a poor MRI signal. Additionally, any magnetic field inhomogeneities across the lung will negatively affect the measured MRI signal. These inhomogeneities are due to the magnetic susceptibility difference at the boundaries between lung tissue and gas in lungs. These inhomogeneities will have pronounced effect for small samples as mouse lungs where strong gradients have to be applied to obtain the MR data.

Applying MR principles to hyperpolarized ^3He gas inhaled into the lungs allows direct imaging of the airspaces in the lungs. The hyperpolarized ^3He MRI of the lungs is a non-invasive, non-destructive and relatively safe technique. It utilizes the high spin polarization of laser-polarized ^3He gas to generate a strong MR signal of the gas delivered to the lung airways. As opposed to the conventional MRI method, in which we image the lung tissue itself, the hyperpolarized ^3He gas MR images gas within the lungs. This method allows for MR examination of the lung internal microstructure, its ventilation as well as time-dependent studies to observe changes.

The process of hyperpolarization is a spin-exchange technique [21] using a commercial polarizer to achieve polarization levels of approximately 40%. The spin density of the ^3He gas is approximately 2,500 times less than that of water ^1H protons; however, the ^3He gas can be hyperpolarized to approximately 100,000 times the spin polarization of the thermal equilibrium. Although this compensates for the low-spin density of the ^3He gas, the hyperpolarization is a non-equilibrium state and the polarization level decreases rapidly due to various mechanisms in the process of creation, dispensing, transportation and delivery of the gas. Even so, the remaining ^3He gas polarization, if quickly delivered, provides more than adequate signal-to-noise ratio (SNR). It is important to note that this technique does not detect tissue (as the solubility of the ^3He gas is very low) but detects hyperpolarized ^3He gas only in the ventilated airways of the lungs. In the MR images tissue will appear as dark regions, while high-spin density regions from hyperpolarized ^3He gas will appear as bright regions.

As stated earlier, the highly polarized state is not an equilibrium (stable) state and each RF pulse will result in an unrecoverable signal loss. Polarization will also degrade over a period of time, thus proximity of the polarizing hardware is beneficial. The ^3He gas is scarce, expensive and slow to polarize. Hence, special MR protocols should be used to address these specific details of hyperpolarized gas MRI.

1.3 ^3He Gas Apparent Diffusion Coefficient in Mouse Lungs

Initial studies in humans and rats [6, 11-13, 22] have shown the correlation between the internal lung microstructure and the apparent diffusion coefficient (ADC) of the hyperpolarized ^3He gas in the lungs. Diffusion here is described as traditional Brownian motion of the gas atoms in the lungs and denoted as D – diffusion coefficient. For ^3He diffusion in ^3He gas, the free diffusion coefficient is $1.8 \pm 0.2 \text{ cm}^2/\text{s}$ [23, 24] and for the observing diffusion time interval t , the diffusing ^3He atoms will on average move

$$x_{rms} = \sqrt{2Dt} \tag{1.1}$$

If diffusion is measured in the presence of gases other than ^3He gas, this diffusion will take a different value and will be modified by the amount and type of other gases [25].

Mouse lungs are highly restrictive to gas diffusion: the obstacles result in reduction of the diffusion coefficient being measured using MR technique. This measure of reduced diffusion is known as the apparent diffusion coefficient (ADC).

As alveolar walls, alveolar ducts, sacs and respiratory bronchioles serve as obstacles to the path of the diffusing ^3He atoms, they reduce and restrict the ^3He gas diffusivity. Thus, there should be a strong correlation between the measured atomic diffusion and underlying lung microstructure.

In essence, we should be able to link changes in ADC to lung microstructure changes. The lung changes due to emphysema will deteriorate the lung airways and alveoli, resulting in a different diffusion coefficient that can be effectively related to detecting the disease, its stages and progression. From here, one can expect to see a discernable difference in ADCs between healthy and diseased lungs as well as to track lung changes due to a disease over time by tracking changes in the ADC.

1.4 Hyperpolarized ^3He Measurements in Mouse Lungs

The flexibility of working with a mouse model makes applying the techniques of hyperpolarized ^3He magnetic resonance lung imaging to mice very logical, thus from that perspective, mice are suitable candidates for hyperpolarized ^3He gas MRI experiments. These experiments can serve as validations of the proposed MR method and also to study different mice models of lung diseases. On the other hand, the mouse is a small animal and many experiments involve larger rodents [11] or even larger animals like dogs or pigs [26]. As compared to other research animals, the small size of a mouse, and its lungs, pose experimental challenges that should be overcome to make them useful research vehicles to conduct hyperpolarized ^3He gas MRI experiments.

The main challenge is that mouse lung is about 10 times smaller than the average rat lung and around 6000 times smaller than the average human lung. This means that volumes of gas will be that much smaller, and although the expected signal should be roughly 40 times higher than that of the protons in the water molecule, such small amounts of hyperpolarized gas in tiny airways will rapidly degrade in polarization.

To date, the ^3He gas lung morphometry technique with hyperpolarized ^3He gas diffusion MRI was developed and exploited for human lungs [19]. In this study we use the ^3He gas lung morphometry to study lungs in mice, leveraging the theoretical model of [19], developed for human lungs. As mouse lungs have vastly smaller physical parameters, this requires modification of the theoretical equations that relate MRI diffusion measurements to lung microstructural parameters [19]. While the general MRI morphometry theory, to be addressed in sections that follow, remains valid, the specific relationships between lung microstructure parameters and the diffusion attenuated MR signals should be modified for mouse lungs, which is one of the objectives of this work. Thus, the theoretical model used in our experiment is generalized for the small physical size of mouse lung airways. Also because the length of acinar airways in mouse lung is much shorter than in humans, the diffusion gradient encoding duration should be shortened to minimize effects of ^3He atoms escaping into adjoining airways (this effect is not accounted for in the current theory) and distorting the lung morphometry measurements. In this study we use very short bipolar diffusion sensitizing gradient pulses ($\Delta t=440 \mu\text{s}$), as compared to $1800 \mu\text{s}$ in similar human experiments.

1.5 Main Project Steps

All experiments were performed on an Oxford Instruments (Oxford, UK) 4.7 T horizontal-bore magnet (33 cm magnet bore and 15 cm gradient bore), equipped with 60 G/cm gradient coils. All procedures are performed with the approval of the Washington University Animal Study Committee. To conduct any of the ^3He gas diffusion measurements in lungs, *ex vivo*, the main project steps are encompassed by the five major and distinct activities:

- 1) **Shimming:** Magnet shimming is accomplished using a spherical phantom containing doped water. The phantom was 17 mm in diameter mimicking the size of the inflated mouse lungs. The shimming was conducted using a tuning box, i.e., a passive LC circuitry that tunes the ^3He coil to the water Larmor frequency for the particular magnet field strength of 4.7 T.
- 2) **Lung extraction and intubation:** After collecting general information from a mouse while alive (weight, age, condition), the mouse was euthanized. The euthanasia was followed by opening the chest cavity and removing the lungs. This is a delicate first step that all subsequent steps and results depend on. Mouse lungs are very small in size; they have to be removed relatively fast and intact, along with the trachea. After the lungs are removed from the chest cavity, the heart and any surrounding fat are removed and the trachea is promptly catheterized with a plastic needle. Particular attention has to be paid not to pierce, cut or damage the lungs otherwise, as any gas leakage will prevent the experiment from being conducted properly.
- 3) **Delivery of the hyperpolarized ^3He gas to the lungs and the MRI experiment:** This step required building a valves-tubes-syringes gas delivery apparatus specially designed to be compatible with the small size of the mice lungs, the high magnetic fields in which it

must operate, and the easily de-polarizing nature of the hyperpolarized ^3He gas. The apparatus was tasked with delivering precise amounts at precise pressure of either ^3He gas or N_2 gas. Once extracted, the lungs were fitted into the ^3He coil and connected to the gas purge and delivery apparatus. Using the apparatus, the lungs were repeatedly purged using ^3He gas (at equilibrium polarization, not hyperpolarized) to remove virtually all remaining oxygen in the lungs. The freshly hyperpolarized ^3He gas was dispensed into a 1L Tedlar bag and the bag was connected to the gas delivery apparatus, ready to be delivered to the lungs. For the duration of the experiment, the Tedlar bag with hyperpolarized ^3He gas resided about 2 feet from the bore opening, along the field axis, where the fringe field of the magnet is about 100 G. This location was selected because the magnetic field is very strong yet the field gradients are small enough (~ 0.1 G/cm) to cause negligible T_1 relaxation of the gas [27, 28]. Immediately after the Tedlar bag was connected to gas delivery apparatus, the hyperpolarized ^3He gas is delivered to the lungs, followed by a small amount of inert gas, N_2 . The lung valve was then closed and the lungs were disconnected from the rest of the gas delivery system. The carrier along with the ^3He coil carrying lungs filled with required amount of ^3He gas was inserted into the center of the magnet for MRI scanning. Usually two to four MRI experiments, depending on the combination of the strength of the polarization and the type of the experiment, are conducted while changing diffusion encoding axis or other key parameters of the MRI sequence, as required. Once scanned, the lungs were pulled out of the magnet, connected to the gas delivery apparatus for the repetition of the process: purging, delivering fresh HP ^3He gas, and inserting back into the magnet for scanning.

- 4) The flip angle confirmation for each batch of ^3He gas: The duration and strength of each RF pulse determines the flip angle that the ^3He nuclear spins will exhibit. Each flip is a loss of irrecoverable nuclear polarization of the hyperpolarized ^3He gas. The precision of the sequence depends on the precision of the flip angle delivered used by the sequence, thus preliminary calibration of the flip angle was conducted using a syringe filled with the pure hyperpolarized ^3He gas by measuring the polarization loss after 20 RF pulses of fixed duration and strength.
- 5) Data Analysis: The MRI data obtained from the scanner were in the form of FID (Free Induction Decay) array of data. To convert it to information useful to us, we first put this array of data through the FFT (Fast Fourier Transform) transform to be able to see discernable spectral information as captured after each RF pulse in the sequence. To extract the peaks of major harmonics, the spectral data are analyzed using Varian's Bayes analysis software. These data are then transferred to MS Excel for further analysis: extraction from Varian format, averaging, flip angle correction. For this part of the process a few MS Excel tools enabling a quick manipulation of large data sets were developed. The previous steps prepare the data to be fit using a mathematical model developed in house specifically for mouse. This fitting is performed in Origin 7.5, professional graphing and data analysis software for scientists and engineers. The fitting of the mouse lung model to data using Origin 7.5, eventually yields information on physical lung dimensions, (varied radius of lung airways, R and r) as well as other important physical lung information (L_m – airway mean chord length, S/V and Na).

1.6 Dissertation Overview

Overview of the remaining chapters is as follows:

Chapter II is an overview of the theoretical background that provides the basis for deriving the latest mouse lung mathematical model for the ^3He gas diffusion. It is a discussion that covers the general physics of nuclear spins in magnetic field, their optical pumping to create the hyperpolarized ^3He gas and the science behind the MRI of such optically pumped gas. It also touches on the impacts of signal-to-noise ratio and its impact on optimizing the flip angle used in our MR pulse sequence. And lastly, the main parameters used in the pulsed field gradient experiment, such as b-value, gradient rise time, slew rate and gradient length are discussed. Further discussion is on the parameters measured by the experiment: diffusion attenuated MR signal and observed anisotropy in the mouse lungs.

Chapter III discusses the development of aforementioned mathematical model based on Stejskal-Tanner diffusion sequence, understanding the relationship between the b-value and the gradients as well as deriving mouse lung airways physical parameters. Additionally, the discussion is centered on approaches used to detect and consistently demonstrate anisotropy of the gas diffusion in the mouse lungs.

Chapter IV focuses on mission critical materials and methods for reliable and repetitive gas delivery to the mouse lungs. The chapter covers the design and development of the gas delivery apparatus including details on how to operate the gas delivery apparatus. Additionally, this chapter covers the animal preparation procedure: surgery of lung removal and trachea intubation. Attention was also given to limitations of the experiment and potential improvements.

Chapter V explains the calibration of the MR magnet. To conduct precise MR diffusion measurements, we needed equipment that will perform to the specifications (calibrate MR gradients) and minimize interferences (eddy currents). This chapter in general covers the equipment/hardware, either created or modified to increase confidence in our results. Items covered are eddy currents, external tuning box, RF coil and polarization equipment.

Chapter VI presents the details of the MR diffusion experiments and pulse sequences used. Deep level of detail is provided on the sequences used to measure the ^3He gas diffusion, all its intricacies and subsequent process of data extraction and analysis, as well as lung parameter calculation use the mouse lung model mentioned above. Similar discussion is given to the MR experiment that measures anisotropy of the diffusion in the mouse lungs.

Chapter VII presents the results of this research project: mouse lung physical parameters as obtained using non-invasive ^3He gas diffusion MR technique. For comparison and reference, included are the results of two more studies: one is similar *in vivo* study conducted in our laboratory, and the other is a collection of independent studies from numerous published works on the related subject. This chapter also includes our interpretation of the results obtained in these studies.

Chapter VIII summarizes the accomplishments, discusses the conclusions of the research project, reflects on known opportunities and gives an insight to future work that can build on results obtained here.

Each chapter has its own collection of references.

Appendix A provides details on the pulse sequences used for setting up the equipment and experiments. This appendix includes pulse sequences for eddy-current measurements and flip-angle calibrations.

Appendix B provides detailed pulse sequences for the experiments themselves, ^3He Lung Morphometry and the Anisotropy experiment. This appendix includes the source code, explanations and their applications to the specific parts of this research project.

1.7 References

1. **Haefeli-Bleuer, B. and E.R. Weibel**, Morphometry of the human pulmonary acinus. *Anat Rec.* **220**(4): p. 401-14, 1988.
2. **Knudsen, L., E.R. Weibel, H.J. Gundersen, F.V. Weinstein, and M. Ochs**, Assessment of air space size characteristics by intercept (chord) measurement: an accurate and efficient stereological approach. *J Appl Physiol.* **108**(2): p. 412-21, 2010.
3. **Knust, J., M. Ochs, H.J. Gundersen, and J.R. Nyengaard**, Stereological estimates of alveolar number and size and capillary length and surface area in mice lungs. *Anat Rec (Hoboken).* **292**(1): p. 113-22, 2009.
4. **Rodriguez, M., S. Bur, A. Favre, and E.R. Weibel**, Pulmonary acinus: geometry and morphometry of the peripheral airway system in rat and rabbit. *Am J Anat.* **180**(2): p. 143-55, 1987.
5. **Weibel, E.R.**, What makes a good lung? *Swiss Med Wkly.* **139**(27-28): p. 375-86, 2009.
6. **Yablonskiy, D.A., A.L. Sukstanskii, J.C. Leawoods, D.S. Gierada, G.L. Bretthorst, S.S. Lefrak, J.D. Cooper, and M.S. Conradi**, Quantitative in vivo assessment of lung microstructure at the alveolar level with hyperpolarized ^3He diffusion MRI. *Proc Natl Acad Sci U S A.* **99**(5): p. 3111-6, 2002.
7. **Hsia, C.C.W., D.M. Hyde, M. Ochs, and E.R. Weibel**, An Official Research Policy Statement of the American Thoracic Society/European Respiratory Society: Standards for Quantitative Assessment of Lung Structure. *American Journal of Respiratory and Critical Care Medicine.* **181**(4): p. 394-418, 2010.
8. **Middleton, H., R.D. Black, B. Saam, G.D. Cates, G.P. Cofer, R. Guenther, W. Happer, L.W. Hedlund, G.A. Johnson, K. Juvan, and et al.**, MR imaging with hyperpolarized ^3He gas. *Magn Reson Med.* **33**(2): p. 271-5, 1995.
9. **Schaefer, S.R., G.D. Cates, and W. Happer**, Determination of spin-exchange parameters between optically pumped rubidium and ^{83}Kr . *Phys Rev A.* **41**(11): p. 6063-6070, 1990.
10. **Albert, M.S., G.D. Cates, B. Driehuys, W. Happer, B. Saam, C.S. Springer, Jr., and A. Wishnia**, Biological magnetic resonance imaging using laser-polarized ^{129}Xe . *Nature.* **370**(6486): p. 199-201, 1994.

11. **Chen, X.J., L.W. Hedlund, H.E. Moller, M.S. Chawla, R.R. Maronpot, and G.A. Johnson**, Detection of emphysema in rat lungs by using magnetic resonance measurements of ^3He diffusion. *Proc Natl Acad Sci U S A.* **97**(21): p. 11478-81, 2000.
12. **Saam, B.T., D.A. Yablonskiy, V.D. Kodibagkar, J.C. Leawoods, D.S. Gierada, J.D. Cooper, S.S. Lefrak, and M.S. Conradi**, MR imaging of diffusion of (^3He) gas in healthy and diseased lungs. *Magn Reson Med.* **44**(2): p. 174-9, 2000.
13. **Salerno, M., E.E. de Lange, T.A. Altes, J.D. Truwit, J.R. Brookeman, and J.P. Mugler, 3rd**, Emphysema: hyperpolarized helium 3 diffusion MR imaging of the lungs compared with spirometric indexes--initial experience. *Radiology.* **222**(1): p. 252-60, 2002.
14. **Jacob, R.E., K.R. Minard, G. Laicher, and C. Timchalk**, 3D ^3He diffusion MRI as a local in vivo morphometric tool to evaluate emphysematous rat lungs. *J Appl Physiol.* **105**(4): p. 1291-300, 2008.
15. **Peces-Barba, G., J. Ruiz-Cabello, Y. Cremillieux, I. Rodriguez, D. Dupuich, V. Callot, M. Ortega, M.L. Rubio Arbo, M. Cortijo, and N. Gonzalez-Mangado**, Helium-3 MRI diffusion coefficient: correlation to morphometry in a model of mild emphysema. *Eur Respir J.* **22**(1): p. 14-9, 2003.
16. **Woods, J.C., C.K. Choong, D.A. Yablonskiy, J. Bentley, J. Wong, J.A. Pierce, J.D. Cooper, P.T. Macklem, M.S. Conradi, and J.C. Hogg**, Hyperpolarized ^3He diffusion MRI and histology in pulmonary emphysema. *Magn Reson Med.* **56**(6): p. 1293-300, 2006.
17. **Mata, J.F., T.A. Altes, J. Cai, K. Ruppert, W. Mitzner, K.D. Hagspiel, B. Patel, M. Salerno, J.R. Brookeman, E.E. de Lange, W.A. Tobias, H.T. Wang, G.D. Cates, and J.P. Mugler, 3rd**, Evaluation of emphysema severity and progression in a rabbit model: comparison of hyperpolarized ^3He and ^{129}Xe diffusion MRI with lung morphometry. *J Appl Physiol.* **102**(3): p. 1273-80, 2007.
18. **Sukstanskii, A.L. and D.A. Yablonskiy**, In vivo lung morphometry with hyperpolarized ^3He diffusion MRI: theoretical background. *J Magn Reson.* **190**(2): p. 200-10, 2008.
19. **Yablonskiy, D.A., A.L. Sukstanskii, J.C. Woods, D.S. Gierada, J.D. Quirk, J.C. Hogg, J.D. Cooper, and M.S. Conradi**, Quantification of lung microstructure with hyperpolarized ^3He diffusion MRI. *J Appl Physiol.* **107**(4): p. 1258-65, 2009.
20. **Robbesom, A.A., E.M. Versteeg, J.H. Veerkamp, J.H. van Krieken, H.J. Bulten, H.T. Smits, L.N. Willems, C.L. van Herwaarden, P.N. Dekhuijzen**,

- and T.H. van Kuppevelt**, Morphological quantification of emphysema in small human lung specimens: comparison of methods and relation with clinical data. *Mod Pathol.* **16**(1): p. 1-7, 2003.
21. **Walker, T.G. and W. Happer**, Spin-exchange optical pumping of noble-gas nuclei. *RevModPhys* **69**: p. 629-642, 1997.
 22. **Leawoods, J.C., D.A. Yablonskiy, B. Saam, D.S. Gierada, and M.S. Conradi**, Hyperpolarized ³He gas production and MR imaging of the lung. *Concepts in MR.* **13**(5): p. 277-293, 2001.
 23. **Agulles-Pedros, L., R.H. Acosta, P. Blumler, and H.W. Spiess**, Resolution enhancement in MRI of laser polarized ³He by control of diffusion. *J Magn Reson.* **197**(1): p. 56-62, 2009.
 24. **Schreiber, W.G., A.E. Morbach, T. Stavngaard, K.K. Gast, A. Herweling, L.V. Sogaard, M. Windirsch, J. Schmiedeskamp, C.P. Heussel, and H.U. Kauczor**, Assessment of lung microstructure with magnetic resonance imaging of hyperpolarized Helium-3. *Respir Physiol Neurobiol.* **148**(1-2): p. 23-42, 2005.
 25. **Reid R.C., P.J.M., Sherwood T.K.**, *The properties of gases and liquids.* 1977: New York: McGraw-Hill.
 26. **Zheng, J., J.C. Leawoods, M. Nolte, D.A. Yablonskiy, P.K. Woodard, G. Laub, R.J. Gropler, and M.S. Conradi**, Combined MR proton lung perfusion/angiography and helium ventilation: potential for detecting pulmonary emboli and ventilation defects. *Magn Reson Med.* **47**(3): p. 433-8, 2002.
 27. **Saam, B., D.A. Yablonskiy, D.S. Gierada, and M.S. Conradi**, Rapid imaging of hyperpolarized gas using EPI. *Magn Reson Med.* **42**(3): p. 507-14, 1999.
 28. **Cates, G.D., S.R. Schaefer, and W. Happer**, Relaxation of spins due to field inhomogeneities in gaseous samples at low magnetic fields and low pressures. *Phys Rev A.* **37**(8): p. 2877-2885, 1988.

Chapter 2 - Physics of Magnetic Resonance Imaging with Hyperpolarized ^3He

2.1 Theoretical Nuclear Spin Physics

Our experiments are based on theory of detection of nuclear spins in magnetic field that was established around 50-60 years ago. The main concepts of theoretical physics related to the behavior of nuclear spins in a magnetic field and the concept of gas hyperpolarization will be succinctly explained in subsequent sections.

2.1.1 Nuclear Spins in Magnetic Fields

NMR (nuclear magnetic resonance) is a property that magnetic nuclei have in a magnetic field and applied radio frequency pulse (or pulses), which cause the nuclei to absorb energy from the radio frequency pulse and radiate this energy back out. The energy radiated back out is at a specific resonance frequency which is proportional to the strength of the magnetic field. Thus, the key feature of NMR is that the resonance frequency of a particular substance is directly proportional to the strength of the applied magnetic field.

Particles that compose any atomic nucleus, neutrons and protons, have the intrinsic quantum property of spin, determined by a spin quantum number S . If the number of both protons and neutrons in a given nucleus is even, then $S=0$. A non-zero spin is always associated with a non-zero magnetic moment (μ) via the relation $\mu=\gamma\hbar S$, where γ is the

gyromagnetic ratio and \hbar is reduced Planck's constant (divided by 2π). It is this magnetic moment that allows the observation of the NMR spectra.

^3He has a nuclear spin $1/2$ and when placed in magnetic field, the energy of a magnetic moment μ when in a magnetic field B_0 is given by:

$$E = -\gamma\hbar B_0 m_s \quad (2.1)$$

where m_s is spin energy level. As a result, the nuclear spins states, (spins up and spins down) have different energies in a non-zero magnetic field. For most isotopes γ is positive, then $m_s=1/2$ is the lower energy state ($m_s=-1/2$ being the higher energy state) and the energy difference between the two states is:

$$\Delta E = -\gamma\hbar H_0 \quad (2.2)$$

If an ensemble of such spins is placed in a magnetic field, this difference results in a small population bias towards the lower energy state, $m_s=1/2$.

This distribution between energy levels of spins up and spins down, determines the spin polarization. At room temperature, the thermal energy dominates over the energy difference between the two energy states (ΔE) so that for equilibrium the Boltzmann polarization for ^3He at 25°C , in a magnetic field strength of 4.7 Tesla is:

$$P \approx \frac{\hbar\omega}{2k_bT} = \frac{(1.05 \times 10^{-34} \text{ J} \cdot \text{s})(2\pi \cdot 151.8 \times 10^6 \text{ s}^{-1})}{2(1.38 \times 10^{-23} \text{ J} / \text{K})(298 \text{ K})} = 1.2 \times 10^{-5} \quad (2.3)$$

$$P = 12 \text{ ppm} \quad (2.4)$$

where $\omega=2\pi f$ and $f=151.82$ MHz is the precession frequency of the ^3He nucleus in 4.7 Tesla magnetic field, k_b is Boltzmann's constant and T is room temperature in Kelvins.

An NMR signal is proportional to the product of polarization P and the spin density. For comparison, density of water is 2500-3000 times higher than the density of gas, thus giving roughly that much better NMR signal for the same room temperature conditions and Boltzmann equilibrium polarization.

2.1.2 Hyperpolarization

According to equations (2.2), (2.3) and (2.4), the strength of MR signal grows with the magnitude of magnetic field B_0 . Another way to improve the effectiveness of NMR is by using hyperpolarization, the nuclear spin polarization far beyond thermal equilibrium conditions. It is a state where much larger population of spins is forced into one energy state (or the other). This is however not a stable condition for the distribution of the spins, it is far from equilibrium state, thus spins will return to the Boltzmann equilibrium in a time order of the longitudinal relaxation time constant T1. Typical ^3He gas hyperpolarization hardware allow the boost of polarization to $\sim 40\%$, $P=0.4$.

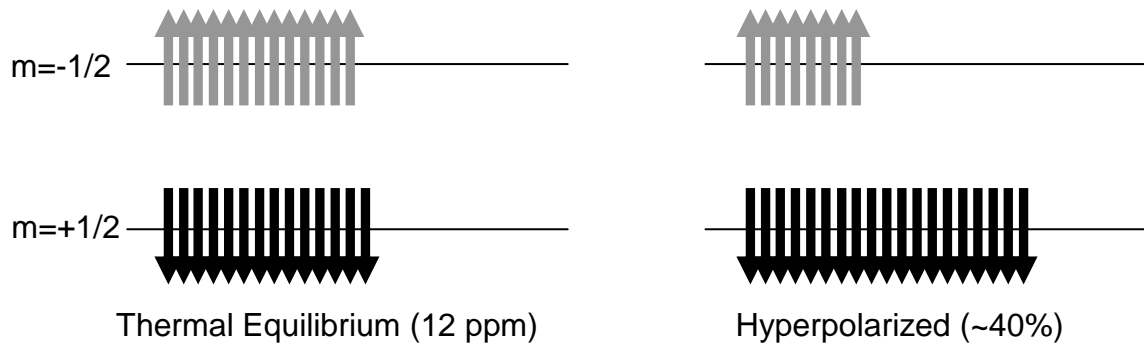


Figure 2.1: Illustrative comparison of Thermal (Boltzmann) equilibrium of several ppm polarization of ^3He gas (nuclear spin number $I=1/2$) versus the high level of nuclear spin polarization reached by optical pumping, $\sim 40\%$.

Various mechanisms are enemy of such high nuclear spin polarization: ^3He atoms' collisions with other ^3He atoms and with other materials present (wall of the polarization cell, small tubing walls, other gas atoms or molecules in the cell or bag), field inhomogeneities or any T1 mechanisms. Almost instant depolarization will be caused by ^3He gas contact with paramagnetic O_2 molecules or any ferromagnetic materials. In later text we will discuss what precautions we take to minimize any of the factors above to increase the hyperpolarized ^3He gas T1 and ultimately improve signal-to-noise ratio (SNR) of the MR experiment.

2.2 Spin Exchange – Optical Polarization of ^3He Gas

First introduced by Kastler [1] in 1950, the polarized ^3He gas has been a useful tool and a testing ground in many areas of research, including the MR imaging of lungs and airways. This section focuses on the system and mechanism employed in hyperpolarizing the ^3He nuclei using spin exchange with optically pumped rubidium atoms. In short, Rubidium valence electrons are polarized by absorption of circularly polarized resonant laser light at

795 nm in a glass cell along with ^3He gas at a high pressure. Through collisions with ^3He atoms, polarization is transferred to the ^3He nucleus, creating hyperpolarized ^3He gas. Relatively recent advances in Ti:Sapphire lasers and specifically laser diode arrays are the main vehicles for achieving high polarizations (40% or more).

2.2.1 Optical Pumping of Rubidium Electrons

Polarization of noble gas (^3He) via spin exchange requires a source of angular momentum to transfer to the noble gas: in this case, the source is optically pumped rubidium (Rb). Although in theory any alkali metal can be used to be optically pumped, Rb is alkali of choice for its dense vapor and humble temperatures, to achieve high levels of polarization.

Optical pumping of Rb is accomplished by absorption of resonant photons that carry angular momentum to the Rb atom. Linearly polarized laser light resonant with the energy level splitting of the Rb electrons is passed through a quarter-wave ($\lambda/4$) plate giving it an angular momentum. The $\lambda/4$ plate in effect converts the light from linearly polarized laser light into circularly polarized laser light. In an enclosed polarization glass cell, under high pressure (125 psi), and high temperature (350 F), the liquid rubidium is vaporized and mixed with the ^3He gas. The cell is illuminated with the circularly polarized laser light effectively bombarding the atoms of rubidium. Since the light is resonant with the principal electric dipole transition of the valence electrons, the spin of the electrons couple with the orbital angular momentum of the laser light. This results in the valence electrons being excited from $5s_{1/2}$ ground state to $5p_{1/2}$, excited state [2] (Figure 2.2). The wavelength of this transition is ~ 795 nm, a match to the frequency of the laser light that carries the angular momentum.

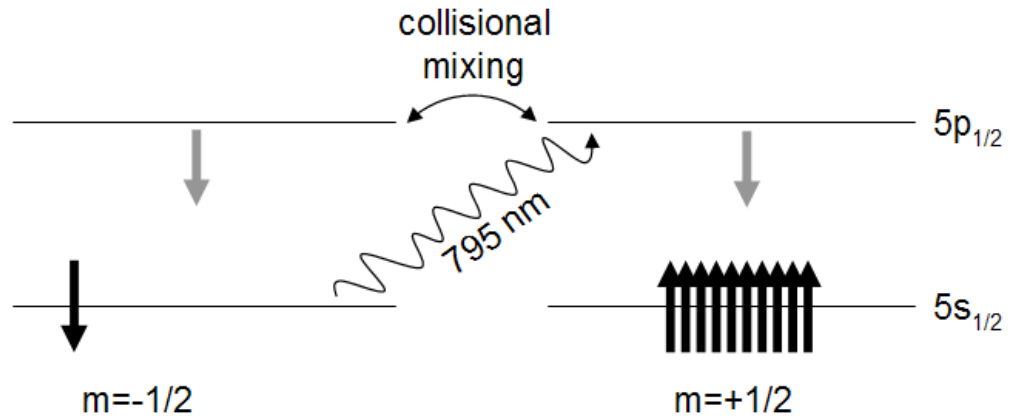


Figure 2.2: Vaporized Rb illuminated using circularly polarized laser light. The light excites the electron transitions from $5s_{1/2}$ ground state into $5p_{1/2}$ excited state. Collisional mixing provides near even re-population of both sub-levels of the excited state. Electrons falling into $m=-1/2$ excited state sub-level eventually decay to the ground state where they are re-pumped, resulting in extremely high polarization of Rb electrons into $m=1/2$ state.

Basically, vaporized Rb electrons are “pumped” to the excited state by the mechanism of the matched frequency circular laser light absorption. Before the Rb electrons leave their excited state, the Rb atoms rapidly collide with the ^3He atoms, re-distributing the electrons into sub-levels of the excited state [3] nearly completely destroying the electron spin polarization of Rb. Nonetheless, electrons are continuously pumped back into the $5p_{1/2}$, excited state by the laser light. Using this mechanism electron polarization of Rb nearly to 100% can be achieved with a well-tuned system [2].

While optical pumping is used to change the electron spin, nuclear spin can be modified by the hyperfine interaction between the electron and nuclear magnetism.

2.2.2 Polarization Transfer from Rb to ^3He

Key process in spin-exchange optical pumping is collisional transfer of polarization between optically pumped vaporized Rb atoms and the nuclei of ^3He gas we are hyperpolarizing. As Figure 2.3 shows, for ^3He , the transfer of angular momentum occurs mostly in simple binary collisions between the atoms [2]. The time for binary collision is ~ 10 - 12 sec, continuously flipping the nuclear and electronic spins, leaving the Rb atom ready to be re-polarized and ready to collide with another ^3He nucleus, to transfer the spin.

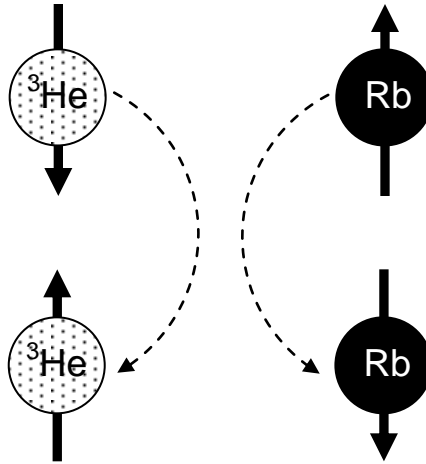


Figure 2.3: Polarization transfer process during binary collisions of the ^3He nuclei and Rb electrons. Spin polarization is continuously exchanged leaving the Rb electron spin-down while the ^3He nuclei get hyperpolarized.

Collisions between ^3He nuclei and the Rb electrons are very frequent however, transfer of the angular momentum during the collision occurs only with the small probability. The spin-exchange rate, γ_{se} is linearly proportional to the density of Rb vapor [4].

The rate of the ^3He gas hyperpolarization as a result of the Rb optical pumping and the rare spin-exchange process approaches a limiting value as a function of time:

$$P_{^3\text{He}}(t) = \langle P_{\text{Rb}} \rangle \frac{\gamma_{se}}{\gamma_{se} + T_1^{-1}} \left[1 - e^{-(\gamma_{se} + T_1^{-1})t} \right] \quad (2.5)$$

where P_{Rb} is the Rb polarization, γ_{se} is spin-exchange rate and T_1 is pure ^3He relaxation constant (pure ^3He gas, no other gases present).

The process of hyperpolarization is a gradual and slow process as the spin-exchange rate is very small while various processes, as T_1 , bad collisions with Rb, collisions with the walls, etc. are continuously reducing polarization level. The highest level of polarization will be eventually reached when the amount of ^3He nuclei that get hyperpolarized is the same as number of ^3He nuclei that get de-polarized by various competing processes mentioned above, per unit of time.

In practice, using our polarizing equipment, polarization of $\sim 1\text{L}$ of ^3He gas to 40%-45% level takes around 22 hours under typical temperature and pressure conditions in the glass cell.

2.3 Design of a HP ^3He MRI Diffusion Experiment: Critical Components

To properly design and conduct the MRI experiments with hyperpolarized ^3He gas in small animal lungs, full understanding of entire process and equipment is required: knowing your

equipment performance limitations, capabilities of the ^3He coil, to designing the sequence to extract lung physical information from the experimental setup, selecting and calibrating the flip angle. This and many other variables pertinent to the experiment will be discussed in this section.

2.3.1 RF Coil and Tuning Box

When a sample is inserted in the permanent magnet (B_0 field), the nuclear spins tend to align with the strong magnetic field, in our case 4.7 T. The sample is always inside a RF (radio frequency) coil that, when emitting the RF signal, can flip the spins (net magnetization). When coil in receiving mode, it can detect electrical induction from those same spins, as they are precessing. For our particular experiment we used a single loop coil, tuned to precise frequency of ^3He for the particular B_0 field.

A schematic of typical NMR coil, as R-L-C (resistance – inductance – capacitive) resonant circuit (as shown in Figure 2.4)

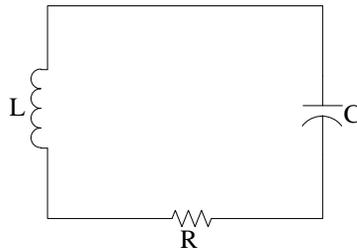


Figure 2.4: Typical RF coil can be represented as a series connection of R-L-C oscillating at the resonant angular frequency ω .

is tuned to the specific frequency of the nuclei of interest as modulated by the frequency of the B_0 field. Sum of the impedances around the circuit is given by Equation (2.6):

$$Z = R + j \left(\omega L - \frac{1}{\omega C} \right) \quad (2.6)$$

where ω is an angular frequency. The quantity in parenthesis is zero when $\omega = 1/\sqrt{LC}$ and that value of ω is called resonant frequency. At that value of ω , the total impedance of the circuit is $Z=R$. In our case, the RF coil was tuned to the frequency of ^3He nuclei equal to 151.82 MHz for our 4.7T scanner.

Ability to conduct the proton scanning (imaging) using the same RF coil as for ^3He imaging, can be useful for various reasons, e.g., one can conduct the scanning using one RF coil on the same sample and generate ^3He as well as complimentary ^1H images. It can be also used to ensure the sample's position prior to the expensive ^3He MR scans, and in more general sense to avoid the need to remove the sample to physically change the resonant frequency of the RF coil to obtain image of another nuclei of interest. This can be achieved using various means, building double resonance coils (coils with two resonant frequencies) or placing another circuitry in series with the original RF coil that tunes it to the new frequency of interest (tuning box). We choose the later one as it can be easily removed and original RF coil will perform to the full standards. The tuning box is a passive one, a simple set of a L-C, and when connected to the RF coil, the schematic changes to one depicted in Figure 2.5. The resonant frequency of this new circuitry, as before, is a solution of the total impedance of the circuit, given by Equation (2.7):

$$Z = R + j \left(\omega L - \frac{1}{\omega C} \right) - j \left(\frac{\frac{L_D}{C_D}}{\omega L_D - \frac{1}{\omega C_D}} \right) \quad (2.7)$$

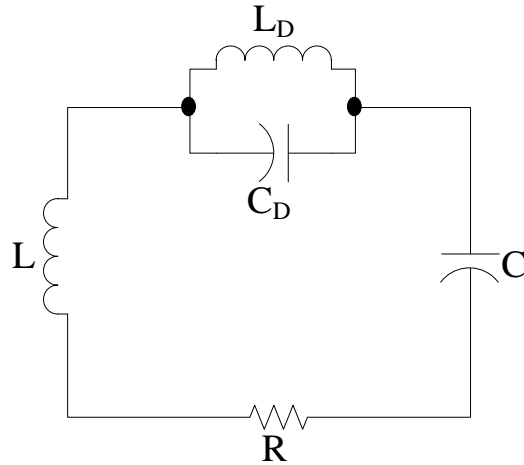


Figure 2.5: When tuning box placed between the RF coil and the amplifier, the equivalent schematic looks as shown, resonant circuitry for dual frequency is a parallel L-C circuit in series with the connection of R-L-C circuitry.

In practice, the RF coils are usually connected to the RF amplifier through inductively coupled circuitry, usually another series L-C circuit, as in the Figure 2.6. The RF amplifier is connected to a simple series L-C circuitry, inductive coupled to the MRI resonant circuitry, tuned to the frequency of interest.

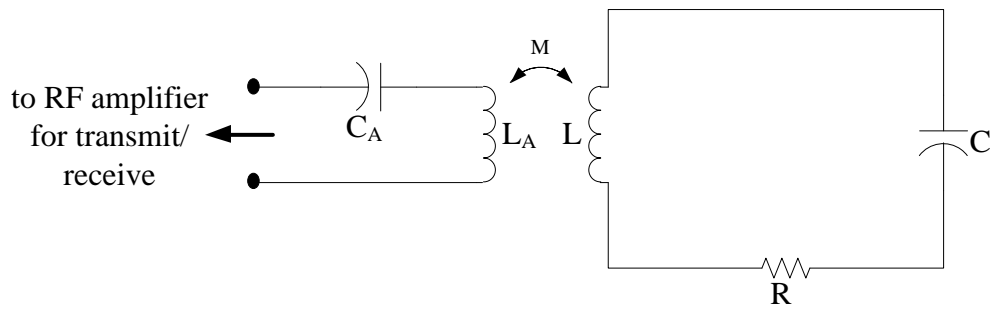


Figure 2.6: The schematic shows typical RF RLC resonant circuit inductively coupled to RF amplifier.

The RF coil is tuned to the frequency of the nuclei we are observing (^3He) for the given B_0 field strength using a network analyzer. As the mouse lungs are small and present very little

or no loading to the RF coil, it is tuned without a load to the precise frequency. The tuning box connected in series with the RF ^3He coil is then tuned to the proton frequency. The proton frequency tuning is as well conducted on the network analyzer by choosing the minimum attenuation and minimal impedance on the Smith chart.

2.3.2 Flip Angle

When sample is inserted in the magnetic field B_0 , spins will precess around the magnetic field with the angular frequency of $\omega = \gamma B_0$. The RF coil, perpendicular to the B_0 external field, excited with alternating current at the same frequency ω , will effectively apply an oscillating magnetic field B_1 , perpendicular to B_0 . This will result in nuclear spins being flipped, depending on the strength and duration of the RF (B_1) field applied.

In general, the degree of rotation of a net magnetization vector aligned along Z axis towards the x-y plane by a radiofrequency pulse is called “flip”, “tip” or “nutating” angle, most commonly denoted as the flip angle α .

We usually think of a RF pulse at Larmor frequency flipping the net magnetization away from Z axis by an angle α . The flip angle α is a function of both, strength of the applied RF field B_1 and, the time τ for which the field is being applied.

$$\alpha = \alpha(B_1, \tau) \quad (2.8)$$

Flip angles between 0° and 90° are typically used in FID sequences, 90° and a series of 180° pulses in spin echo sequences and an initial 180° pulse followed by a 90° or smaller in inversion recovery sequences.

Flip angle lower than 90° decreases the amount of longitudinal magnetization by partially tipping it into the transverse plane. Besides conserving irrecoverable longitudinal polarization of the hyperpolarized ^3He spins, it also allows for shorter TR/TE and decreased scan time and faster acquisitions. The flip angle also determines the quantity of the magnetization left on the longitudinal axis; in Figure 2.7, Z-axis.

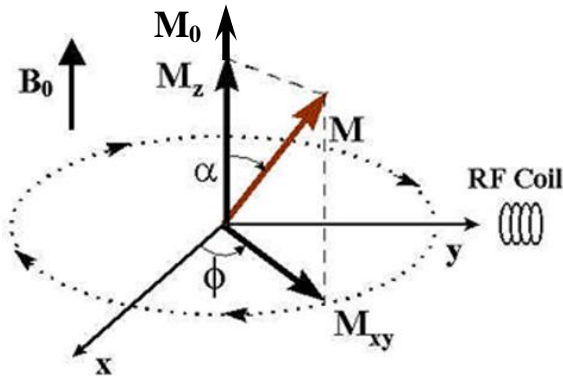


Figure 2.7: The magnetization, M , precesses about the Z axis with the tip angle α , and it is divided into the longitudinal component, M_z and transverse component, M_{xy} . A RF coil is placed in the Y axis direction to collect the MR signal.

Once M_0 is flipped for the flip angle α , the longitudinal magnetization vector, M_z , can be described mathematically as $M_z = M_0 \cos\alpha$. The z-magnetization after two RF pulses, provided they are administered sufficiently close in time to each other (to ignore T1 effects), is given by Equation (2.9):

$$M_0 \cos\alpha \cos\alpha \quad (2.9)$$

It is easy to conclude that after n such pulses, remaining z-magnetization will be $M_0(\cos\alpha)^n$. Using this relationship and desire to retain some longitudinal magnetization ($\sim 25\text{-}30\%$) after the last pulse to ensure good SNR throughout the sequence, a simple iterative calculation is

used to calculate the appropriate flip angle from the varied number of consecutive RF pulses.

2.6 References

1. **Kastler, A.**, Applications of polarimetry to infra-red and micro-wave spectroscopy. *Nature*. **166**(4211): p. 113, 1950.
2. **Happer, W.**, Optical Pumping. *RevModPhys*. **44**(2): p. 169-249, 1972.
3. **Appelt, S., Ben-Amar Baranga, A., Erickson, CJ**, Theory of spin-exchange optical pumping of ^3He and ^{129}Xe . *Phys Rev A*. **58**(2): p. 1412-1439, 1998.
4. **Leawoods, J.C., D.A. Yablonskiy, B. Saam, D.S. Gierada, and M.S. Conradi**, Hyperpolarized ^3He gas production and MR imaging of the lung. *Concepts in MR*. **13**(5): p. 277-293, 2001.

Chapter 3 - Materials and Methods: MR Diffusion Procedure for Mouse Lungs

Chapters 3, 4 and 5 are all Materials and Methods, outlining the details of my contribution to the project. In Chapter 3 those are the contribution to develop MR diffusion procedure for the mouse lungs, vast amount of trials and errors followed by optimization of the model until it yielded results. In Chapter 4, it is creating and perfecting the apparatus for delivery of the ^3He to the mouse lungs, surgery, removal and preparation of the lungs for successful MR scanning. In Chapter 5, it is calibrating the equipment, namely MR gradients, checking for any eddy current issues and creating and tuning the MR coil. With all of this done, my contribution was in writing and testing the MR diffusion sequence that synthesized all the information above to use the maximum out of the hardware without tripping or damaging the gradient amplifiers. Using the sequence and its variations, all experiments were conducted.

3.1 MR Measurements of Lung Microstructure

The theoretical background of the MR lung morphometry with HP ^3He gas in mice is similar to the method that was developed in humans [1-3]. Hence we describe it here only briefly. Measuring the diffusion of ^3He gas in lung airspaces can provide valuable information on the lung microstructure. To make the information encoded in the diffusion-attenuated MRI signals quantitative, the relationship between lung microstructural parameters and the MR signal attenuation function is required. In our approach, the lung acinus is treated as a network of cylindrical passages covered with alveolar sleeves [4, 5] where the main

geometrical parameters characterizing these airways are the outer radius R and the depth of the alveolar sleeve, h [3] (see Figure 3.1).

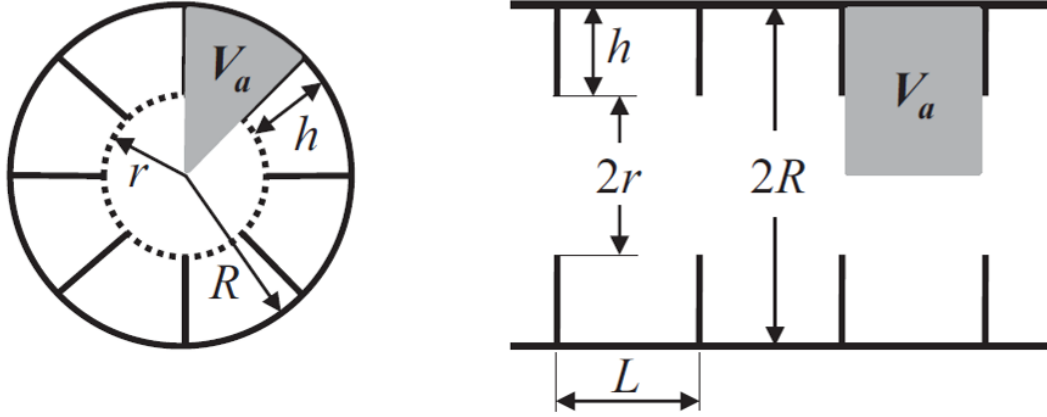


Figure 3.1: Schematic structure of an acinar airway with eight alveoli distributed along the annular ring (eight-alveolar model). Left is a cross section of the airway perpendicular to its length and the right is a cross section along the length of the airway. Each airway (duct or sac) can be considered geometrically as a cylindrical object consisting of an alveolar sleeve with alveoli opening toward the internal cylindrical air passage. The diagram defines inner (r) and outer (R) airway radii (as in Fig. 1 in [4] and [2]) and the depth of the alveolar sleeves (h). The ratio $L=0.765 \cdot R$ is chosen so that the alveolar size is the same along the airway and along the circumference [3]. The shaded area shows lung air volume per alveolus V_a that comprises both the volume of alveolus proper and the immediately associated duct volume.

3.1.1 MR Diffusion Experiment

Measurements of increasing apparent diffusion coefficient (ADC) of the hyperpolarized ^3He gas have been linked to the increases in emphysema in lungs, thus ADC can be used as a tool to quantify, at some level, the lung microstructure. Changes in internal lung microstructure imply changes in restrictions (obstacles to the hyperpolarized ^3He gas diffusion) in the lungs, effectively altering the measured ADC.

Stejskal and Tanner in their seminal paper in 1965 introduced pulsed field gradient sequence [6] into the basic spin echo sequence, resulting in much improved sensitivity to diffusion as compared to steady state gradients. A pulsed field gradient is a bipolar gradient pulse with spatial dependent field intensity. Any gradient is identified by four characteristics: axis, strength, shape and duration. Application of a field gradient destroys the FID signal, but this can be recovered and measured by a refocusing gradient.

Stejskal-Tanner solved Bloch's partial differential equation for a symmetric pair of pulsed gradients (see Figure 3.2) and obtained the well-known Stejskal-Tanner formula (see Equation (3.1)). They were first to propose measuring restricted diffusion by varying the distance between bi-polar gradient pulses. After a RF excitation, a short and strong gradient G is applied along a single axis, changing the constant main field B_0 to a spatially variable field $B(x) = B_0 + Gx$. With time and gradient strength, some phase differences will accumulate between spins at different positions. After time Δ , the opposite gradient, $-G$, is applied. If atoms did not move, the phase would be perfectly reversed and magnetization would be fully restored. The refocusing will not be perfect for spins that have moved during the time interval between the pulses, and the signal measured by the MRI machine is reduced. This reduction in signal due to the application of the pulse gradient can be related to the amount of diffusion that is occurring through the following equation:

$$\frac{S}{S_0} = e^{-\gamma^2 G^2 \delta^2 (\Delta - \delta/3) D} = e^{-bD} \quad (3.1)$$

where S_0 is the signal intensity without the diffusion weighting, S is the signal with the gradient, γ is the gyromagnetic ratio, G is the strength of the gradient pulse, δ is the duration of the pulse, Δ is the time between the two pulses, and finally, D is the diffusion-coefficient.

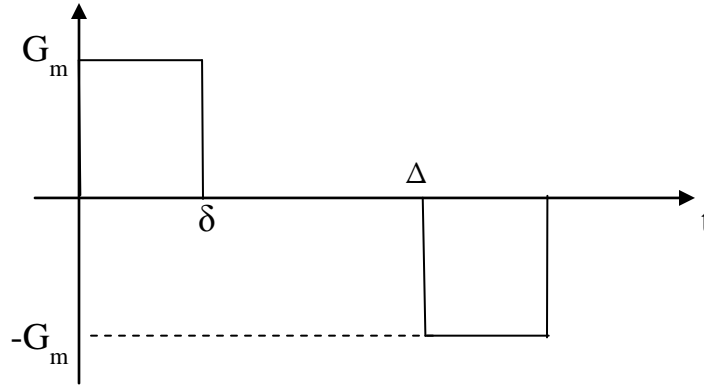


Figure 3.2: Bi-polar pulsed gradients. Stejskal-Tanner were first to propose the idea of measuring restricted diffusion by varying the Δ between gradient pulses.

In the Stejskal-Tanner experiment, the attenuation of MR signal is a measure of molecular displacement during the diffusion time. For restricted diffusion, intensity of MR signal is no longer described by Eq. (3.1) and is usually written as:

$$S = S_0 e^{-b \cdot ADC} \quad (3.2)$$

where “ b ” is known as a b-value, while ADC is dependent on the restrictive lung environment and pulse sequence parameters.

Faster diffusion (larger ADC) means that the spins have bigger chance to travel farther and therefore experience larger magnetic field changes, due to diffusion gradients, causing larger spread in phase and resulting in a smaller MR signal. If the relationship between ADC and

system structure is known, measuring the signal as a function of b-value provides an opportunity to obtain the properties of a system.

For pure ^3He gas at normal pressure of 1 atm and at the room temperature, we measured the unrestricted or free diffusion coefficient at $\sim 1.75 \text{ cm}^2/\text{s}$.

3.1.2 Gradient relationship to b-value

The so called b-value depends on the strength, shape and duration of diffusion-weighting gradient waveform. For the gradient waveform in Figure 3.2, b-value from Equation (3.1) is:

$$b = \gamma^2 G_m^2 \delta^2 \left(\Delta - \frac{\delta}{3} \right) \quad (3.3)$$

This gradient waveform is not possible in practice, e.g., it is impossible to have infinite rate of change from zero to G_m . A more realistic gradient waveform that is attainable by the hardware (Figure 3.3) is used to calculate the b-value relationship as in [2]:

$$b = (\gamma G_m)^2 \left[\delta^2 \left(\Delta - \frac{\delta}{3} \right) + \tau \left(\delta^2 - 2\Delta\delta + \Delta\tau - \frac{7}{6}\delta\tau + \frac{8}{15}\tau^2 \right) \right] \quad (3.4)$$

where the second parenthesis in the bracket is due to the finite ramp-up and ramp-down times in the gradient waveform in Figure 3.3.

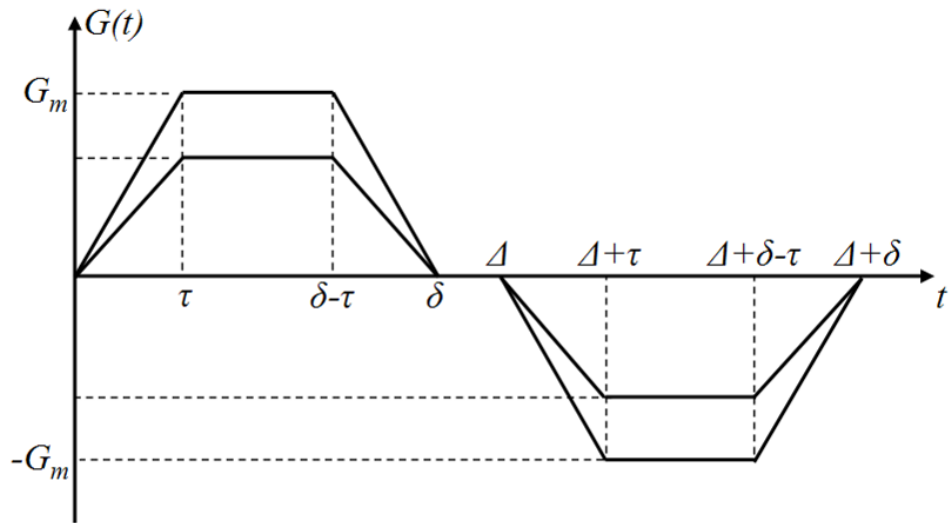


Figure 3.3: Gradient slew rate (time τ) is dynamically controlled to satisfy Equation (3.4) and not to exceed maximum hardware capabilities.

If the gradient rise time is zero the Equation (3.4) is reduced back to Equation (3.3) and the gradient waveform in Figure 3.3 is similarly reduced to the one in Figure 3.2.

Given that the b-value is a reflection of the strength and duration of the bi-polar gradient waveform, a thoughtful selection of the b-value is important when measuring gas diffusion in the lungs. If the b-value is small, attenuation of the MR signal will be small and the ratio of attenuated vs. unattenuated signal will be close to unity, making reliable diffusion calculations difficult. If b-value is selected to be very high, the gradients will attenuate the signal close to the noise floor making diffusion calculations virtually impossible. An acceptable range of b-values depends mostly on the expected diffusion that in turn depends on the size of the airways that we attempt to measure with this MR technique.

3.1.3 Theory of Gas Diffusion in Mouse Lungs

Molecular diffusion in each acinar airway is characterized by longitudinal and transverse diffusion coefficients D_L and D_T . Given a large number of airways in the lungs (in our experiment MR signal is collected from the mouse's entire lungs, excluding large conducting airways), it is safe to assume a uniform distribution of airway spatial orientations. Accordingly, the diffusion attenuated MRI signal can be presented as [2]:

$$S(b) = S_0 \exp(-b \cdot D_T) \left(\frac{\pi}{4bD_{AN}} \right)^{1/2} \cdot \Phi \left[(bD_{AN})^{1/2} \right], \quad D_{AN} = D_L - D_T \quad (3.5)$$

where b is the so-called b-value that depends on the strength and duration of diffusion-weighting gradient waveform (see corresponding expression below and Figure 3.4).

As mentioned above, the *in vivo* lung morphometry technique developed in [1-3] is based on considering the lung on the acinar level as a set of airways of cylindrical geometry, covered by alveolar sleeves, as in Figure 3.4.

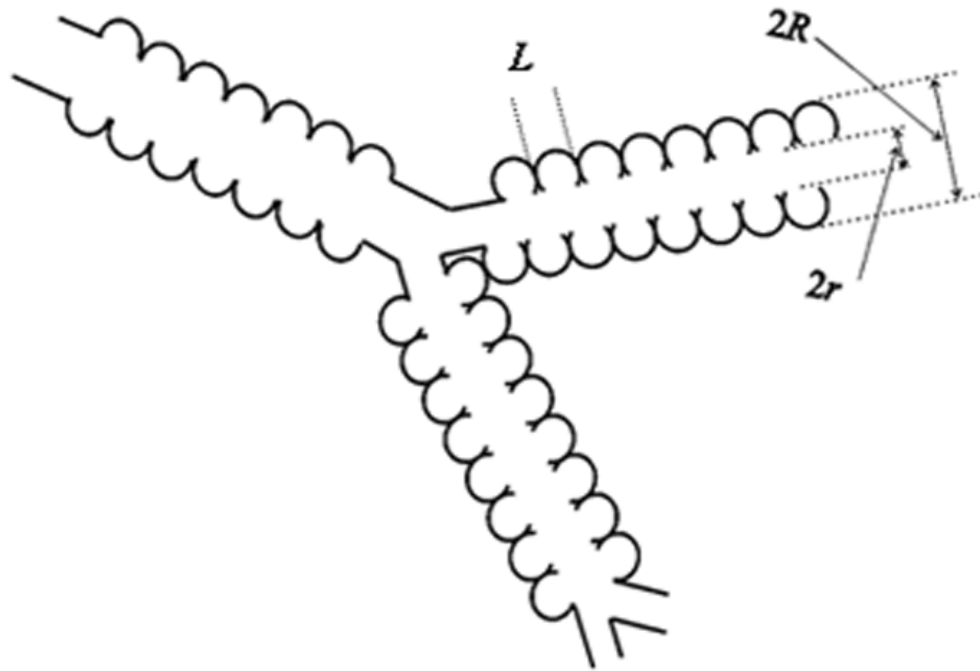


Figure 3.4: Weibel's lung model [7] [8] (based on biological structure), shown as branching acinar airways, covered with alveolar sleeve of depth $R-r$. Diffusion calculations and mathematical model is based on this lung model.

Diffusion of ^3He atoms in the airways is microscopically anisotropic and is described by two principal parameters: longitudinal (D_L) and transverse (D_T) diffusion coefficients [2]. The dependence of the MR signal on these parameters is given in Eq. (3.5). In [1], the diffusion coefficients D_L and D_T were related to the airway geometrical parameters R and b (see [1]), which made it possible to determine R and b from the diffusion attenuated multi- b MR experiments. It was further demonstrated in [3] that the airway's geometrical parameters are related to the commonly used morphometric parameters of the lung microstructure, such as mean linear intercept L_m and surface-to-volume ratio S/V .

It should be noted, however, that the relationships between D_L , D_T and R and b , obtained in [1] by means of computer simulations are not universal and are valid only within the range of the airway size R characteristic of human lungs ($R \sim 300 \mu\text{m}$). In mice, the airway radii R are substantially smaller, $R \sim 100 \mu\text{m}$. In the present study we have found modified relationships between D_L , D_T and R , b for the range of airway radii characteristic for mice and rats ($R \sim 60 - 140 \mu\text{m}$) for the pulse sequence parameters with diffusion times corresponding to smaller airway length, as used here. Specifically, the new equations are valid for $\Delta = \delta \sim 0.3-0.6$ ms. The following relationships were obtained using this approach, based on computer simulations similar to those developed in [1]:

$$\begin{aligned} D_L &= D_{L0} \cdot (1 - \beta_L \cdot b D_{L0}), \\ D_T &= D_{T0} \cdot (1 + \beta_T \cdot b D_{T0}), \end{aligned} \quad (3.6)$$

where

$$\begin{aligned} D_{L0} &= D_0 \cdot \exp[-2.99 \cdot v^{1.88}], \quad v = 1 - r/R, \quad \beta_L = 113.5 \cdot \left(\frac{R}{L_1}\right)^{1.5} \cdot \exp[-5.11/\sqrt{v}] \\ D_{T0} &= D_0 \cdot F(R) \cdot [1 + u(R, r)], \quad F(R) = \frac{7}{16} \cdot x^{(4-3.63 \cdot x^{0.6})}, \quad x = R/L_2 \\ u(R, r) &= v^{1.75} \cdot \exp(A \cdot v), \quad A = 1.1 + 3.14 \cdot x - 18.39 \cdot x^2, \quad \beta_T = 0 \end{aligned} \quad (3.7)$$

where D_0 is the free diffusion coefficient of ^3He gas in lung airspaces. Values

$$L_1 = (2 \cdot D_0 \cdot \Delta)^{1/2}, \quad L_2 = (4 \cdot D_0 \cdot \Delta)^{1/2} \quad (3.8)$$

are the characteristic free-diffusion lengths for one and two dimensional diffusion. The relationships (3.7) are purely phenomenological; specific mathematical functions are chosen solely to fit the simulations. During the data analysis we found virtually no transverse diffusion (D_T) dependence on b -value, thus the analysis of data will be conducted with $\beta_T = 0$.

The b-value in the $12b$ diffusion attenuated MR experiment is determined by a standard relationship given in Equation 15.

With mathematical equations relating D_L and D_T to acinar airway geometrical parameters R and h (Equations (3.6)-(3.8)), we can evaluate the lung tissue surface area per alveolus S_a , lung volume per alveolus V_a , and alveolar number density N_a – the number of alveoli per unit lung volume [3] (see Figure 3.1):

$$S_a = \frac{\pi}{4} R \cdot L + \frac{\pi}{4} h \cdot (2R - h) + 2h \cdot L; \quad V_a = \frac{\pi}{8} R^2 L; \quad L = 2R \sin \frac{\pi}{8}; \quad N_a = \frac{1}{V_a} \quad (3.9)$$

Note that the volume V_a comprises both the volume of alveolar duct, $\pi(R-h)^2 L/8$, and the volume of alveolus proper, $\pi[R^2 - (R-h)^2]L/8$. Also note that here we are using the airway model with eight alveoli in the cross section [3, 9]. Using Equations (3.6)-(3.8) that relate airway geometrical parameters R and h to alveoli surface area and volume, and the well-known relationship between mean linear intercept and surface-to-volume ratio [8] we can estimate the mean chord length Lm :

$$S/V = S_a/V_a = 4/Lm \quad (3.10)$$

Using the Eqs. (3.6)-(3.8) in conjunction with multi-b MR signal measurements in mouse lung acinar airways enables calculation of the geometrical parameters R and h as well as standard morphometric parameters of lung airways: Lm , S/V , N_a - see Eqs. (3.9)-(3.10).

3.1.4 Diffusion Anisotropy in the Lung Model

From the Weibel's lung model one can see that the structure is highly anisotropic, thus we assume that diffusion in such structure will also be anisotropic with two distinct diffusion coefficients parallel and perpendicular to airway axis. This is the main assumption of the model and the associated derived mathematics. To prove this directly, we need to show that diffusion in the lung is anisotropic, deducing that lung structure is in fact anisotropic.

As the model predicts, the anisotropic character of diffusion on the microscopic level together with the presence of numerous multiple-oriented airways, lead to such a non-mono-exponential dependence of the MR signal on the b-value. This non-mono-exponential dependence could also be caused by other factors, e.g., presence of multiple spherical compartments (alveolar sacs) with a variety of sizes. Two-dimensional MR experiments, in which the diffusion sensitizing gradients are applied successively in two orthogonal directions, were proposed in the past to address similar questions [10].

In our study, we exploit the same idea expanding it to a three-dimensional sequence eliminating any potential uncertainties of the interpretation of the two-dimensional experiment.

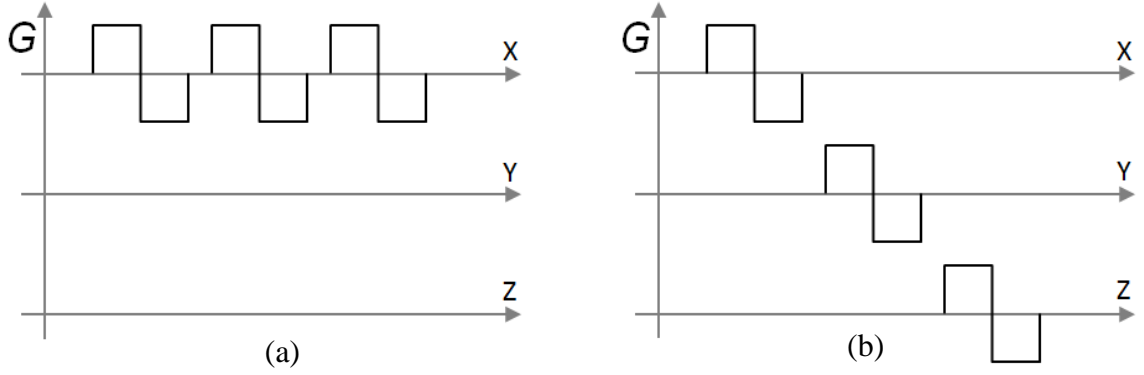


Figure 3.5: The sequence in (a) has three consecutive bi-polar gradients along the x axis, referred to as the XXX sequence, exploiting only diffusion along the X axis. Similarly, the sequence in (b) is the XYZ sequence, and exploits diffusion along all three spatial axes.

To illustrate the idea behind such an experiment, we use the following example. If we are measuring diffusion in the spherical compartments (Figure 3.6a), where diffusion in all directions is the same ($D_x=D_y=D_z$), using the sequence in Figure 3.5a, where we apply three consecutive gradients in one spatial direction along the X axis, the MR signal (labeled S_{XXX} , denoting repetitive diffusion measurements in X direction) will be proportional to:

$$S_{XXX} \sim e^{-b \cdot D_x} \cdot e^{-b \cdot D_x} \cdot e^{-b \cdot D_x} = e^{-3b \cdot D_x} \quad (3.11)$$

Using a sequence that exploits the diffusion in all three directions for this spherical compartment, as in Figure 3.5b, the MR signal will be proportional to:

$$S_{XYZ} \sim e^{-b \cdot D_x} \cdot e^{-b \cdot D_y} \cdot e^{-b \cdot D_z} \quad (3.12)$$

Given that the diffusion coefficient is the same in any direction for a spherically shaped object, the last equation, Eq. (3.12), effectively becomes equal to Eq. (3.11):

$$S_{XYZ} \sim e^{-b \cdot D_x} \cdot e^{-b \cdot D_y} \cdot e^{-b \cdot D_z} = e^{-b \cdot D_x} \cdot e^{-b \cdot D_x} \cdot e^{-b \cdot D_x} = e^{-3b \cdot D_x} \quad (3.13)$$

e.g., both sequences, Figure 3.5a and Figure 3.5b will measure the same MR signal in multiple spherical compartments of various sizes.

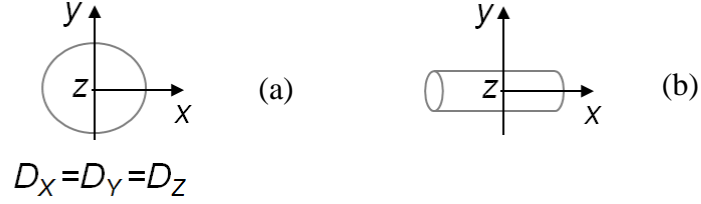


Figure 3.6: If alveolar structure in the lungs can be mimicked as a series of spherical compartments of various sizes, (a), the diffusion in all directions will be equal. If lung microstructure is modeled as cylinders (acinar airways), as in (b), the diffusion will be anisotropic.

Similarly, if we are measuring diffusion in the cylindrical compartments (Figure 3.6b), where diffusion along the X axis differs from those along Y and Z axis, using the XYZ sequence (Figure 3.5b), the MR signal will be proportional to:

$$S_{XYZ} \sim e^{-b \cdot D_x} \cdot e^{-b \cdot D_y} \cdot e^{-b \cdot D_z} \quad (3.14)$$

Given that diffusion coefficients along the Y and Z axis are the same, $D_y = D_z$, and $ADC = (D_L + 2D_T) / 3$, the above expression becomes:

$$S_{XYZ} \sim e^{-b \cdot D_x} \cdot e^{-2b \cdot D_y} = e^{-3b \cdot ADC} \quad (3.15)$$

If our sequence gradients are XXX, as in Figure 3.5a, then we are proportionally measuring:

$$S_{XXX} \sim e^{-b \cdot D_x} \cdot e^{-b \cdot D_x} \cdot e^{-b \cdot D_x} = e^{-3b \cdot D_x} \quad (3.16)$$

This result is clearly different from Eq. (3.15). Hence, conducting the two types of experiments – XXX and XYZ allows distinguishing between the two types of structures – spherical and cylindrical. Averaging Eq. (3.16) with respect to airways orientations, the signal for the XXX sequence is becoming similar to Eq. (3.5) and is proportional to:

$$S_{xxx} \sim \exp(-3b \cdot D_T) \left(\frac{\pi}{12bD_{AN}} \right)^{1/2} \cdot \Phi \left[(3bD_{AN})^{1/2} \right], \quad D_{AN} = D_L - D_T \quad (3.17)$$

It can be proven that Eqs. (3.15) and (3.17) will yield different results, e.g.. it can be shown that for any value of b , $S_{xyz} < S_{xxx}$.

3.2 SNR Optimization of MR in Mouse Lungs

When working with ^3He gas, where polarization is not recoverable, one needs to be aware of the fact that with each RF pulse, the available signal is decreasing. In addition to that, the signal will be decreasing due to various mechanisms, though we will not consider any of these, assuming the experiments are conducted rapidly with respect to T1 decay of hyperpolarized ^3He gas in the Tedlar bag.

A typical gradient echo experiment will utilize a number of RF pulses, as mentioned in the section “Theory of Gas Diffusion in Mouse Lungs”, for each one to interrogate the diffusing ^3He gas nuclear spins with the small flip angle of the RF pulse. The magnitude of the RF flip angle is directly proportional to the MR signal received. For conducting experiments in mouse lungs, where airways are tiny and the hyperpolarization decays faster, SNR optimization is of high importance. Correct choice of flip angle will help consume right amount of polarization with the rapid train of RF pulses, and obtain maximum possible S/N ratio. In addition to the flip angle, we will “encode” the spins with the gradient pulses, further deteriorating the MR signal: the higher the b-value/gradient strength, the more MR signal attenuation will be exhibited. In our experiment, we apply 12 RF pulses, first one with no b-value ($b=0$ [s/cm²]), then 10 RF pulses with changing b-value, and the last pulse again

with $b=0$ [s/cm²]. Having two measurements with $b=0$, at the beginning and at the end of the pulse sequence, allows for accurate calibration of RF pulses. To better utilize the MR signal from such an experiment, the b-values are applied in the descending order. In other words, the sequence of 12 RF pulses has the following b-values: 0, 10, 9, 8, 7, 6, 5, 4, 3, 2, 1, 0 [s/cm²]. This ensures that when ³He gas polarization is fresh and strong to apply the highest b-value and at the end of the sequence, where polarization is weakest, we apply the smallest gradient. This strategy produces a more uniform MR signal pattern and vastly better SNR as opposed to a standard strategy with generally applied ascending order of b-values.

Equation (3.18) gives the amount of the magnetization left along the Z axis after applying the train of RF pulses in the overall sequence, in this case $n=12$

$$M = M_0 (\cos \alpha)^n \quad (3.18)$$

We chose the flip angle α such that some $\sim 25\%$ magnetization is left after applying the train of 12 RF pulses. The reason for this approach is to ensure enough magnetization along the Z axis to produce and capture an adequate signal for the last RF pulse, even if the flip angle is slightly miscalculated.

3.3 References

1. **Sukstanskii, A.L. and D.A. Yablonskiy**, In vivo lung morphometry with hyperpolarized ^3He diffusion MRI: theoretical background. *J Magn Reson.* **190**(2): p. 200-10, 2008.
2. **Yablonskiy, D.A., A.L. Sukstanskii, J.C. Leawoods, D.S. Gierada, G.L. Bretthorst, S.S. Lefrak, J.D. Cooper, and M.S. Conradi**, Quantitative in vivo assessment of lung microstructure at the alveolar level with hyperpolarized ^3He diffusion MRI. *Proc Natl Acad Sci U S A.* **99**(5): p. 3111-6, 2002.
3. **Yablonskiy, D.A., A.L. Sukstanskii, J.C. Woods, D.S. Gierada, J.D. Quirk, J.C. Hogg, J.D. Cooper, and M.S. Conradi**, Quantification of lung microstructure with hyperpolarized ^3He diffusion MRI. *J Appl Physiol.* **107**(4): p. 1258-65, 2009.
4. **Haefeli-Bleuer, B. and E.R. Weibel**, Morphometry of the human pulmonary acinus. *Anat Rec.* **220**(4): p. 401-14, 1988.
5. **Rodriguez, M., S. Bur, A. Favre, and E.R. Weibel**, Pulmonary acinus: geometry and morphometry of the peripheral airway system in rat and rabbit. *Am J Anat.* **180**(2): p. 143-55, 1987.
6. **Stejskal EO, T.J.**, Spin Diffusion Measurements: Spin Echoes in the Presence of a Time-Dependent Field Gradient. *J Chem Phys.* **42**(1): p. 288-292, 1965.
7. **Weibel E.R.**, *The Lung: Scientific Foundations*, ed. W.J.B. Crystal R.G., Barnes P.J., Cherniack N.S. 1991: Raven, New York. 711-720.
8. **Weibel ER**, *Stereological Methods. Vol.2: Theoretical Foundations.* Vol. 2. 1980: London: Academic Press.
9. **Hartroft, W.S.**, The Microscopic Diagnosis of Pulmonary Emphysema. *Am J Pathol.* **21**(5): p. 889-903, 1945.
10. **Mitra, P.P.**, Multiple wave-vector extensions of the NMR pulsed-field-gradient spin-echo diffusion measurement. *Phys Rev B Condens Matter.* **51**(21): p. 15074-15078, 1995.

Chapter 4 - Materials and Methods: Hyperpolarized ^3He Gas Delivery

4.1 Delivery of ^3He Gas

The ^3He gas was hyperpolarized by the spin-exchange technique [1] using a lab-built polarizer or a IGI.9600.He commercial polarizer (General Electric Medical, Fairfield, CT) to achieve polarization levels of approximately 40%. The hyperpolarized gas from the nearby polarizer was transported in a 1 L Tedlar bag to the fringe field of the MRI scanner.

Given the small size of mouse lungs and the small TLC (total lung capacity) of the lungs, 1 ml, an accurate, fast and repeatable delivery of the ^3He gas is of high importance to the successful gas diffusion measurements. Additionally, contact with paramagnetic oxygen has a strong depolarizing effect on hyperpolarized ^3He gas, and substantially reduces the ^3He gas T1 relaxation time constant [2]. Thus, it was important to reduce the amount of residual oxygen in the lungs before and during delivery of a ^3He gas bolus. To achieve that objective, we needed to develop a method and apparatus for controlled delivery of pure ^3He gas, while minimizing contact with oxygen and the consequential loss of polarization.

4.1.1 Gas Delivery Apparatus

The gas delivery apparatus for purging and delivering gas was assembled using six valves (Figure 4.1). Briefly, the system consists of three syringes, six stopcocks (two on-off and four 3-way valves), a pressure gauge (0-30 cmH₂O), and a Tedlar bag to hold hyperpolarized ^3He gas. The syringe close to the pressure gauge is filled with nitrogen and serves to purge the

gauge line. The N_2 syringe close to the lungs serves to purge the valve manifold to remove oxygen that enters the manifold after the lungs are disconnected for scanning. The 3He syringe, close to the 3He gas bag delivers the 3He gas to the lung. To minimize the amount of 3He gas that will be depolarized due to interaction with the walls of small diameter lines, all 3He gas line connections are made as short as possible (about 14 cm long). To ensure repetitive inflation to the same pressure, a conventional pressure gauge for respiratory research was used.

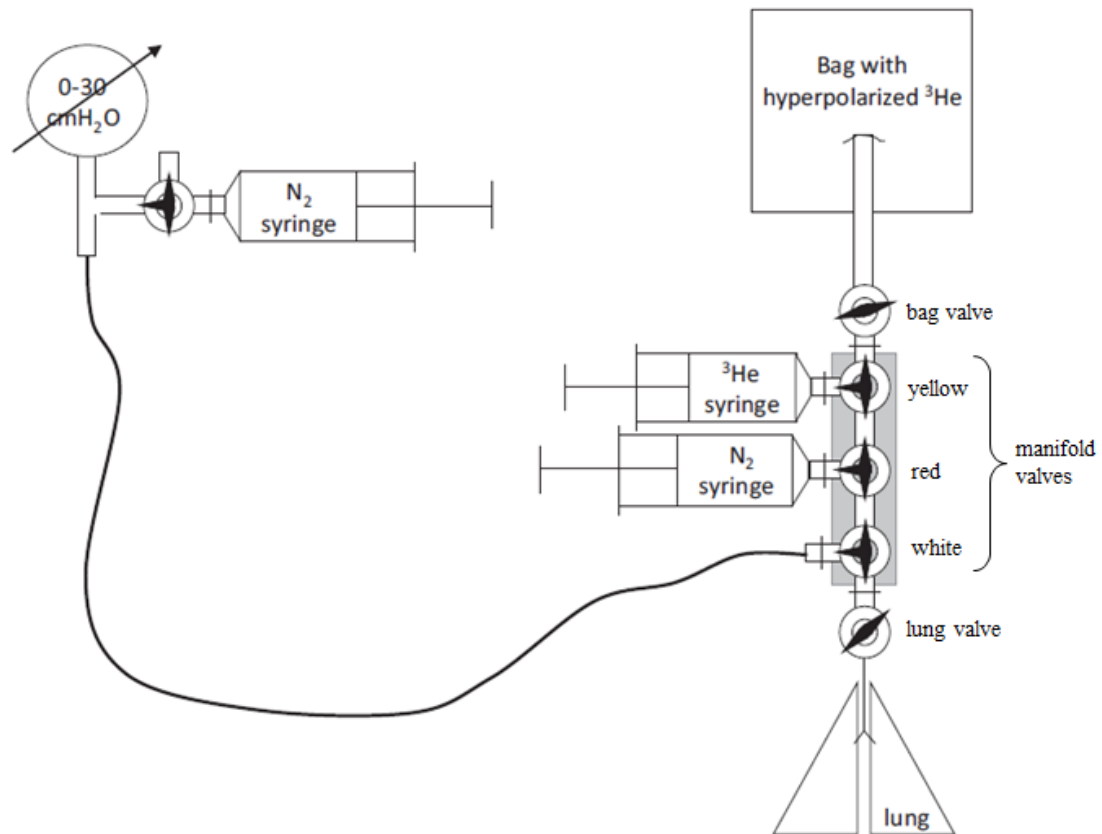


Figure 4.1: The block diagram of MRI-compatible (with the exception of the low-pressure pressure gauge), manual 3He gas delivery six-valve apparatus. The purpose is to allow the lungs to be purged of air multiple times using N_2 and then filled with the 3He for the NMR measurement of diffusion. The 180 cm long line keeps the pressure gauge containing ferromagnetic parts out of the scanner's fringe field.

The gas delivery system is put together with off the shelf standard small tubing parts, using various fittings to reduce tubing to different sizes, and standard lab syringes (5ml for all three syringes, two N₂ and one ³He gas syringe). The pressure gauge is ferromagnetic, thus the long line, to keep it outside of the fringe field of the magnet. The gauge was tested and confirmed to repetitively and accurately measure pressures outside of the fringe field of the scanner. All other parts don't contain any metal parts, be it magnetic or ferromagnetic.

4.1.2 Delivery Method and practice

The 1 L Tedlar bag with ³He (this is ³He gas at thermal equilibrium, not hyperpolarized) was connected to the six-valve setup. The pressure gauge and the lung valve were connected to the six-valve gas delivery setup (Figure 4.1 and Figure 4.2).

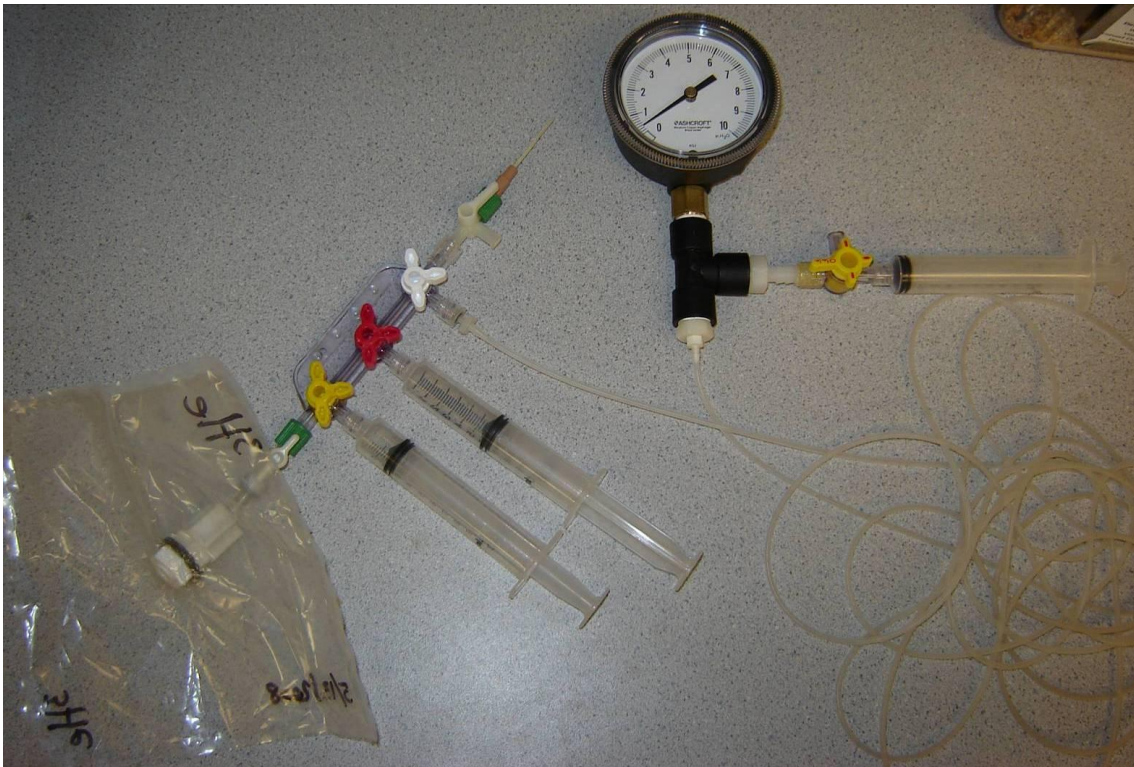


Figure 4.2: The ³He gas, six-valve delivery apparatus. The image shows manifold with three color-coded valves (as described in the block diagram), the plastic cannula connected with

the lung valve, long line to connect the low pressure gauge and the Tedlar bag connected with the bag valve.

Using the colored valves, the setup was purged of oxygen (see Table 4.1 for all the actions in the gas delivery process and the valve positioning). In essence the purging is done by taking ~5 ml of the depolarized ^3He gas with the ^3He syringe from the Tedlar bag and purging it to the atmosphere through the white valve. To remove any oxygen from connecting N_2 syringe to the setup, a several milliliters of the N_2 gas were purged through the same white valve, closed immediately upon purging. The long pressure gauge line was purged using the dedicated N_2 syringe at the gauge, venting again through the same white valve (Figure 4.1 and Figure 4.2).

Once the system is purged, the catheterized lungs were immobilized in the center of the ^3He coil and connected to the six-valve setup. The air in the lungs must be purged as a last step prior to delivery of hyperpolarized gas. Using the same depolarized pure ^3He gas in the Tedlar bag, the lungs are purged 5 times to 30 cm H_2O pressure, to remove oxygen. This procedure ensures that the concentration of ^3He gas in lungs will be practically the same (close to 100%) for all experiments. At this pressure (30 cm H_2O) the typical volume of the C57 mouse lungs is ~1 ml [3].

After the lungs were purged, a Tedlar bag with freshly polarized ^3He gas is brought to the fringe field of the MRI scanner and connected to the six-valve setup, replacing the bag of depolarized ^3He gas. After the lung purging, lungs are inflated in two stages. The first 850 μl of gas delivered to the lung is the hyperpolarized ^3He gas. Using the correct position of the valves at each step, the ^3He gas is taken from the Tedlar bag and then followed by ~150 μl

N_2 , as the second stage. The purpose of this N_2 blanket is to replace 3He gas in the large conducting airways (non-acinar portion of the lungs, typically 11% of mice lungs) [4] with N_2 , minimizing the MR signal contribution from large airways and focusing the measurement on the acinar portion of the lungs.

Table 4.1: The block diagram of MRI-compatible (with the exception of the low-pressure pressure gauge), manual 3He gas delivery six-valve apparatus. The purpose is to purge the lungs of air multiple times using 3He (at thermal equilibrium). After that, the lungs are filled with the HP 3He gas first and topped with $\sim 150 \mu l$ of N_2 for the NMR measurement of diffusion. The 180 cm long line keeps the pressure gauge containing ferromagnetic parts out of the scanner's fringe field.

step		valve						action
		bag	yellow	red	white	lung	gauge	
1	connect 3He bag	closed	closed	closed	closed	closed	closed	none
2	purge manifold w/o lungs, 1	closed	3He -red	yellow-white	open	open	closed	deliver 2 ml of 3He gas
3	purge manifold w/o lungs, 2	closed	closed	open	open	open	closed	deliver 2ml of N_2 gas
4	purge pressure gauge line	closed	closed	closed	gauge-lung	open	closed	deliver 5ml of gauge N_2
5	purge lungs, 1	open	3He -bag	closed	open	open	closed	get 2ml of 3He gas
6	purge lungs, 2	closed	3He -red	yellow-white	red-lung	open	closed	deliver/pull 1ml of 3He gas
7	purge lungs, 3	closed	closed	N_2 -white	red-lung	open	closed	crack 3He syr and purge
8	connect HP 3He bag	closed	closed	closed	closed	closed	open	none
9	purge HP 3He connecting tube 1	open	3He -bag	closed	closed	closed	open	get 2ml of HP 3He gas
10	purge HP 3He connecting tube 2	closed	3He -bag	closed	closed	closed	open	crack 3He syr and purge
11	take HP 3He gas to syringe	open	3He -bag	closed	closed	closed	open	intake 5 ml of HP 3He gas
12	deliver HP 3He gas to lungs	open	3He -bag	yellow-white	open	open	open	deliver 850 ul of HP 3He gas
13	top HP 3He with N_2 gas	open	closed	N_2 -white	open	open	open	deliver 150 ul of N_2 gas
14	disconnect lungs	open	closed	N_2 -white	closed	closed	open	RF coil w/lungs for scanning

As oxygen is one of the main culprits of reduced SNR, a detailed protocol and process steps have been devised to purge all possible oxygen from the system and to keep it out while delivering the two stage lung inflation (see Table 4.1). This also ensured standardization of the steps, reduced variability between experiments (e.g. same protocol for each of the steps) or more precisely, repeatable delivery of hyperpolarized 3He gas with the consistent lung inflation and precise topping with the N_2 gas blanket.

It was important to conduct the experiments fast and accurate. After practicing the gas delivery to lungs for 2-3 weeks, the motions and steps became a routine and added to the repetitiveness of the experimentation, reducing undue variability due to human errors or imperfections.

4.2 Animal Preparation

All experiments were approved by the Washington University Animal Study Committee. We used both lungs excised from freshly sacrificed mice (C57BL/6N, males, 3-4 months of age, kept providing food and water ad libitum, weight between 21-27 grams).

4.2.1 Animal surgery to remove lungs

All surgeries were performed in the dedicated surgery room, using the same set of standard surgery tools and same method described below. Before removing lungs, each animal was weighed for later comparison. The anesthetics and all tools were prepared prior to the surgery, to ensure lungs are freshly excised – shortest time from the euthenization of the animal to the excised lungs, intubated and ready to be scanned. Mouse is first anesthetized with 2.5% isoflurane. This is done to minimize any pain that a mouse could experience and to enable accurate delivery of the anesthetics to the desired location. Once anesthetized, the mouse is intraperitoneally injected with an overdose of anesthetics, 0.1 ml of Ketamine cocktail (0.15 ml of Xylazine, 1.0 ml of Ketamine and 4.6 ml of sterile saline). The anesthetic cocktail euthanizes the animal. Intraperitoneal injection is preferred with the small animal as young mice for the ease of the administration as compared with other parenteral methods, specifically intravenous injection.

Once euthanized, the mouse chest cavity was cut open carefully, paying a close attention not to pierce the lungs, as they would not hold the pressure and experiment of measuring the diffusion in lungs would not be possible.



Table 4.2: The CL57BL/6N mouse strain, euthanized and secured on the surgery table: after the light anesthetic, the mouse is delivered an over dose of Ketamine cocktail (0.15 ml of Xylazine, 1.0 ml of Ketamine and 4.6 ml of sterile saline) and euthanized. The animal is ready for the lungs to be extracted and intubated with a plastic needle.

With the chest cavity open, the aorta was cut to exsanguinate the animal - clean chest cavity facilitates the lung excision. The trachea was exposed and the lungs were excised, paying particular attention not to damage the lobes or the trachea. For our experiment, we need to scan lungs only, and not any other tissue; this will also minimize an undue loading on the RF

coil. With that objective in mind, we removed the heart and any surrounding tissue and fat from the lungs, again paying close attention not to damage the lungs.



Figure 4.3: On the left hand side is freshly extracted mouse lungs with heart and all excess tissue removed. Size relation to a US quarter demonstrates the challenge of size when working with mouse lungs. On the right hand side, the same lung intubated, double ligated, and inflated with 1 ml of air, approximately the total volume of mouse lungs.

4.2.2 Intubating lungs, fixing in the coil

The mouse trachea is very small. To deliver the ^3He gas to it, we needed to use a non-metallic object on whose end we could mount a valve (to keep the hyperpolarized ^3He gas in the lungs during the scanning process). Thus, the trachea was catheterized using a plastic needle and double ligated [5] to ensure both a tight seal and the physical stability. Sound physical structure is needed as we will pull on the needle to connect the ^3He bag to it, each time we deliver a new batch of HP ^3He gas.

We also made sure not to over tight when ligating as that would reduce already small radius of the plastic needle, potentially negatively impacting flow and hyperpolarization of the ^3He gas. Also, more tight than needed, the ligation had tendency to cut through the trachea tissue and split it. The worst case scenario was to ligate so tight to completely obstruct the flow of ^3He gas and render the setup unusable. It was important to make sure the lungs are not intubated with the completely obstructed needle. Remediating any potential problems with the path of the gas delivery was diagnosed and fixed prior to getting HP ^3He gas delivered in scanner's proximity: the gas polarization would continually decrease and negatively impact the SNR for an experiment. Once lungs properly intubated, and the other end of the plastic needle was sealed with a stopcock valve, the intubation was tested with 1ml syringe: 1 ml of air was delivered into the lungs, the valve was closed ensuring there were no leaks in the lungs (e.g. lungs not pierced or cut), intubation or valve. Then, the valve was vented to the air to make sure the lungs would deflate on its own. After this procedure, the lungs were properly secured in the ^3He coil, ready for the HP ^3He gas delivery and scanning. The lung valve is kept outside of the coil for easy connectivity of our gas delivery setup.

4.2.3 Problems incurred during animal procedures

Working with such a delicate organ like lungs, from such a small and delicate animal as mouse, increases the likelihood of mishaps and mistakes and calls for extra caution during the surgery and the intubation procedure. Several recurring problems affected the procedures from time to time; however in general we were getting better results as the experience was acquired. The problems include piercing the lungs, not forming a good seal with the trachea, cutting the trachea with the thread, obstructing the flow through the plastic

needle with over tightening thread or intubating into one branch of the trachea (needle put too far into the bi-furcation of trachea, ending up in one side of the lungs).

By far the greatest obstacle was piercing the lungs. In this case we would not be able to use the lungs. The next one was lungs that leak. Leaks could be caused by various reasons, small cuts, not a good seal, seal loosening after a few times delivering the ^3He to the lungs or lungs stiffening and breaking. In general small leaks, or micro-leaks, where the change in lung volume is negligible relative to the duration of the scanning time (eg, lung would lose half the pressure in 2+ min), did not affect the data collected and only slightly, less than 15% impacted the SNR.

To eliminate the occurrence of leaky seal between the trachea and the plastic needle, at the time of initial testing of the lungs for proper inflation with the air, a droplet of water is placed around the seal to ensure no leaks. Over time with practice and proper ligation, the leaks at the trachea were nearly eliminated.

4.3 References

1. **Walker, T.G. and W. Happer**, Spin-exchange optical pumping of noble-gas nuclei. *RevModPhys* **69**: p. 629-642, 1997.
2. **Saam, B., W. Happer, and H. Middleton**, Nuclear relaxation of ^3He in the presence of O_2 . *Phys Rev A*. **52**(1): p. 862-865, 1995.
3. **Soutiere, S.E. and W. Mitzner**, On defining total lung capacity in the mouse. *J Appl Physiol*. **96**(5): p. 1658-64, 2004.
4. **Irvin, C.G. and J.H. Bates**, Measuring the lung function in the mouse: the challenge of size. *Respir Res*. **4**: p. 4, 2003.
5. **Olsson, L.E., M. Lindahl, P.O. Onnervik, L.B. Johansson, M. Palmer, M.K. Reimer, L. Hultin, and P.D. Hockings**, Measurement of MR signal and T_2^* in lung to characterize a tight skin mouse model of emphysema using single-point imaging. *J Magn Reson Imaging*. **25**(3): p. 488-94, 2007.

Chapter 5 - Materials and Methods: Gradients Calibration, Eddy Currents and RF Coil

5.1 Varian MRI System

All MRI measurements were performed on an Oxford Instruments (Oxford, UK) 4.7 T horizontal bore magnet (33 cm magnet bore and 15 cm gradient bore), equipped with actively shielded high performance Varian/Magnex gradient coils capable of 60 G/cm. The scanner is equipped with the broadband capabilities allowing MR measurements at the ^3He frequency of 152.1 MHz. The operating system used was VnmrJ from Varian. The scanner system includes dedicated eddy current compensator.

5.2 Gradient Pick-up Coil and Oscilloscope

The accuracy of the measurements of the lung microstructural parameters depends in part on the performance of the gradient coils. In particular, precise gradient rise and fall times and gradient strengths should be known accurately for calculation of b-values in Equation (3.4). To measure and calibrate the gradient coil characteristics, we used an induction-based gradient pickup coil consisting of four spatially offset coils (Figure 5.1a), able to record gradients in the X and Z (or Y and Z) directions.

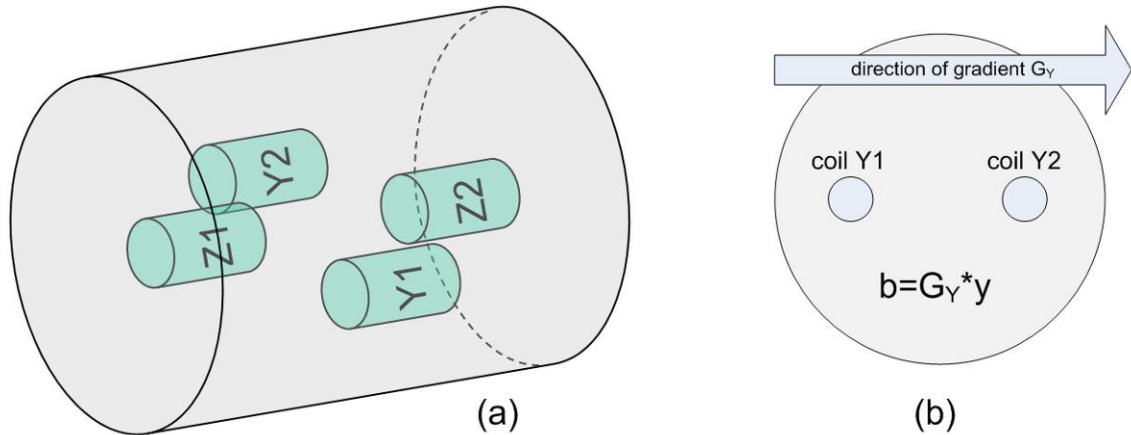


Figure 5.1: Home-built gradient pick up coil. The two pairs of coils are offset spatially along the Z axis (along the cylinder) while the other pair is offset in a perpendicular direction. The Z-gradient is obtained from Z (Z1 and Z2) coil-pair, while X- or Y-gradient are obtained from the Y (Y1 and Y2), coil pair, depending on a physical alignment of the Y coil pair inside the magnet bore, either with X axis or with the Y axis. Due to this nature of the design of the gradient coil, and given the two channel amplification in the accompanied electronic box (see Figure 5.2), one could simultaneously observe Z-X or Z-Y gradients.

Once inside the magnet's bore, the coil assembly can be rotated around the Z axis to align the pair of Y coils (Y1 and Y2) with the Y gradient or to align it with the X gradient, while coil pair Z (Z1 and Z2) is in either case aligned with the Z gradient, along the bore. The coils feed the gradient signal to electronics for time integration and display on an oscilloscope. Inside the electronic box of the gradient pickup coil, there are two identical integrator-inverting amp pairs for ability to read both gradients at the same time, be it X and Z or Y and Z, Figure 5.2.

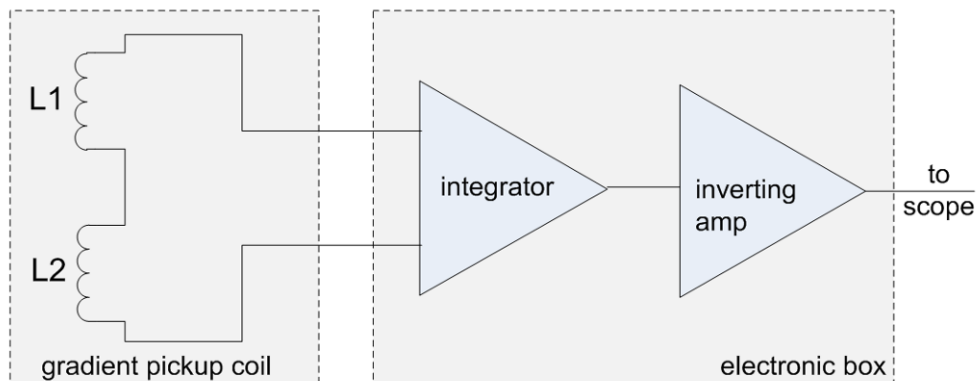


Figure 5.2: Electronic schematic of the circuitry that processes signal from one pair of gradient coils. There are two identical circuits in the electronic box, for both gradient coil pairs. In principle, L1 and L2 can represent Z1 and Z2 of Y1 and Y2 from Figure 5.1.

Using the fast digital oscilloscope, Tektronix TDS 5104, 1 GHz, and the setup above for each gradient pair we conducted the following measurements: the gradient slew rates were measured and tabulated for all three axes through the full range of gradient strengths (Figure 5.3). Virtually all three axes exhibited the same linear relationship through the entire gradient range, 0-60 G/cm. This linear relationship found in the graph (Figure 5.3) is coded into the pulse sequence to ensure the system never asks the gradient amplifiers for a more rapid gradient slew rate than what the system is capable of delivering. Once the sequence was coded to control the gradient slope, its precision and responsiveness has been confirmed using the “pickup coil – oscilloscope” setup.

In our sequence, it was important to have a uniform gradient slew rate for each of the 12 MR diffusion measurements (only 10 of them had gradients applied, all with the exception of the first and the last RF pulse.).

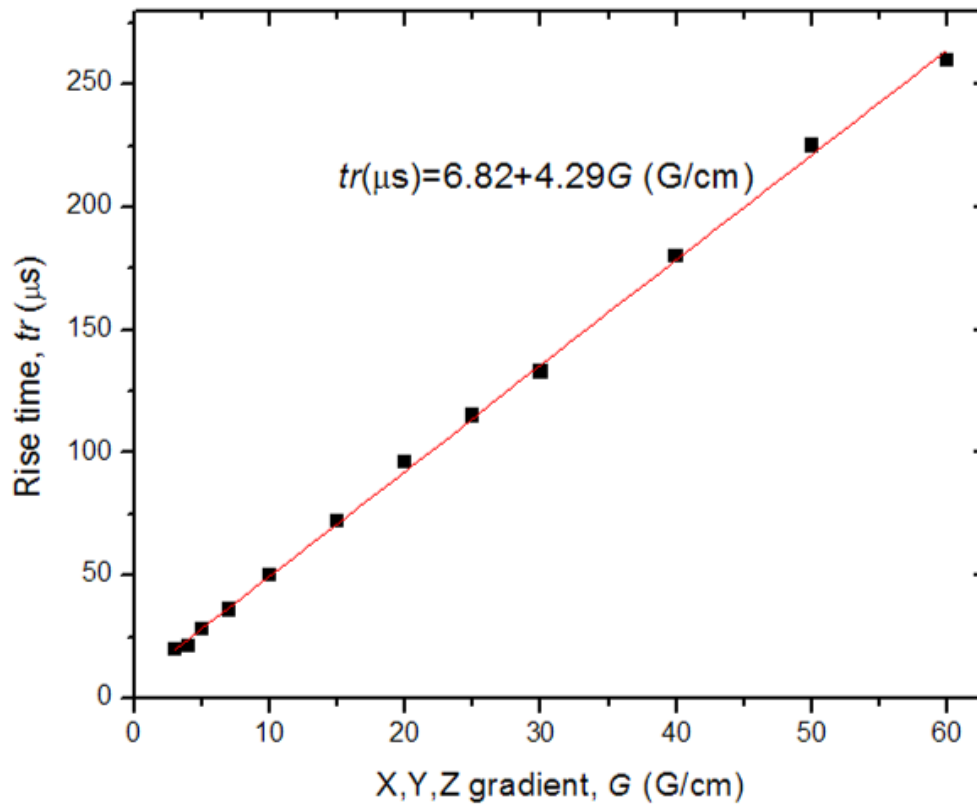


Figure 5.3: The rise times of gradient pulses through the entire range of gradient strengths. Results were identical for all three axes as for the negative gradient amplitudes. The solid curve is a fit to the data with the linear expression shown.

Figure 5.4 gives an example of the same gradient with various slew rates.

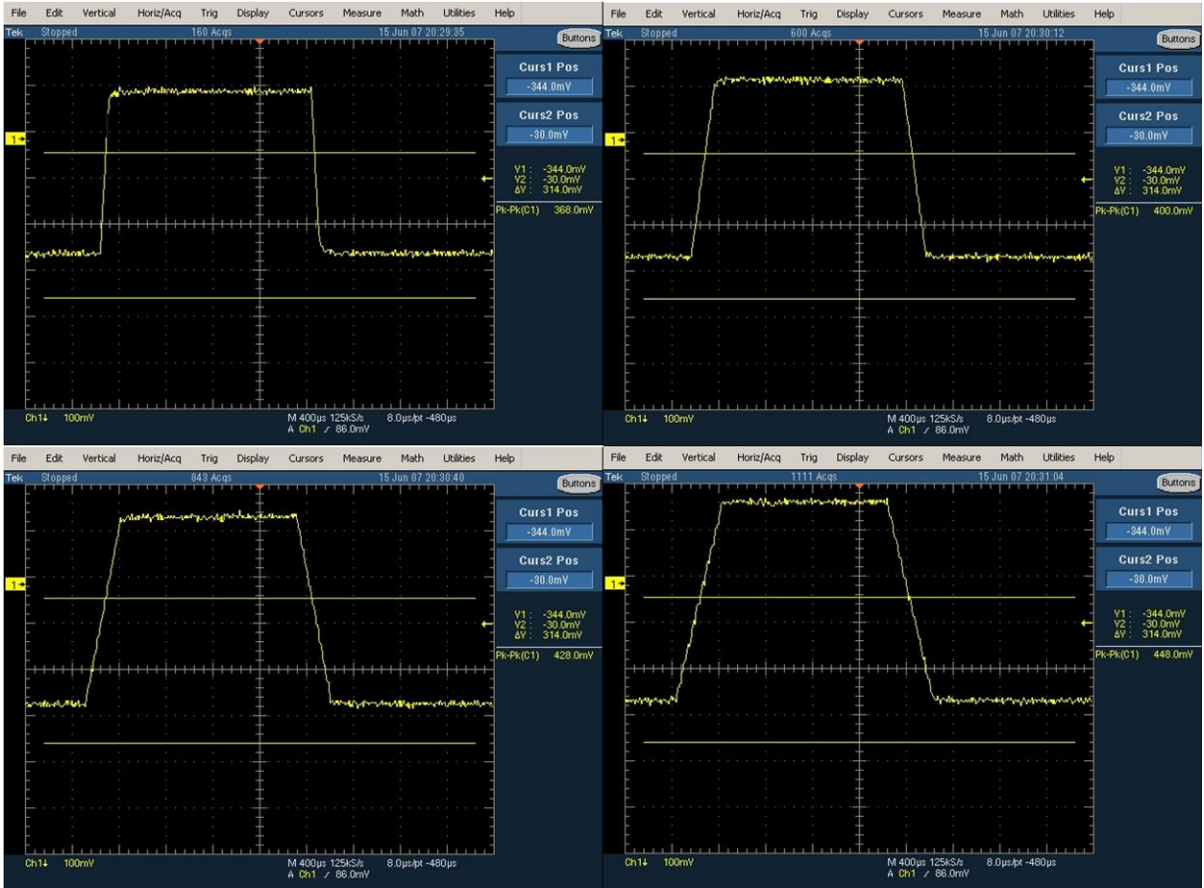


Figure 5.4: Images show the gradient pulse shapes for various rise times for X axis. Results demonstrate an excellent slope control, no ringing and the identical fall. The other two axes, Y, and Z, exhibited identical gradient pulse shapes. Some of the curvature can be noticed in the first image (top left) at the end of the fall cycle. The amount of the curvature is negligible to make a difference in our calculations. Additionally, this is the image obtained for the maximum slew rate, which we never use in our sequence, e.g. we always force the slope, particularly we used rise times in order of 100-200 μ s.

An example of the gradient wave-form used in our experiments is shown in Figure 5.5 (bipolar gradient pair) demonstrating that the calibration procedure provides an adequate gradient behavior allowing precise achievement of required b-values.



Figure 5.5: The bi-polar gradient transition region behaves well: gradient follows the prescribed waveform for both, positive and negative side. The gradient moves through the transition points without ringing or soft corners, allowing us to apply the mathematical theory for the gas diffusion in lungs with the required accuracy and confidence in results.

5.3 External Tuning Box

The external tuning box is a simple passive LC circuitry, as elaborated in Chapter II, which shifts the resonance of the ^3He RF coil. The box, when connected in series with the ^3He RF coil tunes it to the proton frequency. This allows the proton imaging and correct mouse positioning inside the ^3He coil without a need of removal when switching to ^3He gas diffusion spectroscopy or imaging. In a nutshell, inserting the tuning box between the coil and the preamplifier will move the resonance to the proton frequency of ~ 200 MHz.



Figure 5.6: External tuning box, consisting of one inductor and two capacitors, one fixed one adjustable. The adjustable capacitor is there to tune the box to the right resonance, in this case the frequency of proton (^1H).

Figure 5.7 demonstrates the value of the external tuning box: mouse proton images are obtained using the external tuning box to make the best estimate of the location of the lung cavity. Once the location is determined, the external tuning box is removed and the ^3He gas lung images are obtained.

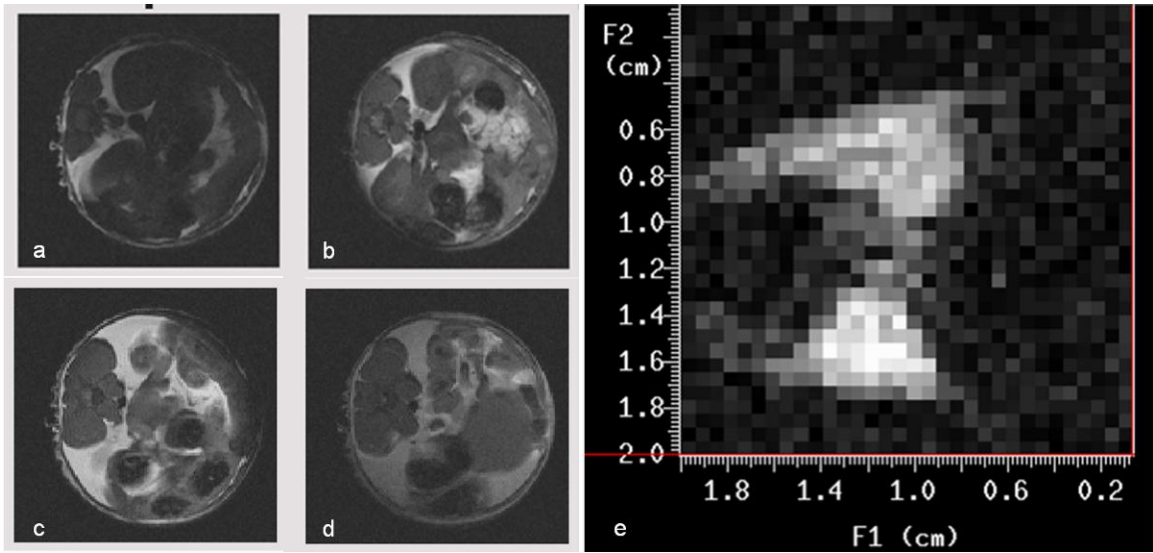


Figure 5.7: Images a-d are coronal mouse proton images, obtained using ^3He RF coil with the external tuning box connected in series, effectively re-tuning the RF coil to the proton frequency. These images are used to locate the lung cavity. The image e is the ^3He gas image of the same mouse lungs in the transverse plane, obtained using the same RF ^3He coil. All imaging planes are cited with the respect to the magnet bore.

5.4 Eddy Currents

Eddy currents are usually induced in conductors, opposing the change in magnetic field that generates them. Eddy currents are circulating flow of electrons or current within the body of conductor, in our case the gradient coils, inducing magnetic fields that oppose change of the original magnetic field [1]. The stronger the applied magnetic field, or the greater the electrical conductivity of the conductor, or the faster the changes of the magnetic field, the greater the eddy currents are developed and the greater opposing field they generate. In our case the gradient coils have a high conductivity (thick copper wire positioned in the cold magnet bore), the field is strong (up to 60G/cm) and it changes fast (few hundred microseconds for a full swing change), creating deeply fertile environment for generation of eddy currents.

Eddy currents can cause repulsive or attractive field effects as well as the heat in the body of the conductor. In our case, eddy current issue translates to concern about impact on the gradient related b-values, the quantity directly impacted by the total gradient applied.

Although there is an eddy current compensator on our Varian system, as strong and fast changing magnetic fields are used in the gradient coils it is possible to exhibit undesirable eddy current effect, causing unpredicted behavior of the gradients applied and thus the received MR signal. Additionally, mouse lungs are very small and signal to noise ratio can be negatively affected, causing diffusion measurement uncertainties. For that reason an exhaustive eddy current tests were conducted to understand their behavior and a potential impact.

Two types of test were conducted. The first one with using one positive gradient pulse whose ramp up/ramp down times were changing from 125 ms to 350 ms, followed by 150 μ s RF pulse and immediate 200 ms of acquisition time (see Figure 5.8a). This sequence was run for ten consecutive times, back to back, each time stepping up the rise/fall time of the gradient pulses by 25 ms. The MR acquisitions did not reveal any noticeable eddy current impacts for either axial direction (see Figure 5.8b). The above sequence strategy was repeated for the RF pulses of significantly longer times, 50 ms and to 3 sec, and eddy currents did not show any impact and results looked virtually the same for all directions, X, Y and Z (see Figure 5.8c, Figure 5.8d).

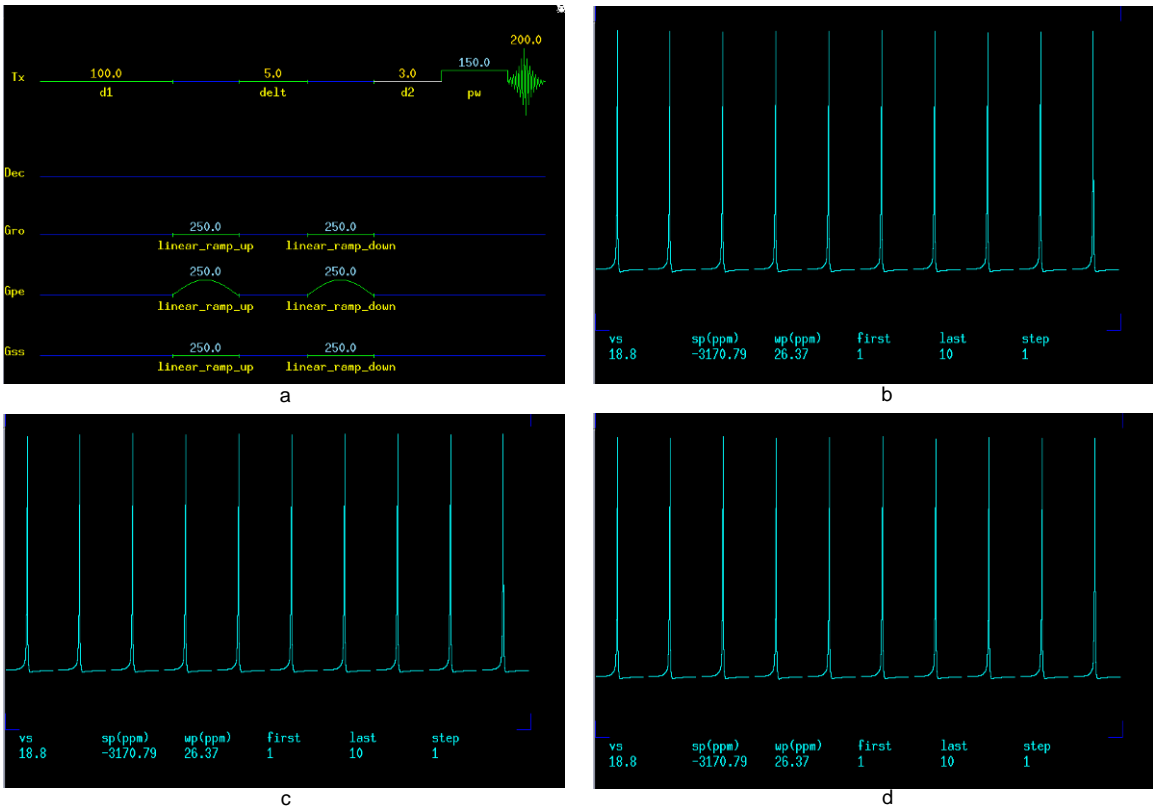


Figure 5.8: Image a shows the sequence used to explore eddy current effect while changing the ramp up/ramp down time of the gradient pulse, $grise$ [ms] = 125, 150, 175, 200, 225, 250, 275, 300, 325, 350, followed by a fixed $d2=3$ ms delay and 150 μ s RF pulse. Image b shows the MR signal for the ten RF pulses. Image c shows the result of the same sequence, now with the RF pulse of 50 ms. Image d employs the sequence with 3 s long RF pulse and reveals no eddy current effect. Images b, c, and d look exactly the same for X, Y and Z direction.

The same test from the above was repeated to more closely mimic our diffusion sequence with the bi-polar gradients (see Figure 5.9a). The bi-polar gradients mean fast shifting in polarity, however the eddy currents had no effect (see Figure 5.9b, Figure 5.9c and Figure 5.9d).

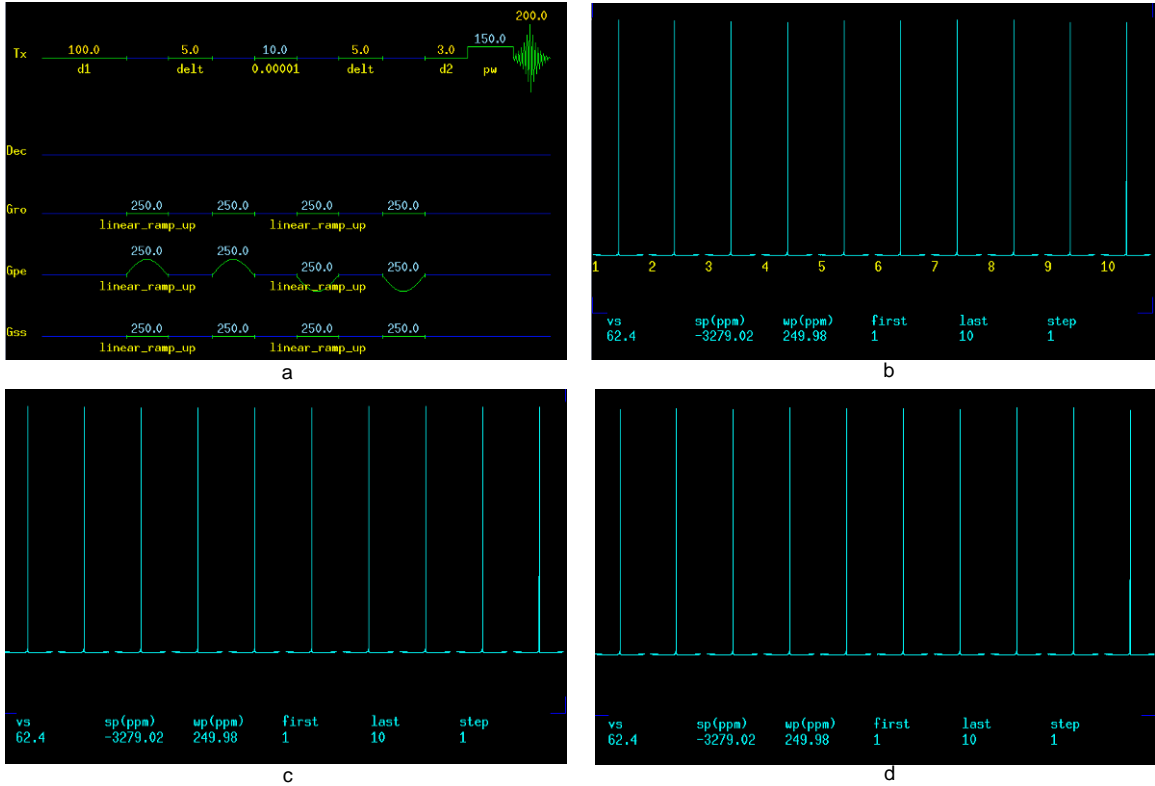


Figure 5.9: Similar to Figure 5.8, image a shows the sequence used to explore eddy current effect while changing the ramp up/ramp down time of the bi-polar gradient pulses, $grise$ [ms] = 125, 150, 175, 200, 225, 250, 275, 300, 325, 350, followed by a fixed $d2=3$ ms delay and 150 μ s RF pulse. Image b shows the MR signal for the ten RF pulses. Image c shows the result of the same sequence, now with the RF pulse of 50 ms. Image d employs the sequence with 3 seconds long RF pulse and reveals no eddy current effect. All MR signal images look identical for all three axes: X, Y and Z.

Determined to put more stress on the system to find where eddy current effect may show, we used a long gradient just before a short RF pulse and made acquisitions for all three axial directions. The sequence was simple: one positive gradient pulse (50 ms) followed by a varied delay (3 ms – 3 s) and a 10 μ s RF pulse, repeated ten times for all three axial directions (see Figure 5.10a), the results revealed impact in all three directions (Figure 5.10b, Figure 5.10c and Figure 5.10d).

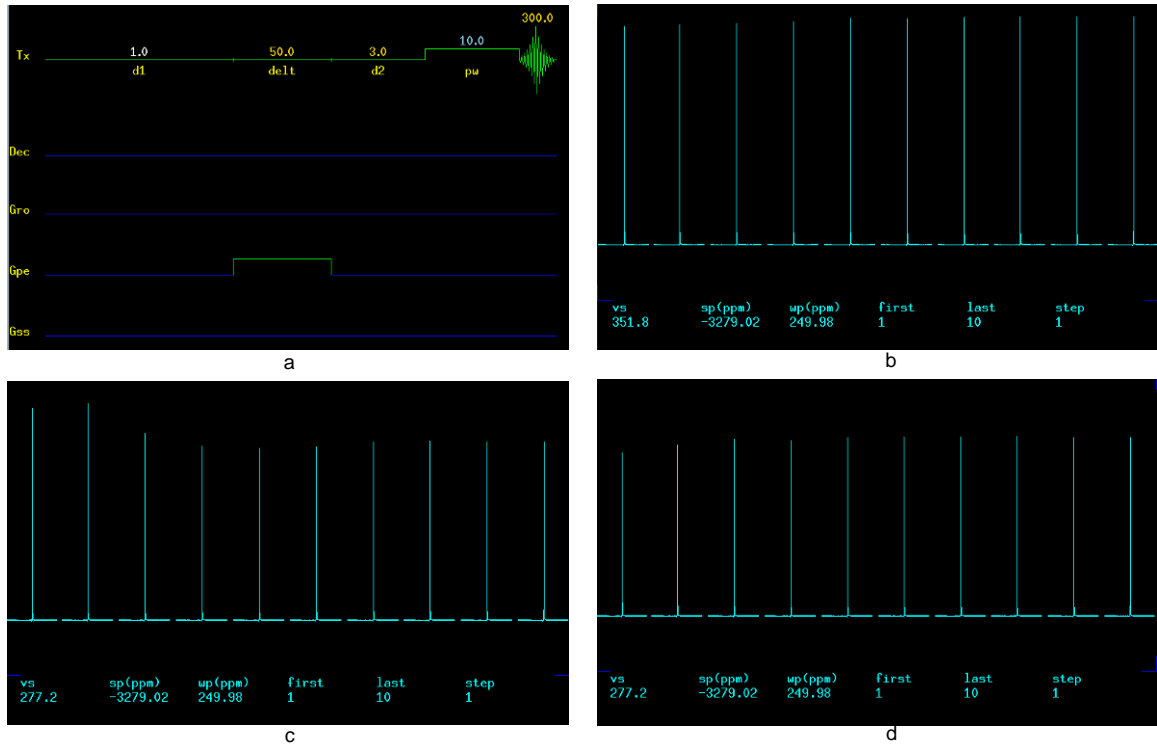


Figure 5.10: As before, image a shows the sequence used to explore eddy current effect while changing the $d2$ delay (3, 10, 50, 100, 150, 300, 600, 1000, 2000, 3000 ms), followed by a $10 \mu\text{s}$ RF pulse and a 300 ms acquisition. Image b shows the MR signal for the ten RF pulses in X direction. Image c shows the result of the same sequence, now with in Y direction and d shows the Z direction.

To exploit this weakness in our diffusion sequence, we assembled similar test using fixed rise-time bi-polar gradients, varied $d2$ delay and comparable RF pulse of $150 \mu\text{s}$ (see Figure 5.11a). The result obtained shows slight impact on the transitioning the delay from 3 ms to 10 ms (Figure 5.11b, Figure 5.11c and Figure 5.11d). For subsequent transitions, eddy currents showed no effects.

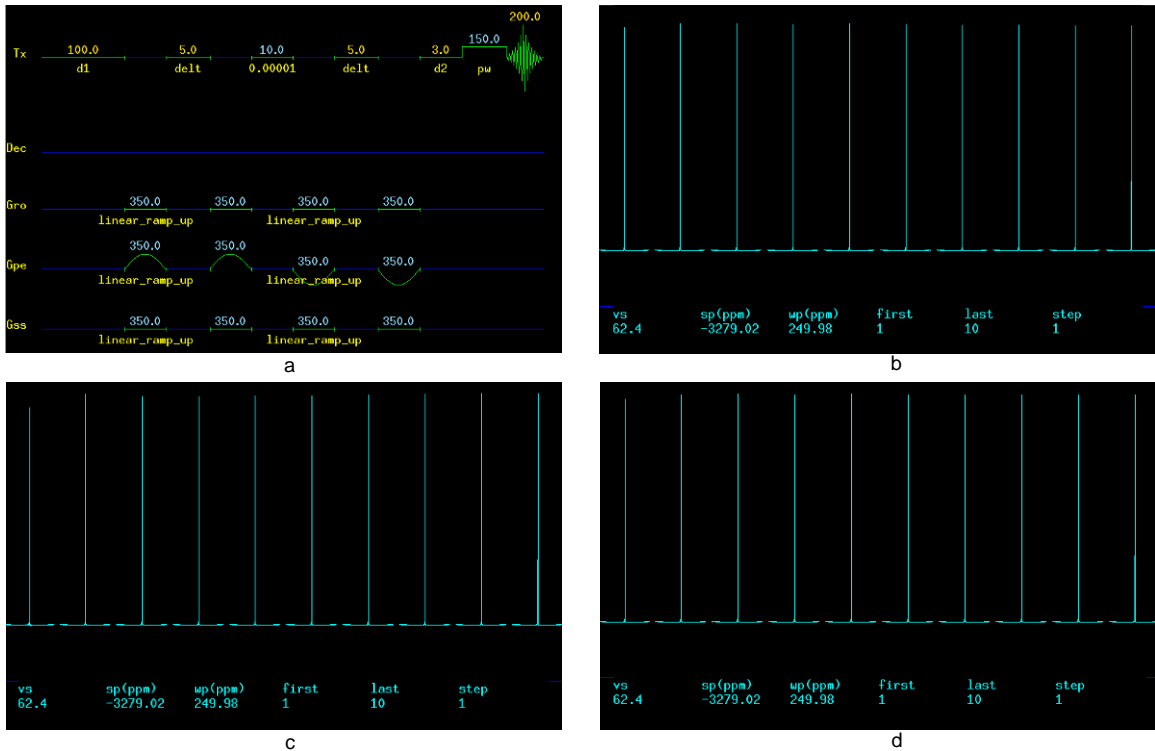


Figure 5.11: Image a shows sequence with fixed rise-time bi-polar gradients with changing the $d2$ delay (3, 10, 50, 100, 150, 300, 600, 1000, 2000, 3000 ms), followed by a 150 μ s RF pulse and a 200 ms acquisition. Image b shows the MR signal for the ten RF pulses in X direction. Image c shows the result of the same sequence, now with in Y direction and d shows the Z direction.

As it can be seen in the next chapter, for our diffusion sequence the delay $d2$ is fixed, gradient pulses are much shorter (< 0.5 ms) and we have fixed preamble delay followed up by crusher gradients, to ensure quiet eddy currents for the new sequence to be ran. Applying these strategies to alleviate issues uncovered above, we were confident that eddy currents have had minimal effects, if any.

5.5 RF Coil for ^3He

We used a lab-built small coil on a 25 mm glass tube, 5 cm in length as in Figure 5.12. The glass tube of this size is used to receive the entire mouse. Since excised lungs are much

smaller, a small padding was created to elevate the lungs to the center of the coil. The inflated lungs fill about one quarter of the cross-section of the glass cylinder. The RF coil consists of the four copper plates, bridged with the three set of capacitors and with one adjustable capacitor. This capacitor is used to adjust the resonance frequency of the coil.

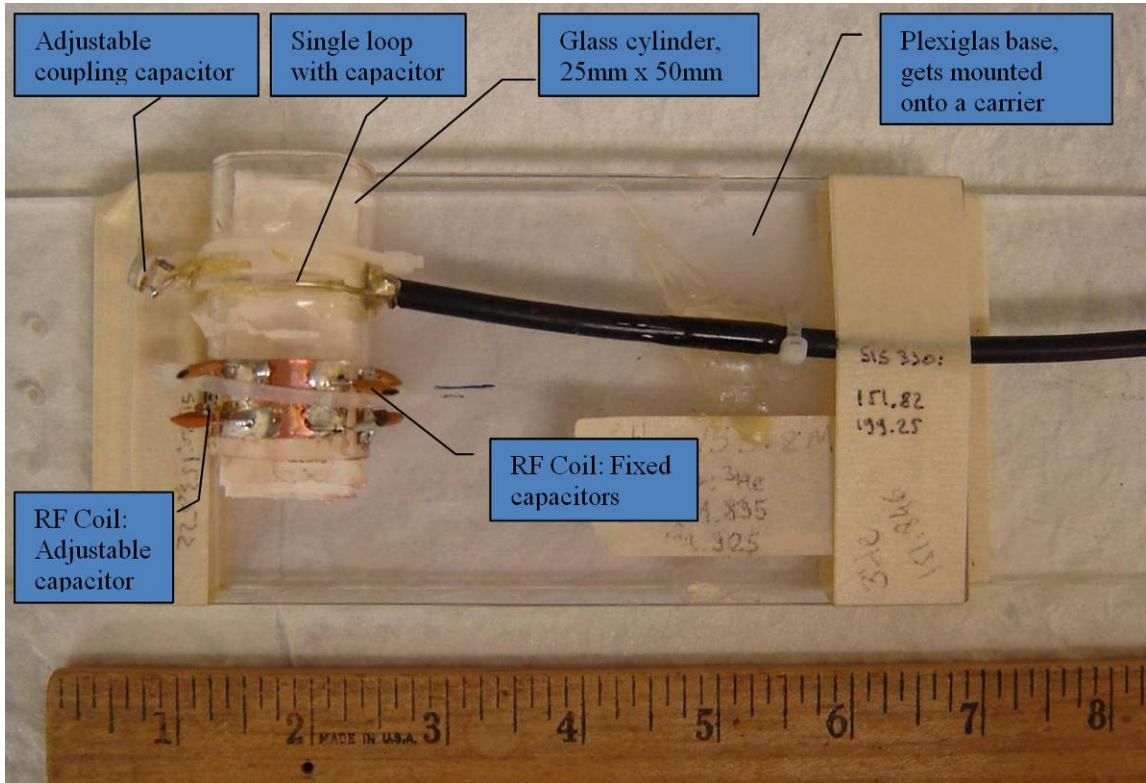


Figure 5.12: The lab-built RF coil, tuned to ^3He nuclei frequency. The coil consists of four copper plates acting as inductors connected in series with capacitors: three fixed and one adjustable capacitor. The RF coil is inductively coupled to RF amplifier using a LC circuitry: a single loop (L) terminated with a capacitor (C). The coupling is adjusted using both, the adjustable coupling capacitor and distance between the loop and the RF coil.

The adjustable capacitor has sufficient range so the coil can resonate on proton frequency (~ 200 MHz for our MRI 4.7 T Varian system) or ^3He nuclei frequency (~ 151 MHz). The resonating circuitry (RF coil) is inductively coupled to the RF amplifier using simple LC circuitry, in this case a single loop of wire terminated with a capacitor. The maximum

inductive coupling can be adjusted by changing the distance of the loop from the RF coil, as well as its L to C ratio by changing the adjustable coupling capacitor.

The whole setup is firmly affixed onto a Plexiglas base that fits snugly into a carrier that is custom made for the magnet bore. The carrier is designed to position the RF coil in the middle of the magnet in all axial directions.

The high sensitivity of the high-quality RF solenoid allows the usage of small RF tipping pulses so that many MR measurements can be obtained from a single bolus of hyperpolarized ^3He gas.

5.5.1 Network Analyzer

The coil, with the lungs as an internal load, is tuned to the ^3He gas nuclear MR frequency for our magnet strength (4.7 T) of 151.82 MHz using the network analyzer. Using the same network analyzer, the inductive coupling is tuned to the peak employing Smith chart and tuning it to center of the chart to minimize reflectance and maximize the inductive coupling.

The network analyzer is shown in Figure 5.13.



Figure 5.13: Network Analyzer, HP 8720A, used to tune the RF coil to the ^3He nuclei frequency and to adjust the inductive coupling, with the load present in the coil.

5.6 Polarization Equipment for ^3He

The ^3He gas was hyperpolarized using IGI.9600.He commercial polarizer (General Electric Medical, Fairfield, CT) to achieve high levels of polarization, approximately 40%. The polarization equipment is housed in its own room, to allow for proper safety (laser equipment), controllable environmental conditions (proper heat removal) and to accommodate for all the utilities connected to it: power, compressed air, compressed nitrogen and compressed ^3He gas.

5.6.1 Hyperpolarizing Hardware

The laser-path schematic of our hyperpolarizing equipment is shown in Figure 5.14, depicting the laser source, collimating optics and the laser beam irradiating the

hyperpolarization cell, filled with ^3He gas and liquid Rb. The cell is heated to temperature of 170°C , at which the Rb is in the gaseous state. The laser light is generated with the laser diode box. The box contains actually two diode arrays and the diodes are supplied by $\sim 36\text{ A}$ each, with

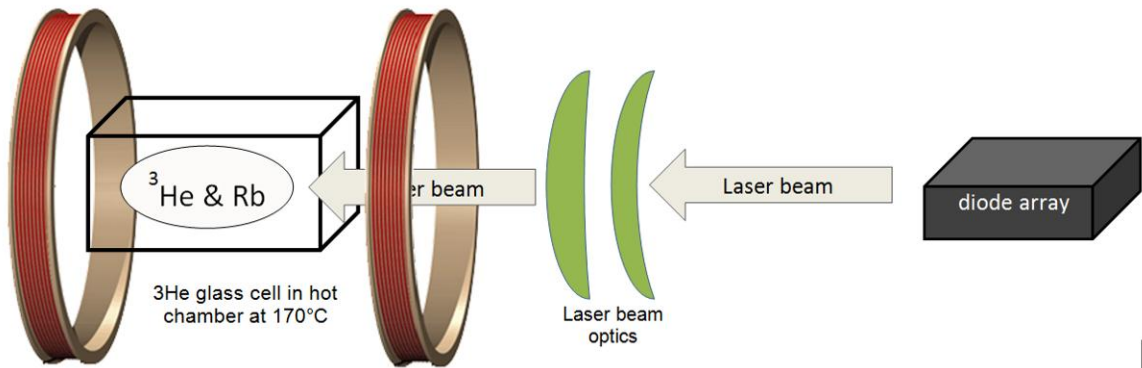


Figure 5.14: Schematic diagram of the laser source (diode array) that emits linearly polarized laser light, series of collimating lenses (to focus the light at infinity, to make the laser rays collinear) after which it is passed through the $\frac{1}{4}\lambda$ plate to make the light polarization circular. This light irradiates the cell with ^3He and Rb vapor. A fan circulates warm air around the cell in a chamber, to elevate its temperature to 170°C . The chamber is located between two Helmholtz coils that generate nearly homogeneous magnetic field.

the target to maintain temperature for both diode arrays at $\sim 12^\circ\text{C}$. The diode arrays consume a lot of energy, turning it into laser light at 795 nm , however large part of energy is dissipated as heat. Fluctuating temperature of the diodes would fluctuate the wavelength of the linearly polarized laser light [2]. To have stable wavelength of the polarized light at the constant power, the diode arrays are cooled using temperature control loop internal to the diode array box.

Laser light from gas or crystal lasers is naturally collimated because it is formed in an optical cavity between two mirrors. Laser light produced by laser diodes is not collimated [3]. This non-collimated light is then passed using polarization-maintaining optical fiber and fed into

the set of optics to collimate. The set of optics will nearly collimate the light (perfectly collimated beam with no divergence cannot be created due to diffraction, thus need to wear laser-protective glasses in the polarization room!) producing linearly polarized, collimated light. This beam of light is then passed through a $\frac{1}{4}$ wave plate to transform the laser light's linear polarization into the circular polarization. This light is entered into the heating chamber to irradiate the gas cell containing approximately 1 liter of ^3He gas mixed with nitrogen and Rb vapor. The gas cell pressure is kept at ~ 10 atm or ~ 130 psig. As the chamber is heated by introducing compressed air over the heating element, impurities from the compressed air line (oil and dust), as well as any non-metal or non-glass material in the chamber, will overtime deposit on the gas cell and the chamber window where the laser light enters, reducing the hyperpolarization effectiveness.

The gas cell and the chamber are located in the homogeneous magnetic field, maintained by a pair of Helmholtz coils using low-field strength ($\sim 50 \times 10^{-7}$ Tesla). The homogeneous magnetic field extends the T1 of the hyperpolarized ^3He to typically >24 hours [4].

5.6.1 Controls and Diagnostics

Inside the heating chamber, close to the gas cell, there is a coil that is connected to the small NMR spectrometer system. Its functionality is controlled by a PC that runs the polarizer and the results of the polarization inspections are displayed in a form of spectra. Inside the heating chamber, as the laser light goes through the gas cell it is received by a light sensor, thus the PC is capable of showing the laser light absorption and also reads the light's wavelength. With the fact that PC also controls the diode array box and can set their currents, desired temperature and turns them on or off, this setup gives a complete

diagnostic and control of the laser-path for the polarizer. Temperature of the system is controlled using individual PID (proportional-integral-derivative) controller.

The ^3He gas delivery is controlled using a few valves and manifolds (see Figure 5.15). As the compressed ^3He gas is at a very high pressure (1500 psi) in the metal tank, the ^3He gas is delivered to a small limited volume (short pipe run), from where it is metered to the glass cell making sure not to exceed 3 cfm of the gas flow to the cell, for safety reasons. The hyperpolarized gas can be dispensed from the cell or mixed with the nitrogen using the set of valves that is part of the ^3He gas piping structure. If there is a need to purge the dispensing container (in our case the Tedlar bag), the small vacuum pump provides vacuum at the point of dispensing.

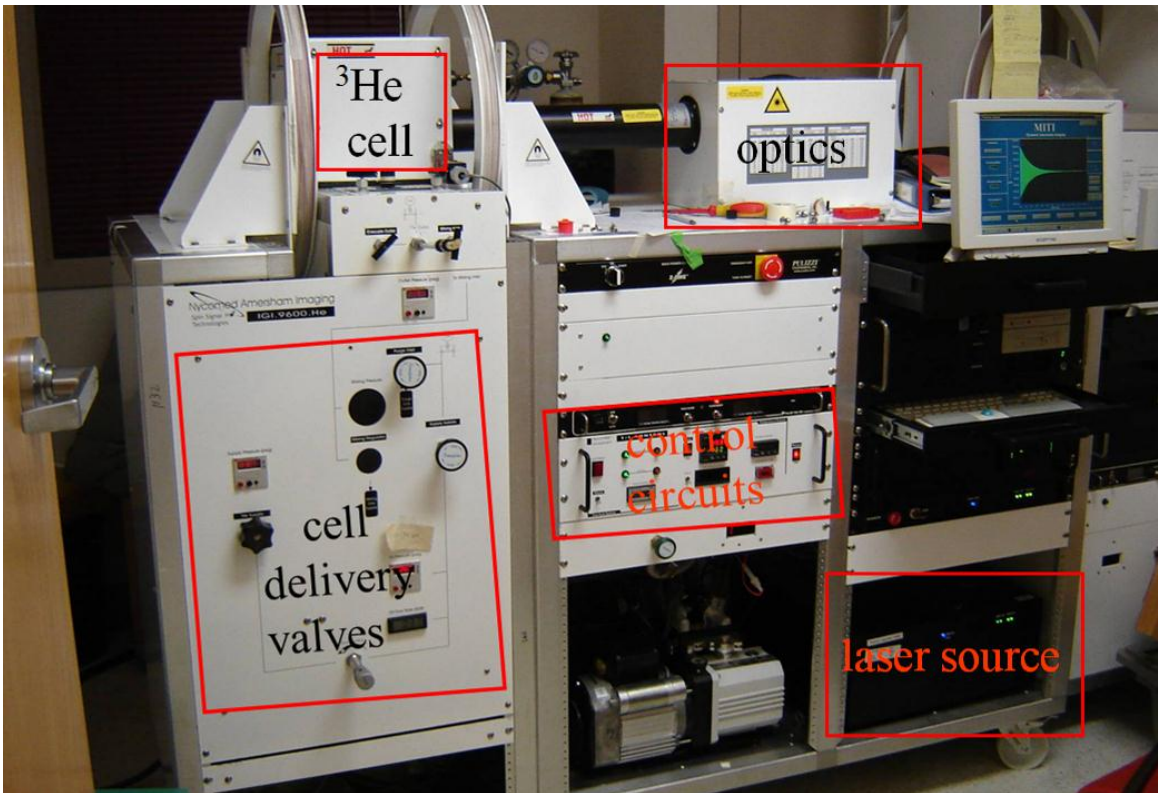


Figure 5.15: The commercial GE polarizer with its key components boxed in red. The control PC runs the laser diode array, measures the light absorption, its wavelength and can inspect the polarization level.

5.7 References

1. **Reese, T.G., O. Heid, R.M. Weisskoff, and V.J. Wedeen**, Reduction of eddy-current-induced distortion in diffusion MRI using a twice-refocused spin echo. *Magn Reson Med.* **49**(1): p. 177-82, 2003.
2. **Walker, T.G. and W. Happer**, Spin-exchange optical pumping of noble-gas nuclei. *RevModPhys* **69**: p. 629-642, 1997.
3. **Appelt, S., Ben-Amar Baranga, A., Erickson, CJ**, Theory of spin-exchange optical pumping of ^3He and ^{129}Xe . *Phys Rev A.* **58**(2): p. 1412-1439, 1998.
4. **Happer, W.**, Optical Pumping. *RevModPhys.* **44**(2): p. 169-249, 1972.

Chapter 6 - Mouse Lung MR Diffusion Experiment

6.1 MR Diffusion Experiment

Data from the MR lung diffusion experiment are obtained using bi-polar Stejskal-Tanner diffusion sequence optimized for mice (Figure 3.2) by taking 12 consecutive MR measurements, some with and some without applied gradient. Additionally, the measurement of free diffusion of the ^3He gas was conducted immediately after the lung MR scan using a 10 ml syringe and the same sequence with modified b-values. This procedure will be explained in detail in this section.

6.1.1 Bi-Polar Stejskal-Tanner Sequence for Diffusion

Measurements

Signal was collected from the whole lung by applying a broad-band RF pulse and collecting the free-induction decay data without any spatial encoding. The bipolar diffusion-sensitizing gradients were inserted between the RF excitation pulse and the data acquisition, to generate diffusion attenuation of the MR signal. The diffusion gradient waveform had the following parameters: $\tau = 0.175$ ms, $\Delta = \delta = 440$ μs and shape as shown in Figure 3.2. Parameters δ and Δ define each gradient pulse duration and the beginning of the second pulse, respectively. As the two gradient pulses are applied consecutively, Δ and δ are the same in our pulse sequence (in fact the VnmrJ would not let us use zero time between the two gradient pulses, thus we used 1 μs ; this is negligible as compared to 880 μs , duration of two

gradient pulses during which diffusion is being coded). Time τ (ramp time) is fixed in the sequence; that is, the rise/fall time of each gradient pulse is independent of the gradient strength (see Figure 3.2). The sequence controlled the gradient waveform slope to achieve this constant ramp-up and ramp-down time τ independent of b-value. The maximum b-value was varied by varying only the maximum gradient amplitude G_m . The VnmrJ sequence was programmed to calculate a required gradient for the particular b-value and selected maximum slope, making sure it never called for faster gradient ramp-rate than the hardware limitation established previously in Chapter V.

The fastest ramp time was established from the gradient calibration chart (see Figure 5.3) and our highest desired b-value, discounted by the overhead delay caused by the system controlling the ramp time. In our case, our highest b-value, $b=10$, is the limiting and determining factor for the fastest ramp time achievable by the hardware. In this case, the ramp time was calculated to be 155 μs , empirically confirmed to be 170 μs and for the final value we chose $\tau = 175 \mu\text{s}$.

The MR pulse sequence that we use in the experiment, as displayed in the Varian system software window, is shown in Figure 6.1. The first thing applied in the MR sequence is the crusher gradients, meant to dephase any potential remaining magnetization. This is followed by a square wave RF pulse at the frequency of the ^3He nuclei, for given B_0 . Half millisecond after the RF pulse, we applied a set of bi-polar gradients, first the positive one and then negative, back to back. The gradient is applied only in one axial direction (or not applied at all when $b=0$) per RF pulse, for all 12 consecutive RF pulses. The diffusion sequence has been written so that gradient pulses have always the same rise time, duration and fall time, to

accommodate the theory and mathematical model developed and described in Chapter III. Shortly after the diffusion sensitizing gradients are applied (after 270 μ s), the MRI signal is acquired for 50 ms.

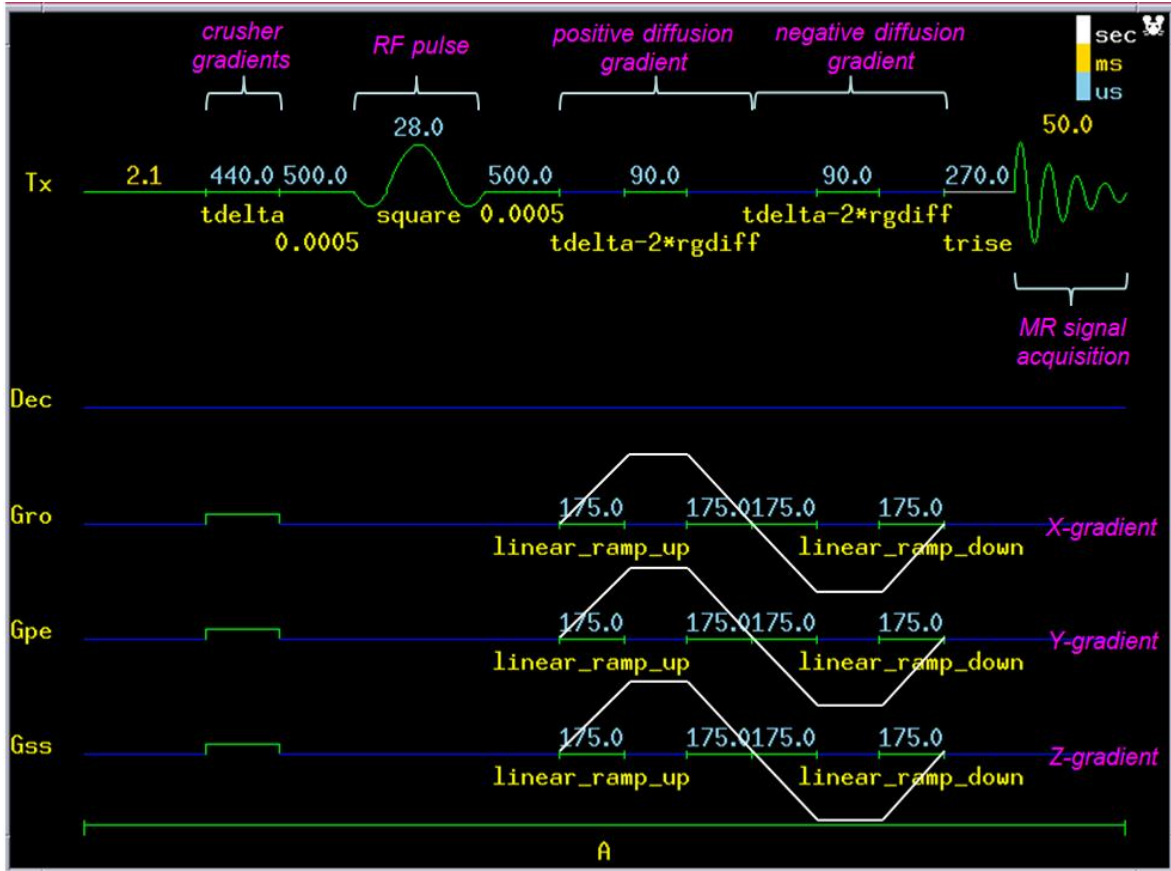


Figure 6.1: The bi-polar diffusion sensitizing gradient sequence used in all diffusion MR measurements. The sequence is run 12 times back to back for different b-values ($b[\text{s}/\text{cm}^2]=0, 10, 9, 8, 7, 6, 5, 4, 3, 2, 1, 0$). The purple italics denote main sequence parts: crusher gradients followed by the RF pulse and the bi-polar set of gradients, only in one axial direction for one 12-sequence set.

6.1.2 b-values and Diffusion Gradient Direction

The sequence is a multi-b value experiment that uses 12 b-values each with the same acquisition time of 50 ms and all other parameters as seen in the previous section. As mentioned earlier, the descending order for b-values was chosen to better use the naturally

decreasing SNR in ^3He gas experiments: apply the large b-values first while the ^3He gas has strong polarization and apply the weakest b-values last, when the polarization is reduced by a large percentage. The ten b-values were chosen for our experiments by selecting an approximate value that would provide the desired MR signal attenuation according to the Eq. (3.3) in Chapter II. Once these b-values were selected, given all sequence timings were preset, the sequence by itself chooses corresponding diffusion sensitizing gradient strength. The sequence calculated actual gradient strengths using Eq. (3.4).

Each full data set (12 MRI scans) is acquired in about a second. Each of three axial directions (X, Y and Z) is scanned individually with a new batch of hyperpolarized ^3He gas using full 12-b sequence. Although different signal strength was acquired for the each axial direction, it did not matter as the relative relationship between the 12 MR signals in each sequence is used to determine the diffusion parameters in the lungs.

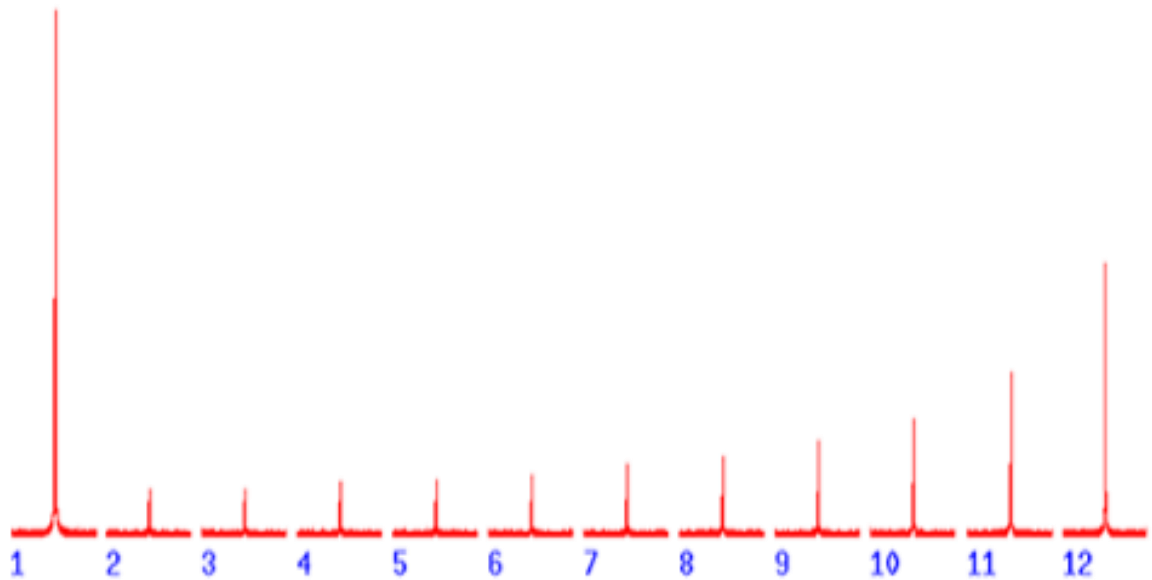


Figure 6.2: A set of typical 12 MR signals collected from the b-value descending sequence for $b[\text{s}/\text{cm}^2]=0, 10, 9, \dots, 2, 1, 0$. The first and the last pulse of $b=0$ value are used to calculate actual flip angle α .

The same 12 b-value sequence was used to measure ^3He gas self-diffusion. This is conducted right after the lung diffusion experiment. A 10 ml syringe is purged several times and filled with the pure HP ^3He gas. As compared to the lungs alveoli, the size of the syringe compartment is enormously large, needing much smaller gradient diffusion encoding. This translates into b-values for this part of experiment being vastly smaller than those used for measuring diffusion in the lungs. In this case, we calculated and experimentally confirmed that optimal gradient attenuation, required for calculating the self-diffusion coefficient, is produced by using b-values of $b[\text{s}/\text{cm}^2]=0, 1.50, 1.35, 1.20, 1.05, 0.90, 0.75, 0.60, 0.45, 0.30, 0.15, 0$. The smaller b-values as compared to measurements in lungs are required due to bigger self-diffusion coefficient. Also, large quantity of HP ^3He gas produces the strong signal, and the sequence gain had to be attenuated not to over-saturate the MR amplifier. The great SNR enabled us to calculate precise values of ^3He gas self-diffusion coefficient for later use in our lung mathematical model. Data analysis and calculations are discussed in Section 6.3, MR Data Processing.

6.1.3 Residual Magnetization

An important issue to remember whenever running MR scans consecutively, is the issue of remaining magnetization in the X-Y plane induced from the previous scan (the diffusing spins are de-phased/re-phased using bi-polar gradients, forming an echo upon which the MR signal is acquired). If there is any magnetization left from the previous MR scan, when next RF pulse is delivered, the residual magnetization will contribute to the acquired MR signal, skewing the results. Question here is reduced to the longevity of T_2^* relaxation time constant in the lungs, which is short. Literature has quoted the T_2^* in the rat lungs as short as

4 milliseconds [2], which is expectedly even shorter in mouse lungs. Various delays throughout the sequence are considerably longer than T_2^* time in mouse lungs, thus we fully expect that any magnetization that is rotated to the X-Y plane is completely dispersed/relaxed well before the next MR pulse arrives. To remove any guess work and make sure we de-phase any remaining magnetization in the X-Y plane, we included low level crusher gradients of 12 G/cm for all axial orientations (X, Y and Z) as the first step of our MR sequence, just before RF pulse (see Figure 6.1, crusher gradients).

6.1.4 Diffusion Pulse Sequence Details

In order to improve the SNR in the MR signal obtained, the order of b-values in the diffusion sequence is descending (see Section 2.5, Signal to Noise Optimization). Due to this optimization, our sequence was designed to deplete almost all of the ^3He polarization, thus providing maximum available signal, allowing for no averaging. Total length of the one full sequence, with all timings/delays, crusher gradients, RF pulses, bi-polar gradients and the acquisition time was 54.72 ms, while for 12 of them to run consecutively, it took about 1.2 seconds; the discrepancy coming from the parameter $t_r=100\ \mu\text{s}$, repetition time parameter that describes the duration of one whole sequence. One MR sequence acquires 10,000 complex data points (5,000 real and 5000 imaginary), over the acquisition time of 50 ms. The MR signal was largely attenuated after the first 10 ms, however we acquired entire 50 ms to make sure to capture any changes in case of a stronger signal. Entire set of the sequence parameters can be found in the Table 6.1.

Table 6.1: The comprehensive list of sequence parameters used for acquiring lung diffusion data, used for estimation of the lung internal physical parameters.

Parameter	Description	Values and Units
sw	spectral width (auto set with scanner/MR system preparation macro)	100 kHz
at	acquisition time (hard set by the sequence)	0.05 s
np	number of complex points acquired during the acquisition time, at	10,000
nt	number of transients (number of acquisitions, averaged together)	1
tr	repetition time – time to acquire full k-space data, one full sequence	0.1 s
te	echo time – time between RF pulse and echo peak	0.0021 s
rfcoil	RF coil type, here tuned to ^3He frequency, calibrated for flip angle, power and RF signal pattern	lungs ^3He – here named variable associated with values mentioned in description
p1	RF pulse duration	28 μs
p1pat	RF pulse pattern/shape	square
tpwr1	RF pulse power	36 dBm
ws	water suppression – here n/a	n
gcoil	gradient coil (system value, describes gradient coil present in the scanner)	205_120_HD
rgdiff	rise time of bi-polar diffusion gradient (also fall time of bi-polar diffusion gradient) – time required to transcend from zero to the required gradient value	175 μs
crushg	crusher gradient value – here fixed for all iterations	12 G/cm
dir	direction of the gradient applied – here we used all three axial directions, X, Y and Z	X, Y or Z, depending on axial diffusion being measured
tdelta	time duration from the beginning of the positive (or negative) gradient to the end of the same gradient	440 μs
tDELTA	time duration from the beginning of the bi-polar gradient to the beginning of the opposite polarity gradient – here greater than “tdelta” by 1, to accommodate internal vnmrJ system requirements	441 μs
gain	amplifier gain for acquired signal	40 dB
trise	rise time – internal variable, here used to delimit the end of the bi-polar gradient from the acquisition time	270 μs

6.2 MR Experiment for Anisotropy

6.2.1 Pulse Sequence

The theory behind the anisotropy experiment is described in Chapter III. The experiment is conducted by applying the same idea of measuring gas diffusion in the lungs, in this case three consecutive MR measurements stacked in X, Y, Z direction and compared with three MR gas diffusion measurements stacked in one direction, in our case we chose X, X, X combination. The Sequence for XYZ experiment (Figure 6.3) is ran first followed by the sequence for XXX experiment (Figure 6.4). Similar to the diffusion multi b-value sequence, the bi-polar diffusion sensitizing gradients are inserted between the RF pulse and the acquisition time, in this case three pairs of bi-polar gradients. In this sequence we used lower b-values and the Varian hardware was able to achieve somewhat faster ramp times, $\tau = 0.150$ ms, while the whole one-pole gradient time was $\Delta = \delta = 350 \mu\text{s}$. We used the same technique to control the gradient ramp time to achieve constant ramp irrespective of varied b-values in the sequence and also to prevent the sequence to ask for faster gradient ramp times than hardware's capabilities. This also ensured that the scan duration is the same each time, allowing us to compare the MR measurements side by side.

The basic premise behind the idea of confirming the anisotropy of the gas diffusion in the mouse lungs is to establish the link between the non-mono-exponential dependence of the MR signal on the b-value and the lung microstructure. This objective is embodied in our approach to compare the signal acquired with three successive gradient pairs (each gradient characterized by a given b-value) applied in the three axial directions, S_{XYZ} , and the signal acquired with the three successive gradient pairs applied in the same axial direction, S_{XXX} . If

the lungs provide isotropic environment for the gas diffusion, both signals will be the same. For anisotropic environment, e.g. cylindrically shaped airways, $S_{XYZ} < S_{XXX}$ as described previously by Eqs. (3.15) and (3.17) for any value of b . The two sequences in Figure 6.3 and Figure 6.4, are designed to show how these two signals, S_{XYZ} and S_{XXX} , have consistent deviation from each other, confirming in fact the anisotropic nature of the gas diffusion in lungs at the microscopic level.



Figure 6.3: The X, Y, Z diffusion sensitizing gradient sequence used in all anisotropy MR experiments. The sequence utilized the descending set of b-values, $b[s/cm^2]=0, 4, 3, 2, 1, 0$. The purple italics denote the main sequence parts: crusher gradients followed by the RF pulse and all three consecutive bi-polar gradients, X, Y and Z.

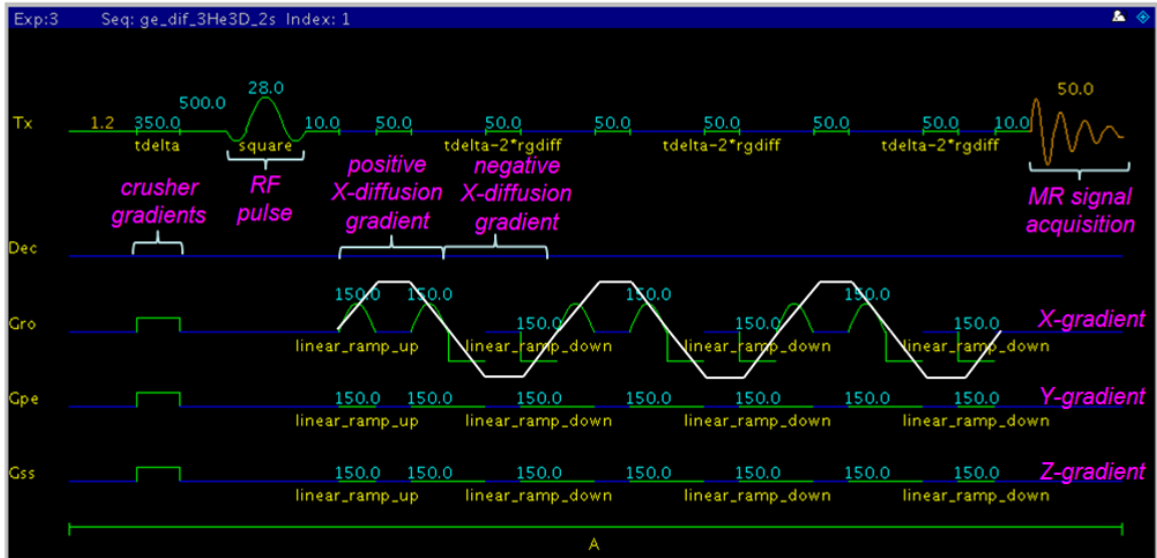


Figure 6.4: The X, X, X anisotropy sequence. The graph is for illustration purpose of the three consecutive uni-axial gradients. The sequence otherwise has the same timings and works in tandem with X, Y, Z sequence to confirm the anisotropy of the gas diffusion in mouse lungs. The purple italics denote the main sequence parts: crusher gradients followed by the RF pulse and the set of three bi-polar gradients all applied in one axial direction, X direction.

6.2.2 b-values

Similar to the original diffusion sequence, this one is also multi b-value sequence. To scan both XYZ and XXX experiment with one gas delivery to the lungs, this sequence is ran in tandem of 11 scans using descending b-values: 0, 4, 3, 2, 1, 0, 4, 3, 2, 1, 0 [s/cm^2]. The first six scans are run as XYZ sequence and the last six scans as the XXX sequence, thus the sixth scan (the mid scan) of $b=0$ is used for both sequences, XYZ and XXX, to determine the exact flip angle α . The three successive gradient pairs are reducing the signal budget left over for diffusion coding, thus we used lower b-values for this experiment, as compared to the 12 b-value diffusion experiment.

6.2.3 Anisotropy Sequence Details

This anisotropy sequence also uses crusher gradients, in this case variable crusher gradients to ensure any repetitiveness in the scanning pattern and reading undesired signals is avoided. As both measurements, XYZ and XXX are packed in one 11-RF pulses scan, this sequence uses gradient directions as variables. The overall duration of one sequence is as before, $t_r=100 \mu\text{s}$, and the 11 b-value sequence is ran in approximately 1.1 seconds. Detailed list of all anisotropy sequence parameters are in the Table 6.2.

Table 6.2: Comprehensive list of anisotropy sequence parameters used for acquiring lung diffusion data after applying successive gradients, used for establishing the link between the anisotropy of the diffusion and the lung tissue.

Parameter	Description	Values and Units
sw	spectral width (auto set with scanner/MR system preparation macro)	100 kHz
at	acquisition time (hard set by the sequence)	0.05 s
np	number of complex points acquired during the acquisition time, at	10,000
nt	number of transients (number of acquisitions, averaged together)	1
tr	repetition time – time to acquire full k-space data, one full sequence	0.1 s
te	echo time – time between RF pulse and echo peak	0.0015 s
rcoil	RF coil type, here tuned to ^3He frequency, calibrated for flip angle, power and RF signal pattern	lungs ^3He – here named variable associated with values mentioned in description, same as before
p1	RF pulse duration	28 μs
p1pat	RF pulse pattern/shape	square
tpwr1	RF pulse power	39 dBm
ws	water suppression – here n/a	n
gcoil	gradient coil (system value, describes gradient coil present in the scanner)	205_120_HD
rgdiff	rise time of bi-polar diffusion gradient (also fall time of bi-polar diffusion gradient) – time required to transcend from zero to the required gradient value	150 μs
crushg	crusher gradient value – here variable throughout the sequence	5, 15, 10, 7.5, 12.5, 5, 15, 10, 7.5, 12.5, 5 G/cm
dir1	direction of the first successive gradient applied	X, X
dir2	direction of the first successive gradient applied	Y, Y, Y, Y, Y, Y, X, X, X, X, X, X depending on anisotropic experiment being conducted

dir3	direction of the first successive gradient applied	Z, Z, Z, Z, Z, Z, X, X, X, X, X, X depending on anisotropic experiment being conducted
tdelta	time duration from the beginning of the positive (or negative) gradient to the end of the same gradient	350 μ s
tDELTA	time duration from the beginning of the bipolar gradient to the beginning of the opposite polarity gradient – here greater than “tdelta” by 1, to accommodate internal vnmrj system requirements	352 μ s
gain	amplifier gain for acquired signal	40 dB

6.3 MR Data Processing

To correct the inhomogeneity of the magnetic field produced by the MRI magnet due to imperfections in the magnet, field disturbance by the objects inside the bore, we have to shim the magnet. As each RF pulse inflicts a loss of nuclear polarization of the HP ^3He gas, it is virtually impossible to shim the magnet on the ^3He sample. Instead we shimmed the magnet using a 17 mm spherical doped water phantom that has approximately the same size as inflated mouse lungs. This shimming produces good results with the water phantom (the MR test pulse line width obtained was 20-40Hz, see Figure 6.5) and allows us to obtain good SNR with ^3He ,

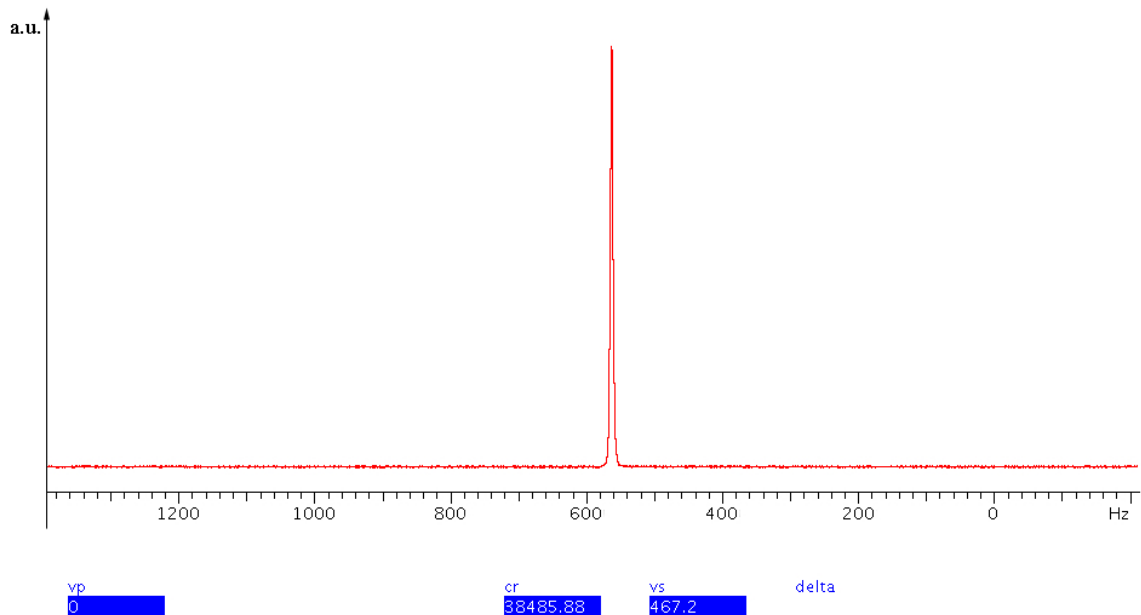


Figure 6.5: MR signal obtained by shimming on the water phantom with the volume similar to inflated mouse lungs, 17 mm in diameter. Very narrow Lorentzian signal has the width of less than 20 Hz.

however is not perfect as the material, shape and sizes differ from the mouse lungs. Thus, some field inhomogeneities will be present in the lung sample, which will broaden the MR signal, lower the SNR and introduce jumps or shoulders in the MR frequency spectrum.

Our first attempt to scan lungs was with the lungs inside of mouse chest cavity. However the body of the mouse introduced a large amount of field inhomogeneities, and the received MR signal was broad with many peaks (see Figure 6.6), with low SNR. At this point we concentrated the research on the freshly excised lungs.

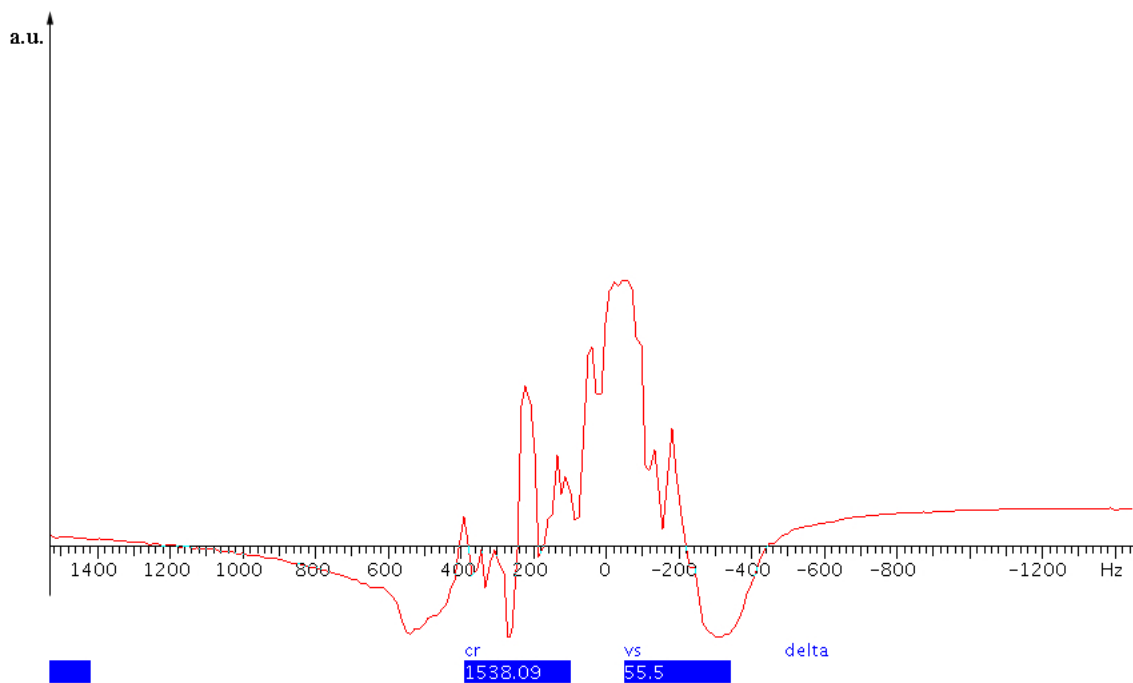


Figure 6.6: A broad MR signal with many peaks (lungs inside chest cavity make for very inhomogeneous magnetic field). The full scale is 3000 Hz wide, and shows real part of the signal. The MR signal from excised lungs, shown at the same frequency scale, 3000 Hz, was of much better shape (see Figure 6.8) and SNR.

As mentioned in the section 6.1.4 , the raw MR data are obtained as 10,000 complex data points that describe behavior of the FID during the 50 ms data acquisition time (see Figure 6.7 for an example of a single FID). The FID signal was put through the FFT (Fast Fourier Transform) in the Varian MR software system, VnmrJ, resulting in the MR frequency spectral line - see Figure 6.8. Our sequence uses a train of 12 RF pulses; a train of typical 12

MR signals can be seen in Figure 6.2. For our next step in the signal processing, we need to assess the area

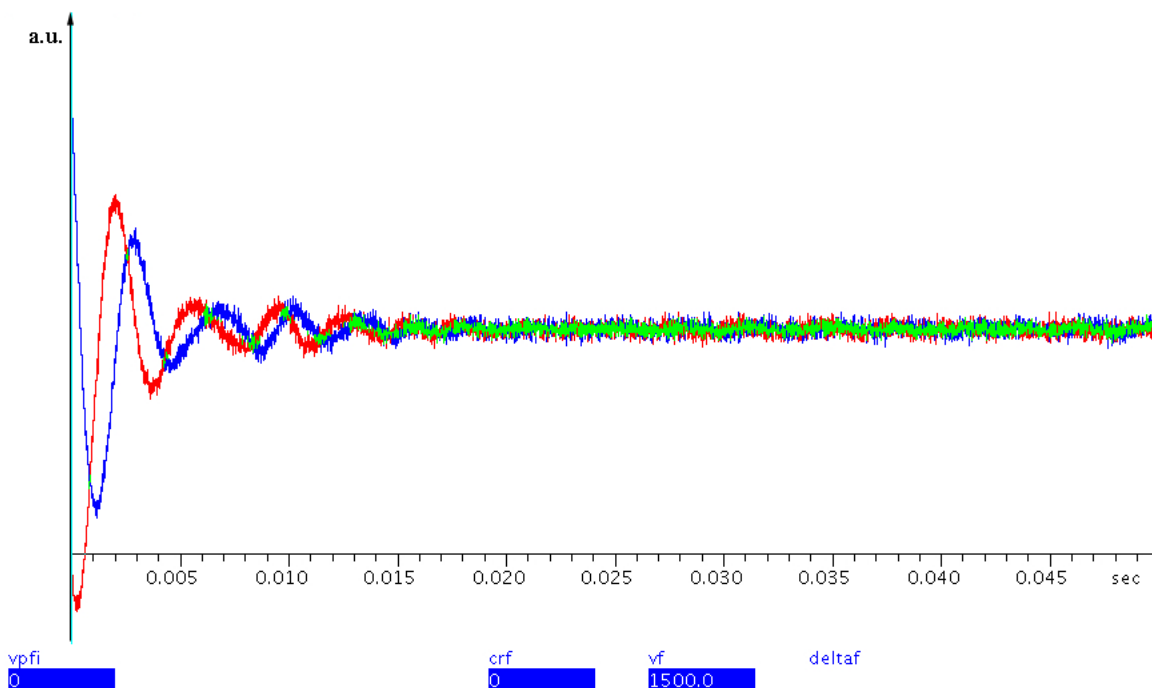


Figure 6.7: A typical FID signal collected for 50 ms, immediately after the RF excitation pulse and the Stejskal-Tanner gradients in our sequence, 5000 real and 500 imaginary data points. The red line is the real while the blue is imaginary part of the MR signal.

under the curve of each of the 12 MR spectral lines. As in Figure 6.8, the tails of the signal never fall to zero, making it impossible to calculate the area under the curve in a consistent manner, from pulse to pulse. Instead, we used Bayesian Analysis tool in the Varian system [3], to represent the original spectral information (see Figure 6.6) as the concatenation of several Bayesian curves (where obvious criterion of goodness is the residual between the original signal and the Bayes representation – see Figure 6.9). More peaks there are in the MR spectral line, the more Bayes resonances will be needed to model the original MR signal

behavior. In our experiment, we then used the Bayesian curves to calculate the height of the 12 original MR signals, by adding Bayesian peak heights together.

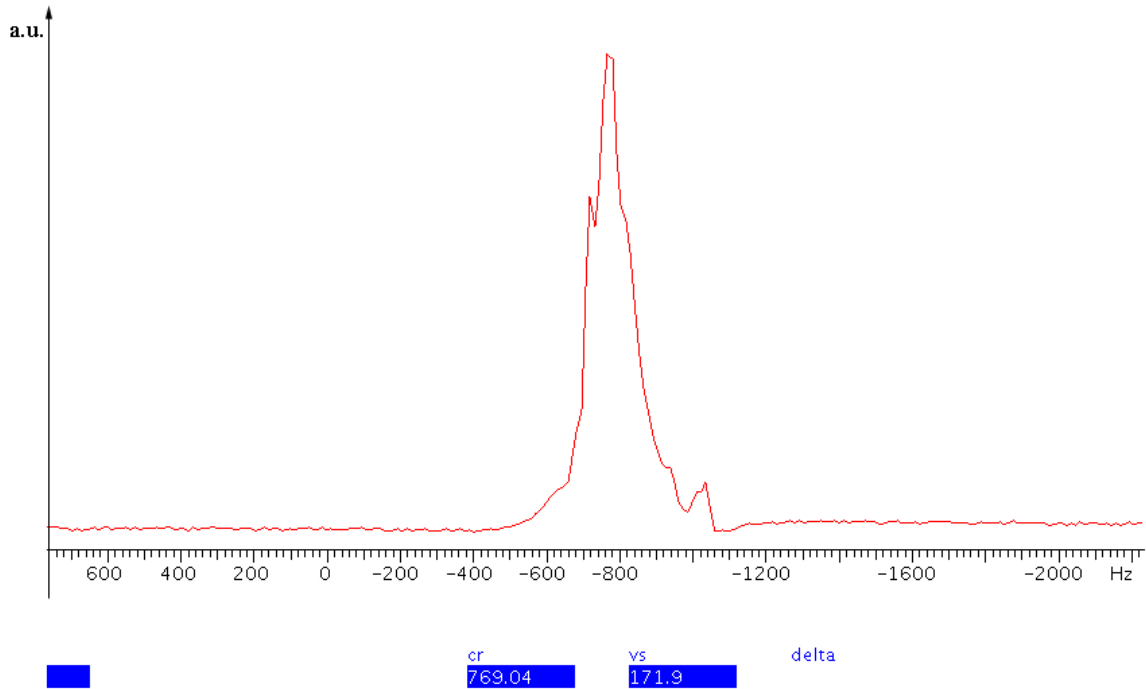


Figure 6.8: After the FID signal is passed through the FFT transform, the spectral signal is obtained. The tails of the signal never go to zero due to noise floor level, making it hard or impossible to calculate the area under the curve in a meaningful way. The horizontal axis is 3000 Hz wide, same as Figure 6.6. Signal obtained from the excised lungs is about twice as narrow with vastly improved SNR, in this case around three times. The deviation of this curve from a Lorentzian behavior seen in Figure 6.5 is due to imperfect shimming and the specific structure reflects the distribution of field inhomogeneities.

Each set of the 12 MR signals is represented using the same number of curves generated by the Bayesian Analysis: in a case of a signal represented in Figure 6.9 (the third curve) three Lorentzian peaks were sufficient to model the MR signal (the second curve) with a negligible residual (the first curve in Figure 6.9). The amplitudes of those three peaks are added together and that number is taken as the height/peak of the original MR signal. With all 12

peak heights calculated, the first ($b=0$) MR signal is normalized to 100, while the rest of 11 MR signals are normalized to the first one.

Each RF pulse inflicts a loss of nuclear polarization of the HP ^3He gas. A tradeoff in selecting the RF pulse flip angle was made between maximizing the signal extraction from each RF pulse and maintaining the polarization for subsequent signals. We chose the flip angle of 20 degrees, leaving approximately 25-30% of the polarization after the last pulse. Naturally, the precision of this quantity is dependent on the precision of the flip angle calibration. Preliminary calibration of the flip angle α was conducted using a 10 ml syringe filled with pure HP ^3He , subjected to a train of 20 RF pulses of fixed duration and strength. Final determination of the flip angle was done by comparing the first and the last values of the signal amplitude obtained with zero gradient ($b=0$) (see Figure 6.2), using equation

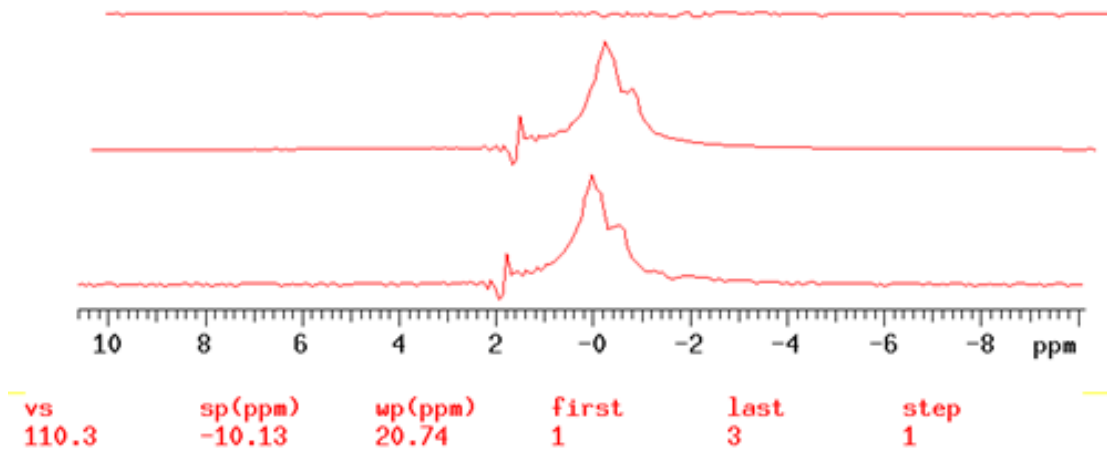


Figure 6.9: The line on the bottom represents an original MR spectrum; line in the middle is its Bayesian representation (using three Bayesian resonances), while the first line is the residual between the two signals: original MR signal and its Bayesian representation.

$S_{12} = S_1 \cdot (\cos(\alpha))^{11}$. In all experiments, the flip angle so obtained agreed closely with the value from the calibrating procedure (see Figure 6.10, dotted curve). With the true flip angle known, each measured signal amplitude is adjusted by dividing by $(\cos \alpha)^n$, where n indicates the number of previous RF pulses. The adjusted data are then plotted as a function of b -value and normalized to 100. The adjusted data are analyzed using Eqs. (3.6), (3.7) and (3.8) (as described in the Chapter III) to obtain the key lung microstructure parameters, R and b . The data are analyzed using OriginPro 7.5 (OriginLab; Northampton, Massachusetts).

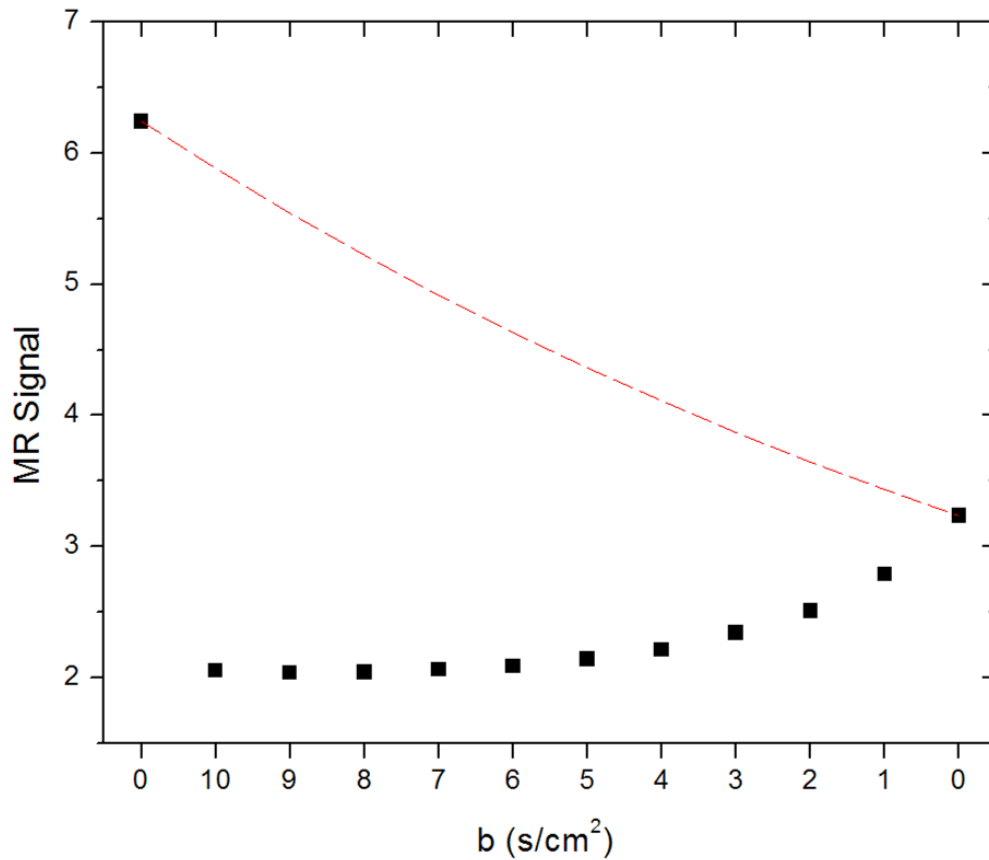


Figure 6.10: Original MR signal (arbitrary units) amplitude, using the order of b -values as they were collected in the experiment, in $[s/cm^2]$. Two $b=0$ signals, at the beginning and the end of the sequence, have different amplitudes as polarization is consumed by RF pulses during the measurement. These two signals are used to determine the RF pulse flip angle for later correction of the amplitudes. Dotted line shows the signal decay path that would occur in case of no gradients, all $b=0$.

Signal after such an adjustment accounting for RF consumption, is shown in Figure 6.11.

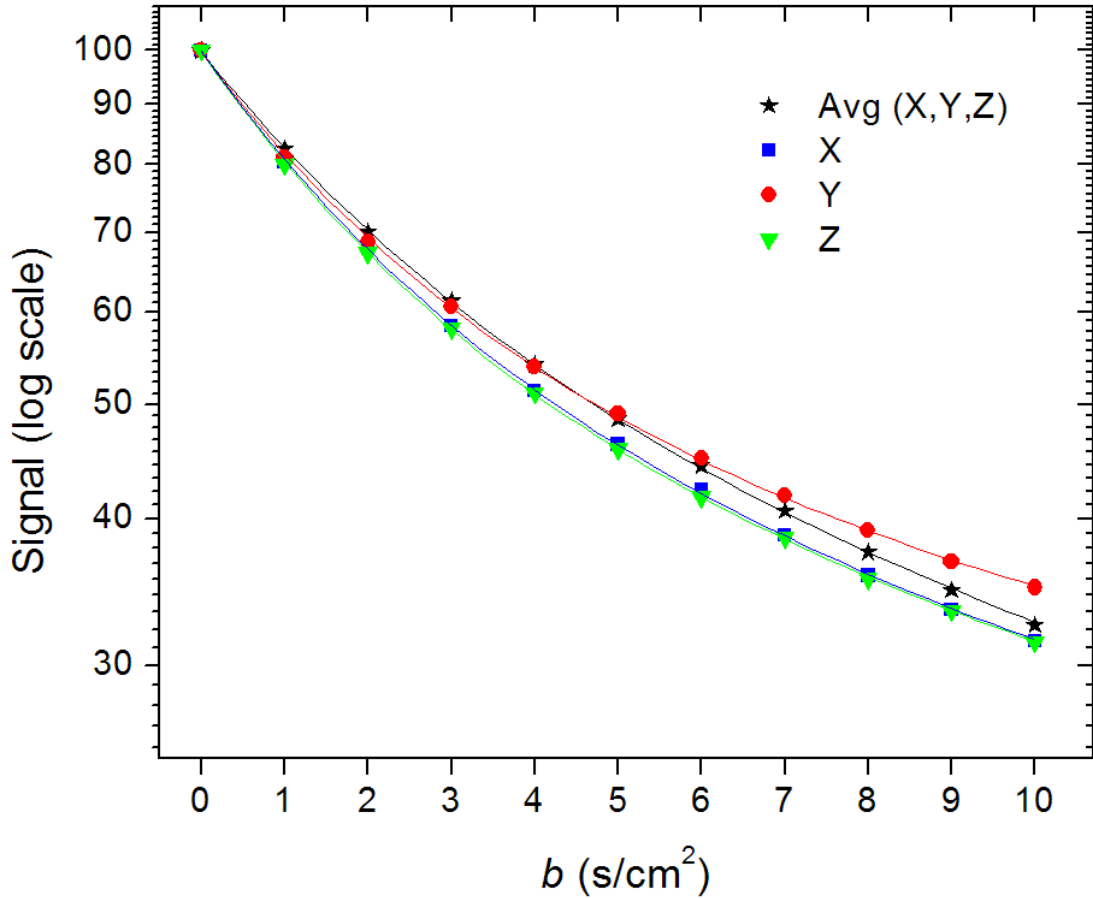


Figure 6.11: Typical dependence of adjusted MR signal amplitude (logarithmic scale) on b-value (symbols) and the fitting curves (solid lines) for X, Y, Z and their average. Results demonstrate an excellent fit with $\chi^2=0.045$. A very important feature is the substantial deviation from mono-exponential behavior (deviation from straight line), in agreement with theoretical prediction, in [1] and the theory presented in this paper.

The theoretical equations connecting the MR measurements to the lung geometrical parameters (Eqs. (3.7), (3.8) in Chapter III) rely on knowledge of the ³He gas free diffusion coefficient D_0 (recall that in our experiments the lungs are filled with pure ³He gas). To measure D_0 , approximately 10 ml of HP ³He gas from the same batch of gas is scanned in a

syringe using the same 12 b-value sequence with a substantially lower range of b-values, $b[\text{s}/\text{cm}^2] = 0, 1.5, 1.35, 1.2, \dots, 0.3, 0.15, 0$.

The result of this measurement was $D_0 = 1.76 \text{ cm}^2/\text{s}$, which is in good agreement with similar values found in the literature ($1.8 \pm 0.2 \text{ cm}^2/\text{s}$) [4, 5] for 20°C , the temperature maintained for all our experiments.

Thus, the flow of the steps going from the MR experiment to the final 12 MR signals where the lung physical parameters are extracted is given in the Figure 6.12.

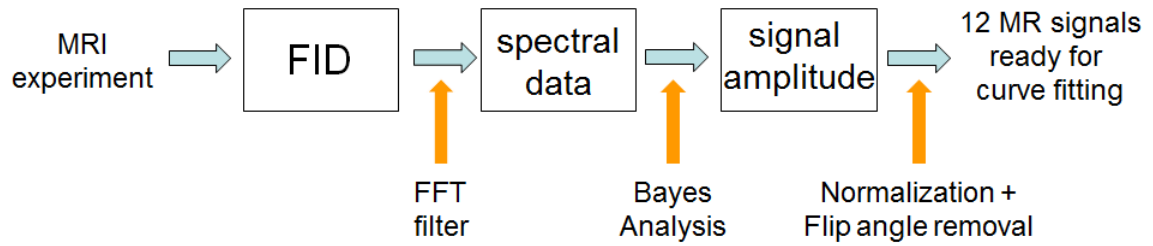


Figure 6.12: The figure gives a complete data processing path spanning the MR experiment until the data are ready for the curve fitting and lung physical parameters extraction.

6.4 References

1. **Yablonskiy, D.A., A.L. Sukstanskii, J.C. Leawoods, D.S. Gierada, G.L. Bretthorst, S.S. Lefrak, J.D. Cooper, and M.S. Conradi**, Quantitative in vivo assessment of lung microstructure at the alveolar level with hyperpolarized ^3He diffusion MRI. *Proc Natl Acad Sci U S A.* **99**(5): p. 3111-6, 2002.
2. **Ailion DC, C.T., Blatter D, Morris A, Cutillo A, Durney D, Johnson S**, Applications of NMR spin imaging to the study of lungs. *Bull. Magn Resonance.* **6**: p. 130-139, 1984.
3. **Bretthorst, G.L.**, *Bayesian Spectrum Analysis and Parameter Estimation*. Lecture Notes in Statistics, ed. J. Berger, et al. Vol. 48. 1988, New York: Springer-Verlag. 209.
4. **Agulles-Pedros, L., R.H. Acosta, P. Blumler, and H.W. Spiess**, Resolution enhancement in MRI of laser polarized ^3He by control of diffusion. *J Magn Reson.* **197**(1): p. 56-62, 2009.
5. **Schreiber, W.G., A.E. Morbach, T. Stavngaard, K.K. Gast, A. Herweling, L.V. Sogaard, M. Windirsch, J. Schmiedeskamp, C.P. Heussel, and H.U. Kauczor**, Assessment of lung microstructure with magnetic resonance imaging of hyperpolarized Helium-3. *Respir Physiol Neurobiol.* **148**(1-2): p. 23-42, 2005.

Chapter 7 - Summary of Results

7.1 MR Measurements of Key Lung Parameters

An example of the raw data set corresponding to the MR signal amplitude acquired with the 12 b-values sequence is shown in Figure 6.10. A typical dependence of the corrected amplitudes on the b-value is shown in Figure 6.11 (symbols) along with the fitting curve (solid line). Data are presented for three directions of applied diffusion sensitizing gradients and demonstrate a small anisotropy. This is consistent with the results of Mitzner et al [1] who demonstrated in mice that lung structure is slightly anisotropic even at the macroscopic level. These authors provided evidence that the measured mean linear intercept L_m is dependent on the planar orientation of the sample. Specifically, L_m along the ventral-dorsal axis of the lung tissue was on average 7.4% greater than L_m measured in the perpendicular direction. Our approach takes into account the anisotropic structure of the lung acinar airways at the microscopic level; however it assumes isotropy of airway orientations at the macroscopic level. That is, the airways are oriented in all directions essentially equally. In principle, we could introduce this anisotropy at the macroscopic level in our equations, which would further increase the model complexity. Instead, to avoid potential bias based on this effect and retain the model's isotropy at the macroscopic level, we collected data for three spatially orthogonal directions of diffusion sensitizing gradients and averaged the MR signals together before data analysis. The result shown in Figure 6.11 demonstrates an excellent fit with $\chi^2=0.045$. For this individual measurement, lung microstructure parameters are $R=103.7\pm 2.9 \mu\text{m}$ and $h=63.1\pm 1.1 \mu\text{m}$. An important feature of this signal dependence on b-value is the substantial deviation from the mono-exponential behavior (deviation from

a straight line on the logarithmic scale in Figure 6.11), in agreement with theoretical prediction and experimental data obtained in human lungs [2].

The complete set of morphometric data for all six mice are summarized in Table 7.1. Our average measurement of the mean linear intercept Lm (from Eqs. (3.9) and (3.10)) presented in Table 7.1 for six mice is $\sim 62 \mu\text{m}$. This corresponds to a surface-to-volume ratio of the air spaces of 670 cm^{-1} . We also found that an average alveolar density, N_a is about 3200 per mm^3 . The corresponding number that we found previously [3] in normal human lungs (S/V about $200\text{-}240 \text{ cm}^2/\text{ml}$ and N_a about $120\text{-}150$ per mm^3) were in good agreement with direct histological measurements.

Table 7.1: Summary of geometrical and diffusion parameters from excised lungs of six mice. The table gives values of key parameters in our model: major airway radius R , the depth of alveolar sleeve h , alveolar surface-to-volume ratio S/V , mean chord length Lm and alveolar density N_a , where the error bars are the fit uncertainties. Average diffusion along and perpendicular to the airways is $0.7 \text{ cm}^2/\text{s}$ and $0.0143 \text{ cm}^2/\text{s}$, respectively. Both diffusion parameters, D_L and D_T are sharply reduced from ^3He free diffusion ($D_0=1.76 \text{ cm}^2/\text{s}$) as the alveolar ducts and walls present obstacles to diffusing ^3He atoms. Quantity β_L is kurtosis factor for longitudinal diffusivity.

mouse #	$R, \mu\text{m}$	$h, \mu\text{m}$	$S_a/V_a, \text{cm}^{-1}$	$Lm, \mu\text{m}$	N_a, mm^{-3}	$D_{L0}, \text{cm}^2/\text{s}$	$D_{T0}, \text{cm}^2/\text{s}$	β_L
1	103.7 ± 3	63.1 ± 1	738	54.2	2984	0.741	0.0114	0.0174
2	107.8 ± 11	48.3 ± 5	555	72.1	2656	0.877	0.0144	0.0081
3	84.1 ± 5	46.3 ± 2	836	47.8	5594	0.642	0.0063	0.0117
4	119.1 ± 3	64.1 ± 1	580	69.0	1969	0.679	0.0235	0.0181
5	109.3 ± 4	46.9 ± 1	524	76.4	2548	0.796	0.0170	0.0075
6	97.1 ± 10	58.8 ± 2	788	50.8	3634	0.486	0.0133	0.0216
mean	103.5	54.6	670	61.7	3231	0.704	0.0143	0.0141
std dev	11.9	8.3	133	12.2	1280	0.135	0.0058	0.0058

For comparison with the data reported in Table 7.1 we have compiled in Table 7.2 various results from the literature obtained by stereological analysis of mouse lungs [1, 4-11]. The

studies assessed alveolar number, mean linear intercept of air spaces, and the surface-to-volume-ratio, as well as mean alveolar volume $v(alv)$; this latter value allowed obtaining an approximate estimate of $h = v(alv)^{1/3}$ assuming a cubic shape of alveoli in first approximation. The data show considerable variation, which may reflect significant differences between animals; but some of this may be due to different inflation levels achieved in fixation as the measured lung volumes varied by a factor of 3. Results obtained in this study for L_m , S/V and N_a are within the range of published data (Table 7.2). Some of the differences may also be related to the fact that the lungs prepared for microscopic morphometry are generally fixed by fluid instillation at 20 cm H₂O whereas in the present study the helium gas was applied at a pressure of 30 cm H₂O resulting in a larger volume. The lower pressure and the fluid-filled state may have affected some of the microscopic measurements.

Table 7.2: Morphometric data from microscopic studies from various literature sources obtained by stereological analysis of mouse lungs using animals of different strain, age and size. The measured lung volumes varied by a factor of 3, some of which may be due to different inflation levels achieved in fixation.

Source	Strain	age (week)	M _b g	V _L cm ³	L _m μm	N _V (a) mm ⁻³	h μm	v(a) 10 ³ μm ³	S _a /V _a cm ⁻¹
Voswinkel	C57BL/6	12-16	24.3	0.721	54.3		37**	51	740
Knudsen [6]	C57BL/6	12		0.680	35	14.1	39**	59	1150
Soutière	C57BL/6J	6-8		0.95-1.45	45-63				
Fehrenbach	C57BL/6	12-14		0.432		2.7			
Mitzner	C57BL/6	10-12		1.2	52				770
Knust	C57BL/6	6.5-10	20.6	0.307	85	9.6	39**	59	470
Lee	C57BL/6J	7-9			38				
Kang	C57BL/6J	12		1.7	55				
Knudsen	C57BL/6*	12		0.69	39				915
Overall range		6-16	20-25	0.4-1.5	40-80	3-14	30-50		500-1000
This study	C57BL/6	12-16	21-27	~1.2	61.7±12	3.2±1.3	55±8		670±133

*) SPD-deficient mice treated with recombinant SPD; **) $h = v(alv)^{1/3}$

The published data [1, 4-11] do not contain estimates of the morphometric parameters of alveolar ducts, such as their major radius R that comprises both the inner duct radius r and the alveolar sleeve of depth b (Figure 3.1). Such data characterizing the structure of acini have been obtained for human, rat and rabbit lungs [12, 13].

Here for illustration purposes we present data obtained in an as yet unpublished identical study by Weibel E.R. of the acinus of the mouse lung that provided a limited number of specimens on which the size characteristics of mouse alveolar ducts could be estimated. These studies were based on two types of preparations: silicone rubber casts filled to about 70% TLC [13], and perfusion fixed lungs air-inflated at about 60% TLC [14]; examples of these preparations are shown in Figure 7.1A and Figure 7.1B. The specimens were obtained on BALB/6 mice of about 40 gr and a total lung volume of 0.8-1.0 ml following the methods described in [13]. The two specimens are different in terms of preparation artifacts: the silicon rubber cast does not shrink during preparation and thus shows the real size of the structures; in contrast, the lungs fixed by vascular perfusion suffered considerable shrinkage during the preparation procedures, mainly because of critical point drying. We estimate that measurements obtained on the perfusion fixed specimen must be corrected by a factor of 1.6; this about the difference in the size of alveoli in Figure 7.1A and Figure 7.1B. The very small size of mouse acini (mean volume $\sim 0.1 \text{ mm}^3$) rendered a rigorous morphometric analysis of the duct structure, as done for larger lungs [12, 13], difficult, but it was possible to determine an approximate range for the parameters R , r , and b , as marked on a few examples in Figure 7.1. We find that the inner duct radius r , marked by double-pointed arrows, measures on the order of 40-75 μm and shows systematic variation being nearly 2 times as

wide in the ducts of the first generations following on the transitional bronchiole (trb) as compared to more peripheral ducts; this agrees with the pattern found in rat, rabbit and human lungs [12, 13]. The outer radius R , marked by a bar, varies in the same sense but to a lesser degree with a

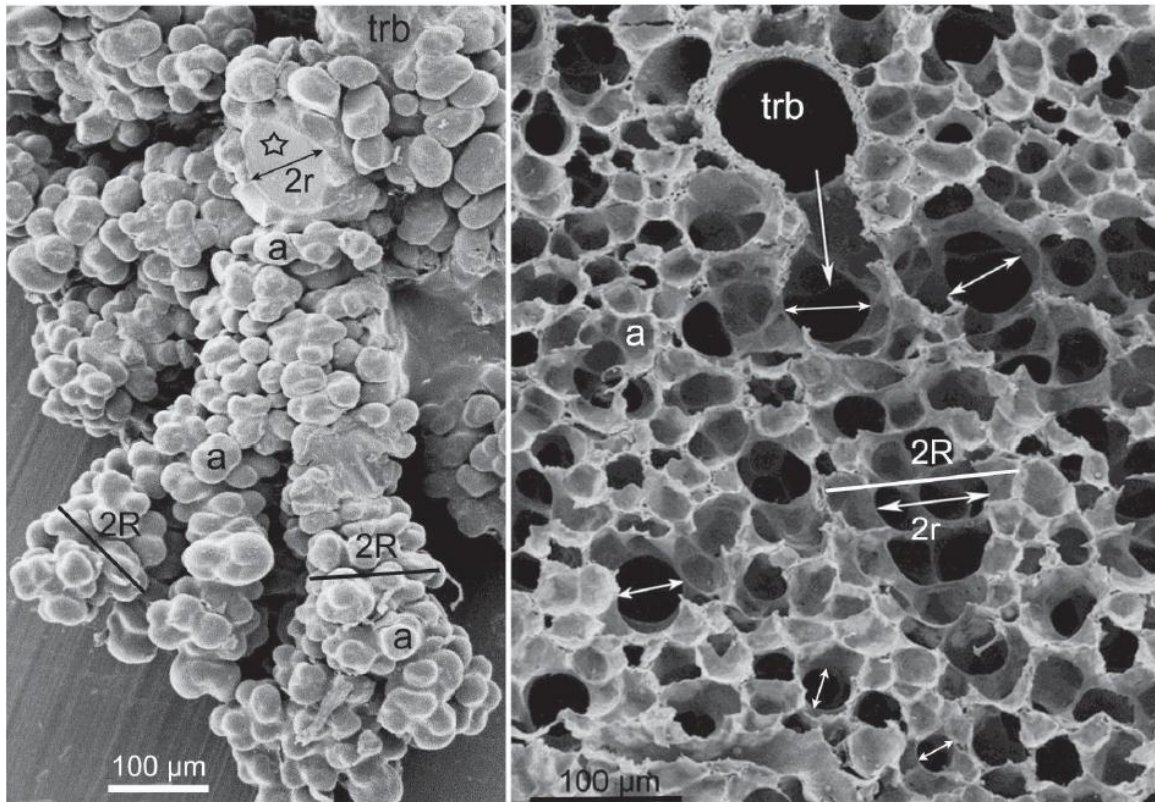


Figure 7.1: (A, left) Scanning electron micrograph of segment of a partly dissected silicone-rubber cast of an acinus of a mouse lung showing the transitional bronchiole (trb) as entrance airway and alveoli (a) grouped around alveolar ducts which have been partly separated. Asterisk marks a transected alveolar duct with diameter $2r$. Bars mark approximate outer diameter $2R$. (B, right) Scanning electron micrograph of a perfusion-fixed mouse lung air-inflated to about 60% TLC showing a transitional bronchiole (trb) that opens into the acinus (arrow). Double-pointed arrows mark the inner diameter $2r$ of alveolar ducts that are wide in the first generations of branching and taper somewhat towards the periphery; the bar marks the outer diameter $2R$ that comprises the sleeve of alveoli (a). Range of measured values: $R = 70\text{-}100\ \mu\text{m}$, $r = 40\text{-}75\ \mu\text{m}$, $b = 30\text{-}55\ \mu\text{m}$.

range of 70-100 μm . The size of alveoli (a) varies considerably in the range of 30-55 μm .

These results show a reasonable agreement with our MRI measurements.

Certain phenomena, not taken into consideration by our model and experimental method, can affect the accuracy of the results obtained with ^3He gas lung morphometry technique. First we mention that our model assumes that during the diffusion experiment of duration $2\tau=880\ \mu\text{s}$, most ^3He atoms spend their time diffusing in a single airway. The effect of ^3He atoms moving into another airway of different orientation during the diffusion measurement is especially important in small animals. Because the average mouse lung mean alveolar length is much smaller than in humans, in this study we used very short bipolar diffusion-sensitizing gradient pulses ($\delta\tau=440\ \mu\text{s}$), as compared to $1800\ \mu\text{s}$ in human experiments [3]. This decreases the fraction of ^3He molecules escaping into adjoining airways and distorting the lung morphometry measurements. In principle, this effect could be further reduced by using still smaller diffusion times, however hardware limitations in our case would not allow for further improvement.

To minimize the undesirable contribution of ^3He gas in conducting airways to our measurements, we followed the ^3He gas delivery with 15% of inert N_2 . Practically, this may lead to partial mixing of ^3He and N_2 gases resulting in a reduced ^3He diffusion coefficient D_0 in some regions. If we assume the dilution level of ^3He to be 90%, the corresponding reduction in D_0 will be from $1.76\ \text{cm}^2/\text{s}$ for 100% ^3He concentration to $\sim 1.58\ \text{cm}^2/\text{s}$. Substituting this reduced D_0 in the equations used for data analysis yielded average changes of geometrical parameters R and b of only 3.6% and -4.3%, respectively. Thus we expect that ^3He - N_2 gas mixing between large and small airways causes errors no more than 5% in estimation of the geometrical parameters R and b .

Our model is limited to the adopted lung microstructure and its simplified representation. The data analysis provides an overall average of the distribution of the airway and alveolar sizes throughout the lungs. The main geometric parameters characterizing acinar airways are the internal acinar airway radius r and the outer radius R (which includes the sleeve of alveoli with its depth, b) [12]. Both of these parameters (R and r , thus R and b) vary depending on the position and branching level of the acinar airway tree. Our method assumes that we can characterize the diffusion attenuated MR signal in terms of the average characteristics across the acinus and, further, across the lung. In humans this is justified by experimental measurements of Haefeli-Bleuer and Weibel who found that the variation in parameters distribution is rather small: the distribution width is 16% for R and 20% for r [12]. In this manuscript we also make an assumption of the “narrowness” of the distributions of parameters R and r and characterize our result by average parameters R , r and b in mice.

In this work we studied only lungs obtained from healthy mice. The theoretical model developed here is suitable for deformation/destruction of lung microstructure only in the initial stages of emphysema that can be characterized by airways inflation and retraction of alveolar sleeve [3, 15]. At advanced stages of emphysema, characterized by severe destruction of lung parenchyma, our measurements could return skewed values of the key lung parameters. However, validation data obtained in human lungs [3] demonstrated that the measurements of L_m using ^3He gas ADC even in severely emphysematous lungs were in excellent agreement with direct histological measurements.

7.2 MR Measurements of Lung Anisotropy

For the lung anisotropy experiment, the diffusion data are acquired using the same sequence with different gradient spatial orientations (see Figure 6.3 and Figure 6.4), one with three consecutive gradients in the same direction, XXX, and another with gradients in the orthogonal directions, XYZ. As described in the Section 3.1.4, “Diffusion Anisotropy in the Lung Model”, it can be shown mathematically that, if lungs are made out of cylindrical airways (as opposed from spherical ones), for any b-value the MR signal from the two experiments will be consistently different, e.g. theory predicts $S_{XYZ} < S_{XXX}$.

A typical raw data set obtain from these experiments is shown in Figure 7.2. Our approach for this experiment is to unequivocally link the anisotropy of the diffusion in the lungs with the lung microstructure. Raw MR data obtained as in Figure 7.2 are analyzed using the same Bayesian analysis technique, where flip angles are removed. Typical MR dependence on b-value for both, XYZ- and XXX-experiments (log scale), obtained for one mouse is shown in Figure 7.3. Clearly, the signal corresponding to XYZ experiment consistently lays below the signal corresponding to the XXX experiment. This consistent difference between the two signals, S_{xyz} and S_{xxx} (Figure 7.3) proves that non-mono exponential behavior of the MR signal is indeed due to the diffusion anisotropy at the microscopic level. Furthermore, as experiment is set up to confirm the anisotropy due to cylindrical lung airways and data support the theoretical expectations, in this experiment we established a link between the anisotropy of the gas diffusion in the lung and the lung microstructure.

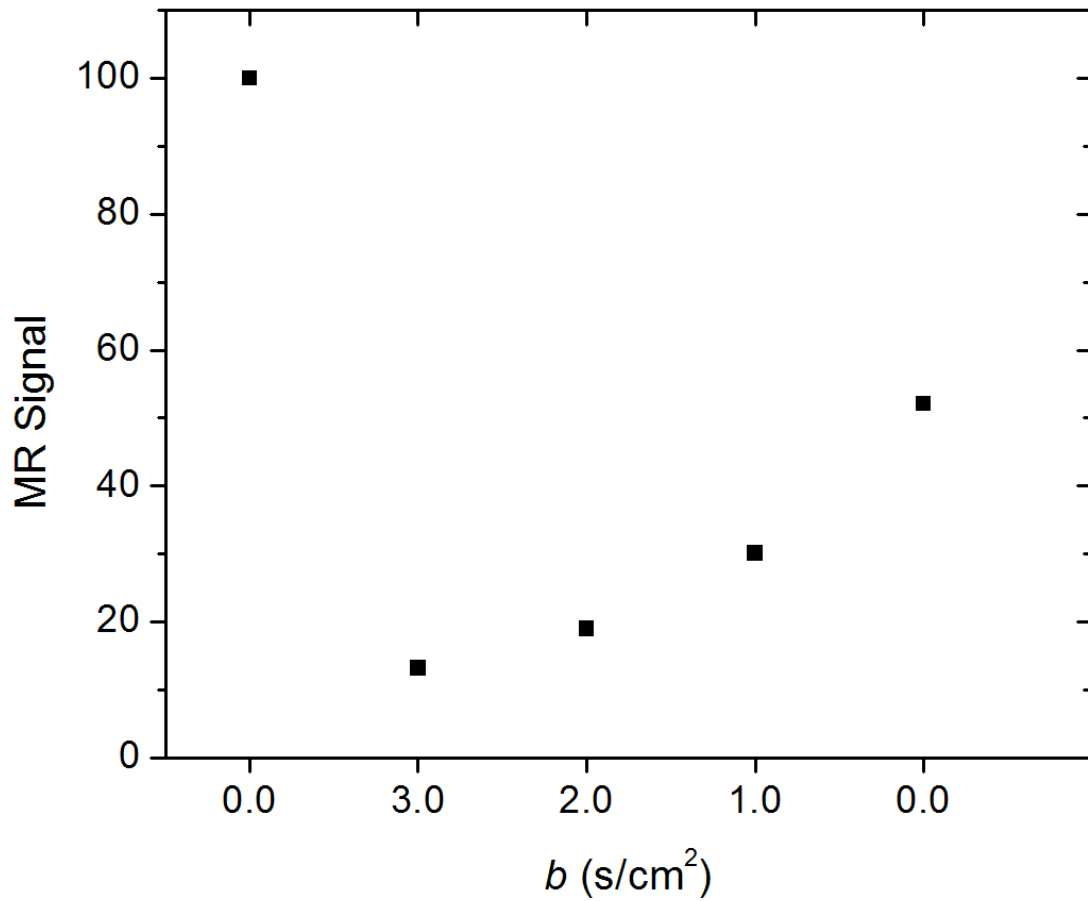


Figure 7.2: Raw data are shown in the order they were acquired. After the first $b=0$ acquisition, the descending order of b -values was chosen to better use the naturally decreasing SNR in ^3He gas experiments: apply the large b -values first while the ^3He gas has strong polarization and apply the weakest b -values last.

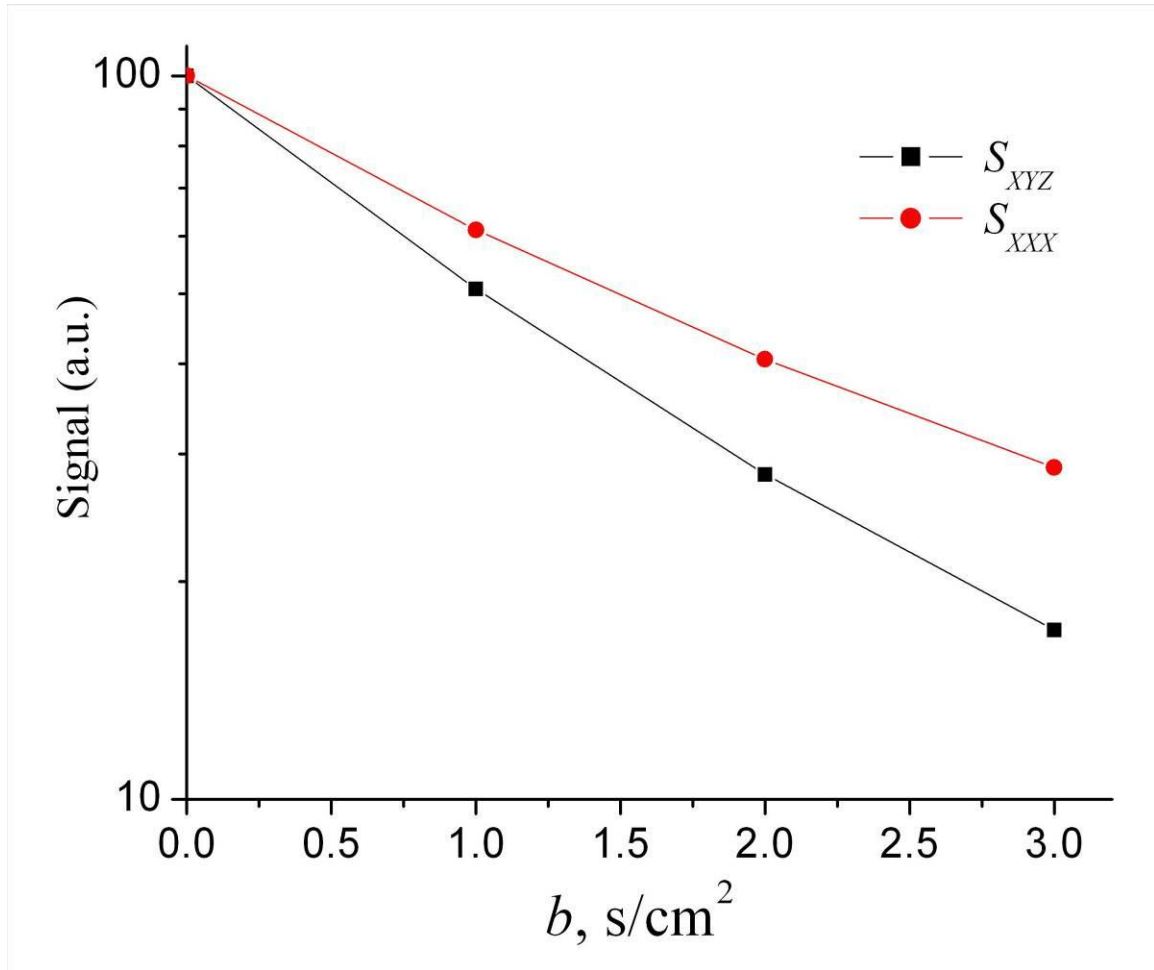


Figure 7.3: Typical XYZ and XXX data comparison for one mouse lungs. The S_{xxx} stays above S_{xyz} throughout the range of different b -values used in the experiment. This consistent inconsistency indeed demonstrates the ^3He gas diffusion anisotropy at the microscopic level in the mouse lungs.

Data in Figure 7.2 and Figure 7.3 are presented for one mouse. The data for all other mice from Table 7.1, where we measured the lung microstructure parameters, produced consistent difference between S_{xxx} and S_{xyz} , as shown in Figure 7.3. All six graphs are shown in Figure 7.4. The MR signal obtained from S_{xyz} experiment is expected to be anisotropic and it clearly demonstrates deviation from the monoexponential behavior (deviation from a straight line in the logarithmic scale), while MR signal from S_{xxx} experiment is much closer to the straight line, as also expected.

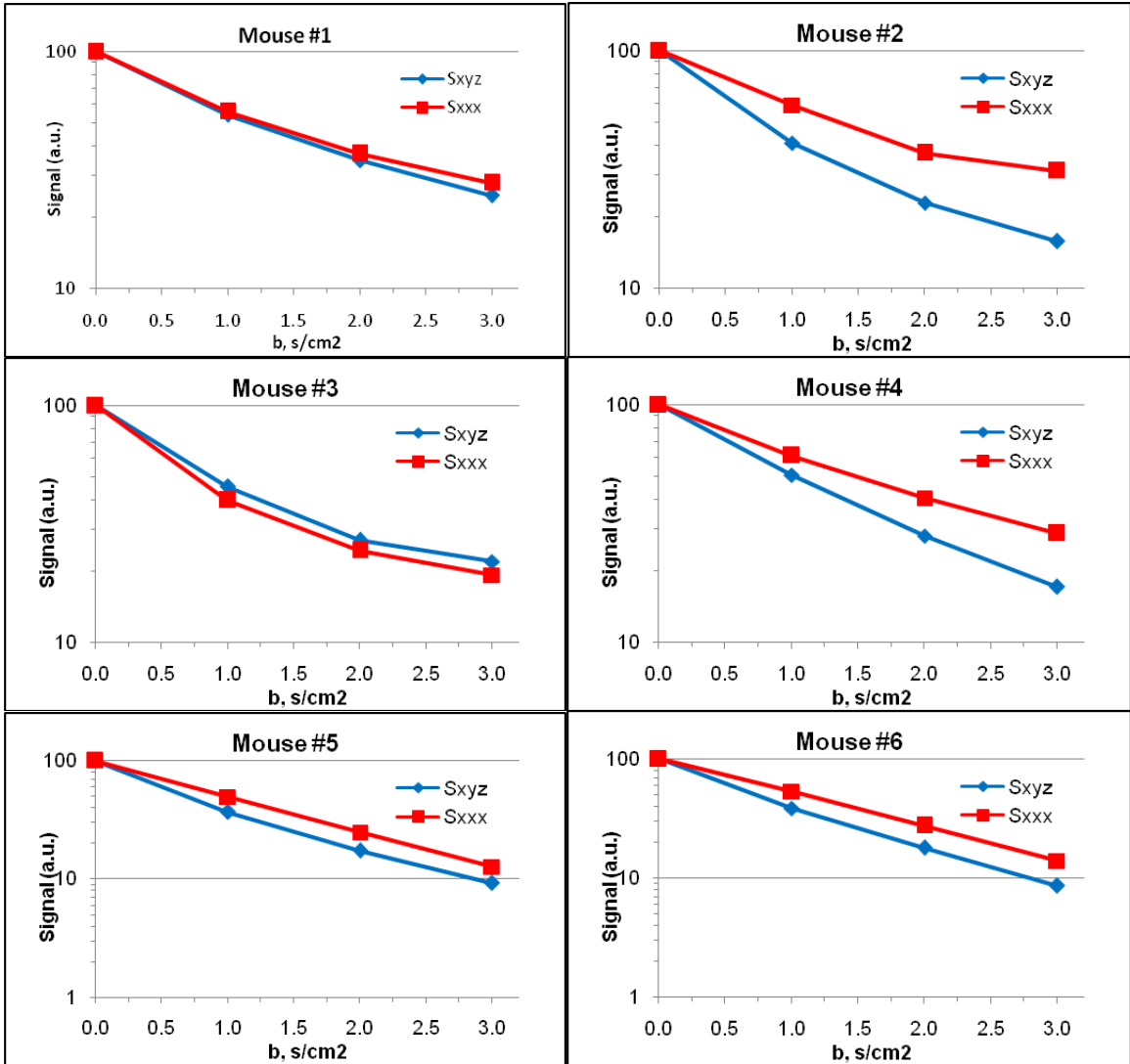


Figure 7.4: Summary of comparison of S_{xxx} and S_{xyz} signals for all six mice, as in Table 7.1, for the anisotropy experiment. MR signal S_{xxx} is consistently higher than S_{xyz} for all scanned b -values, demonstrating the gas diffusion anisotropy in the mouse lungs, due to the cylindrical shape of airways in the mouse lungs.

7.3 Results from *in vivo* Studies

An *in vivo* study on seven mice was conducted by one of the PhD candidate in our labs, Wei Wang, with similar objectives: implement ^3He gas lung morphometry to quantify regional

lung microstructure in the mouse *in vivo* [16] using the same mathematical modeling as described in the Section 3.1 of Chapter III.

Briefly on methods: Mice were of the same strain and age group as in our original study. Animal was anesthetized using standard procedure, orally intubated using 20-gauge intravenous catheter and attached supine to a ventilator [17], custom built in our labs. The animal was ventilated at 120 breaths per minute with each breathing cycle consisted of an inhalation of $^3\text{He}/^4\text{He}$ gas mixture, a short breath hold, further inhalation of pure oxygen, followed by a passive exhalation. A trigger signal from the ventilator during the short breath hold ensured that the image data acquisition began at the same point, where lungs are still. Using 2D multi-slice gradient echo sequence with embedded bipolar diffusion-sensitizing gradients (with similar key sequence parameters as our diffusion experiment: 6 b-values of 0, 1, 2, 4, 6, 9 s/cm^2 , $\delta=\Delta=440 \mu\text{s}$, rise time $\tau = 150 \mu\text{s}$) ^3He gas diffusion data were collected. For each mouse, five 2 mm-thick axial slices were acquired with a 40 mm x 40 mm field of view, covering nearly entire lung.

A voxel by voxel ^3He gas diffusion data was extracted, generating parametric maps for alveolar depth h , airway radii R and the mean linear intercept, L_m . Figure 7.5a shows the representative parameter map for one mouse, while the corresponding ^1H MR images and ^3He ventilation images are shown in Figure 7.5b and Figure 7.5c.

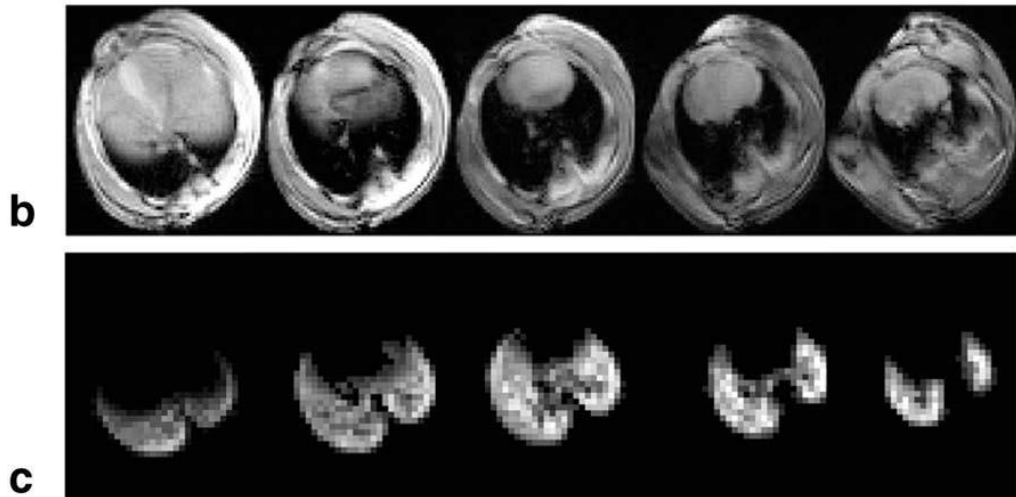
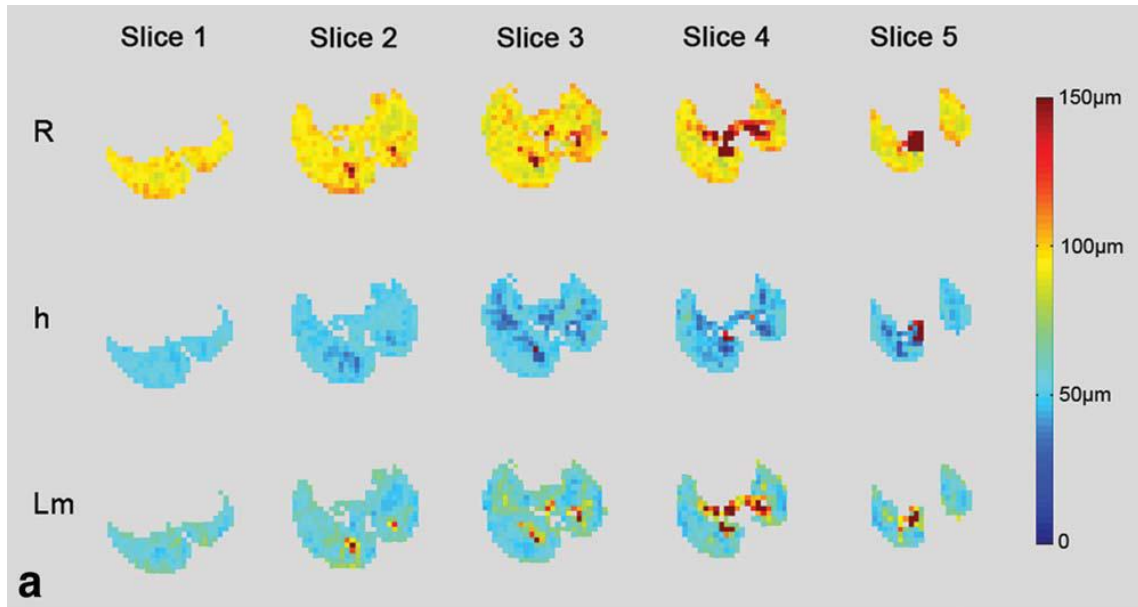


Figure 7.5: **a:** Representative geometric parameter (R , h , and Lm) maps obtained from one healthy mouse lung. Major airways are red in the maps of R . The pixel size is $0.63 \text{ mm} \times 0.63 \text{ mm}$ and slice thickness is 2 mm . The slightly elevated R and Lm values in the ventral and dorsal lung periphery are fairly consistent from mouse to mouse.
b: corresponding ^1H images showing anatomical positions.
c: Corresponding HP ^3He ventilation images ($b=0$)

Table 7.3 summarizes all the parameters for all mice: key physical parameters as R , h , Lm , Na and S/V are all fairly homogeneous throughout the entire lung, with some regional variation

and slight increase of R and Lm in the lung periphery. Variation from slice to slice for average values is minimal.

Table 7.3: Summary of morphometric parameters obtained via ^3He MRI from 7 normal mice with histological comparison (not available for mice 6 and 7). The table gives values of key parameters for our model: acinar airway radius R , alveolar depth h , mean linear intercept Lm , alveolar density N_a and alveolar surface-to-volume ratio S/V . Since there is not much variation from slice to slice in the same mouse, only mean values of the parameters for each mouse are shown here.

Mouse No.	R (μm)	h (μm)	Lm (μm)	N_a (mm^{-3})	S/V (cm^{-1})	Lm (Histology)
1	95.6 \pm 7.0	49.8 \pm 6.7	61.0 \pm 12.5	3920 \pm 829	702 \pm 88.6	54.5 \pm 5.0
2	100.4 \pm 6.4	49.2 \pm 4.4	66.0 \pm 10.2	3360 \pm 632	642 \pm 69.1	52.8 \pm 5.6
3	97.4 \pm 7.9	49.3 \pm 6.3	62.4 \pm 13.1	3760 \pm 854	689 \pm 86.7	49.6 \pm 5.6
4	94.7 \pm 6.7	51.3 \pm 5.9	58.7 \pm 11.6	4020 \pm 784	722 \pm 87.9	52.7 \pm 4.5
5	92.0 \pm 6.4	52.9 \pm 3.6	54.6 \pm 10.1	4390 \pm 871	762 \pm 105.0	50.6 \pm 3.4
6	103.3 \pm 5.8	58.3 \pm 3.9	60.1 \pm 8.8	3680 \pm 536	682 \pm 70.2	-
7	96.7 \pm 5.9	51.4 \pm 4.2	60.1 \pm 8.4	3760 \pm 670	688 \pm 82.4	-
Mean	97.2	51.7	60.5	3840	698	52.0
Std Dev	3.7	3.2	3.5	3920 \pm 829	702 \pm 88.6	1.9

Average value for all seven mice, for all voxels in this experiment is found to be 60.5 ± 3.5 μm , which compares well with our diffusion experiment and the mean $Lm = 61.7$ μm .

Table 7.3 also shows the data of the mean chord length measured by histology, conducted on the same mice, right after the MR *in vivo* scanning. The quantitative histology was conducted using the usual method (lungs were inflation-fixed, embedded in agar to random cut 2-3 mm blocks for post processing: 5 μm slices were cut and stained to determine the chord length and other physical parameters). The average of mean chord length using this direct method was found to be 52.4 μm . The small but statistically significant difference between the measurements by the two methods appears to be systematic and may relate to the histological preparation and imprecise estimation of tissue shrinkage.

7.4 References

1. **Mitzner, W., J. Fallica, and J. Bishai**, Anisotropic nature of mouse lung parenchyma. *Ann Biomed Eng.* **36**(12): p. 2111-20, 2008.
2. **Yablonskiy, D.A., A.L. Sukstanskii, J.C. Leawoods, D.S. Gierada, G.L. Bretthorst, S.S. Lefrak, J.D. Cooper, and M.S. Conradi**, Quantitative in vivo assessment of lung microstructure at the alveolar level with hyperpolarized ^3He diffusion MRI. *Proc Natl Acad Sci U S A.* **99**(5): p. 3111-6, 2002.
3. **Yablonskiy, D.A., A.L. Sukstanskii, J.C. Woods, D.S. Gierada, J.D. Quirk, J.C. Hogg, J.D. Cooper, and M.S. Conradi**, Quantification of lung microstructure with hyperpolarized ^3He diffusion MRI. *J Appl Physiol.* **107**(4): p. 1258-65, 2009.
4. **Fehrenbach, H., R. Voswinckel, V. Michl, T. Mehling, A. Fehrenbach, W. Seeger, and J.R. Nyengaard**, Neoalveolarisation contributes to compensatory lung growth following pneumonectomy in mice. *Eur Respir J.* **31**(3): p. 515-22, 2008.
5. **Kang, M.J., C.G. Lee, J.Y. Lee, C.S. Dela Cruz, Z.J. Chen, R. Enelow, and J.A. Elias**, Cigarette smoke selectively enhances viral PAMP- and virus-induced pulmonary innate immune and remodeling responses in mice. *J Clin Invest.* **118**(8): p. 2771-84, 2008.
6. **Knudsen, L., M. Ochs, R. Mackay, P. Townsend, R. Deb, C. Muhlfeld, J. Richter, F. Gilbert, S. Hawgood, K. Reid, and H. Clark**, Truncated recombinant human SP-D attenuates emphysema and type II cell changes in SP-D deficient mice. *Respir Res.* **8**: p. 70, 2007.
7. **Knudsen, L., E.R. Weibel, H.J. Gundersen, F.V. Weinstein, and M. Ochs**, Assessment of air space size characteristics by intercept (chord) measurement: an accurate and efficient stereological approach. *J Appl Physiol.* **108**(2): p. 412-21, 2010.
8. **Knust, J., M. Ochs, H.J. Gundersen, and J.R. Nyengaard**, Stereological estimates of alveolar number and size and capillary length and surface area in mice lungs. *Anat Rec (Hoboken).* **292**(1): p. 113-22, 2009.
9. **Lee, J., R. Reddy, L. Barsky, J. Scholes, H. Chen, W. Shi, and B. Driscoll**, Lung alveolar integrity is compromised by telomere shortening in telomerase-null mice. *Am J Physiol Lung Cell Mol Physiol.* **296**(1): p. L57-70, 2009.

10. **Soutiere, S.E. and W. Mitzner**, On defining total lung capacity in the mouse. *J Appl Physiol.* **96**(5): p. 1658-64, 2004.
11. **Voswinckel, R., V. Motejl, A. Fehrenbach, M. Wegmann, T. Mehling, H. Fehrenbach, and W. Seeger**, Characterisation of post-pneumonectomy lung growth in adult mice. *Eur Respir J.* **24**(4): p. 524-32, 2004.
12. **Haefeli-Bleuer, B. and E.R. Weibel**, Morphometry of the human pulmonary acinus. *Anat Rec.* **220**(4): p. 401-14, 1988.
13. **Rodriguez, M., S. Bur, A. Favre, and E.R. Weibel**, Pulmonary acinus: geometry and morphometry of the peripheral airway system in rat and rabbit. *Am J Anat.* **180**(2): p. 143-55, 1987.
14. **Bachofen, H., S. Schurch, M. Urbinelli, and E.R. Weibel**, Relations among alveolar surface tension, surface area, volume, and recoil pressure. *J Appl Physiol.* **62**(5): p. 1878-87, 1987.
15. **Hartroft, W.S.**, The Microscopic Diagnosis of Pulmonary Emphysema. *Am J Pathol.* **21**(5): p. 889-903, 1945.
16. **Wang, W., N.M. Nguyen, D.A. Yablonskiy, A.L. Sukstanskii, E. Osmanagic, J.J. Atkinson, M.S. Conradi, and J.C. Woods**, Imaging lung microstructure in mice with hyperpolarized ³He diffusion MRI. *Magn Reson Med.* **65**(3): p. 620-6, 2011.
17. **Dugas, J.P., J.R. Garbow, D.K. Kobayashi, and M.S. Conradi**, Hyperpolarized (³He) MRI of mouse lung. *Magn Reson Med.* **52**(6): p. 1310-7, 2004.

Chapter 8 - Conclusion

8.1 Accomplishments

The accomplishments of this research are in both scientific and technological domain.

8.1.1 Mouse Lung Microstructure Measurements

First, scientifically, we established empirical relationships that connect MRI measurements of ^3He gas diffusion-attenuated MRI signal in mouse lungs with the geometrical parameters of lung acinar airways. We applied the new mathematical model to study mouse lungs and demonstrated that MR-based measurements of hyperpolarized ^3He gas diffusion in mouse lungs provide quantitative information on acinar airway dimensions and lung surface-to-volume ratio consistent with published histological values and our direct estimates.

8.1.2 Anisotropic Nature of Mouse Lungs

Additionally, our measurements of the lung anisotropy provided conclusive relationship between lung microstructure and the anisotropic diffusion in the mouse lungs. As mentioned in Chapter II, the lung environment is microscopically anisotropic and macroscopically isotropic system (assuming uniform orientation of the lung airways) and the measured MR signal is non-mono-exponential in b-value in humans [1, 2] and mice [3]. Such non-mono-exponential dependence can be caused by other factors, e.g. presence of multiple spherical compartments of varied sizes. This study established a relationship between the non-mono-exponential behavior of the MR signal and the diffusion anisotropy at the microscopic level. In short, our measurements confirmed that the diffusion of ^3He gas in the mouse lung is

anisotropic at the microscopic level but practically isotropic at the macroscopic level thus explaining the non-mono-exponential behavior of diffusion attenuated MR signal in lungs.

8.1.3 Adaptive MR Sequence for Optimal use of Gradient

Budget

Technologically, we developed an adaptive MR sequence to effectively take full advantage of the gradient strength budget, while staying within the constraints of the developed mathematical model and within operating parameters of the hardware used. Direct outcome is the new MR protocol able to acquire data with much shorter diffusion times as compared to human measurements, to accommodate the substantially smaller acinar airway length as those found in mice. The basis of the sequence is used for other similar mouse lung MR measurements for both *in vivo* and *ex vivo*.

8.2 Directions for Future Study

8.2.1 Known Experiment Limitations

We would not demonstrate the scientific rigor and full awareness of aspects of the research conducted here without discussing known limitations. Although studies are with merit, more measurements could have been taken to allow for richer set of results. Also, another branch of experiments could have been conducted (e.g. study of lungs with chemically induced emphysema or lungs damaged with smoke) to show comparison and to draw conclusions. Additionally, collaboration with other departments and universities in adoption of the gold standard method for direct lung microstructure measurements would provide more sound scientific comparison of our newly developed MR mouse lung methods.

Further, although developed theory assumes that no ^3He atoms will escape observed airways (not case in practice), published papers on similar measurements in humans provide evidence that actual MR measurements are impacted with less than 7% of accuracy. Diffusion times used in mice are substantially shorter than those in humans, as the airways are. Similar study on impact of escaping ^3He atoms into adjacent airways would provide a valuable insight and potential modulation of this study.

Triggering the MR measurements at the magnet (right upon delivering the HP ^3He gas to the mouse lungs and inserting the carrier into the magnet), rather than walking to the magnet and triggering them at the console would improve the SNR and reduce the noise floor, in turn potentially allowing for further flip angle increase (flip angle was chosen conservatively to hedge ourselves from the proximity of the noise floor).

Unfortunately, the ongoing progressive scarcity and high cost of ^3He gas limits wide scope of studies with large sample population in this area. Though certain steps are currently taken to address this issue, among them – ^3He gas recycling which offers substantial reduction in experimental costs.

8.2.2 This Study and Future Work

The MR measurements of lung microstructure appear to be in good correlation with histological findings and other similar published studies. We regard these diffusion measurements as closely reflective of true mouse lung microstructure physical parameters. The method we developed here creates a basis for *in vivo* study of lung microstructure in small animals, similar to the previously developed method of ^3He Lung Morphometry in

humans [2, 4]. It also creates a basis for ex vivo work on other area of lung studies (e.g. lung development and diseased lungs).

The development of the MR diffusion sequence used on such small subject that produces results in good correlation with the histological findings, paves two paths. One is to use the sequence in other experiments (e.g. in vivo, where the HP noble gas is continuously delivered). This in fact has been done: the sequence developed in this dissertation has been used as a basis to develop imaging sequence with focus on voxels of interest in the lungs. The other is to use the HP noble gas apparatus in different experiments (e.g. with newborn mice to observe for example lung developmental process, or with different small animals such as rats in similar experiments). Similarly, we used the tools developed in this work to conduct experiments on newborn mice.

Additionally, as the ^3He gas is becoming prohibitively more expensive and there are drives to recycle it, the gas delivery apparatus makes it easy to do both, save unused gas and recycle the gas used in the experiment.

Also, moving the mathematical model from the human lungs to mice lungs, in spite of the successful results, can be questioned. Developing similar model for rats or a model for xenon for both mice and rats would drastically add to the validation of the method and the tools used.

8.3 References

1. **Yablonskiy, D.A., A.L. Sukstanskii, J.C. Leawoods, D.S. Gierada, G.L. Bretthorst, S.S. Lefrak, J.D. Cooper, and M.S. Conradi**, Quantitative in vivo assessment of lung microstructure at the alveolar level with hyperpolarized ^3He diffusion MRI. *Proc Natl Acad Sci U S A*. **99**(5): p. 3111-6, 2002.
2. **Yablonskiy, D.A., A.L. Sukstanskii, J.C. Woods, D.S. Gierada, J.D. Quirk, J.C. Hogg, J.D. Cooper, and M.S. Conradi**, Quantification of lung microstructure with hyperpolarized ^3He diffusion MRI. *J Appl Physiol*. **107**(4): p. 1258-65, 2009.
3. **Osmanagic, E., A.L. Sukstanskii, J.D. Quirk, J.C. Woods, R.A. Pierce, M.S. Conradi, E.R. Weibel, and D.A. Yablonskiy**, Quantitative assessment of lung microstructure in healthy mice using an MR-based ^3He lung morphometry technique. *J Appl Physiol*. **109**(6): p. 1592-9, 2010.
4. **Wang, W., N.M. Nguyen, D.A. Yablonskiy, A.L. Sukstanskii, E. Osmanagic, J.J. Atkinson, M.S. Conradi, and J.C. Woods**, Imaging lung microstructure in mice with hyperpolarized ^3He diffusion MRI. *Magn Reson Med*. **65**(3): p. 620-6, 2011.

Appendix A - Source Code for Flip Angle and Eddy Currents Measurements

A1 Flip Angle Measurement and Calibration

```
#ifndef LINT
static char SCCSid[] = "@(#)s2pul.c 14.1 12/08/98 Copyright
(c) 1991-1996 Varian Assoc.,Inc. All Rights Reserved";
#endif

/* s2pul - standard two-pulse sequence */

#include <standard.h>

pulsesequence()
{
    /* equilibrium period */
    status(A);
    hsdelay(d1);

    /* --- tau delay --- */
    status(B);
    pulse(p1, zero);
    hsdelay(d2);

    /* --- observe period --- */
    status(C);
    pulse(pw, oph);
}
```

A2 Eddy Current Pulse Sequence

```
#ifndef LINT
static char SCCSid[] = "@(#)semsdw.c 13.1 10/10/97
Copyright (c) 1991-1995 Varian Assoc.,Inc. All Rights
Reserved";
```

```

#endif
/*
 * Varian Assoc., Inc. All Rights Reserved.
 * This software contains proprietary and confidential
 * information of Varian Assoc., Inc. and its contributors.
 * Use, disclosure and reproduction is prohibited without
 * prior consent.
 */
/*****
****
SEDFWS.C
Spin-echo diffusion spectroscopy sequence with optional
CHESS water suppression
010104 deleted acquire command. This added or subtracted a
delay so that echo was not centered. This caused a
1st order phase shift.
000511 Add ir option. Can be used to find null point for
STIR imaging. Suppress water with diffusion.
991001 Add option of putting gradients for water
suppression on in two directions and alternating the
axis so all three are orthogonal. Usage is wstype = 1
or 2 where 1 is the 1-2-4 height from earlier.
990903 Added the option to turn on all gradients at once
for diffusion. Direction refered to as 'a' for all.
Allows 1.732x gradient height by vector sum. Added
notification of gmax and bmax.
990813 phase cycling changed to 4 transient EXORCYCLE of
Bodenhausen (1977) with subsequent increment in p1 to
give 16 transient cycling. The previous phase cycling
was from the imaging sequence and inappropriate.
990812 CHESS gradient height changed to 1-2-4, and on in
all three directions to get a higher maximum spoiler
by vector addition. Different heights suggested by
Moonen and van Zijl.
990811 abort_flag created so all timing errors are listed
at one time
990329 created from semsdw.c by Jon Sehy water suppression
and b calculation from presstd2.c gradient direction
code from Victor Song
081001 retrofitted the code for exploiting eddy currents -
Emir Osmanagic
*-*-*-*-*-*-*-*-*-*-*-*-*-*-*-*-*-*-*-*-*-*-*-*-*-*-*-*-*-*-*
*-*-*
RF ---- [90] ----- [180] -----
|**ACQ**|-
< - - - - - te - - - - -
>

```

```

GDIFF
_____
////////\_____////////\
_____
                                <tA><tdelta> <tB>          <tC><tdelta>
<tD>
                                < - - - - tDELTA - - >
*-*-*-*-*-*-*-*-*-*-*-*-*-*-*-*-*-*-*-*-*-*-*-*-*-*-*-*-*-*-*-*-*-*-*-*-*
*-*-* /
#include <standard.h>

pulsesequance()
{
    /* INTERNAL VARIABLE DECLARATIONS
    *****/
    double  predelay, seqtime, tA, tB, tC, tD, rgdiff, crushg;
    double  temin, tDELTAmax, tDELTAmin, tau1, tau2, b;
    double
grate, gmr, half_gspoil, quarter_gspoil, vectorsum=1, bmax;
    char    dir[MAXSTR], dircg[MAXSTR], gpn[MAXSTR];
    int
dir_ro=0, dir_pe=0, dir_ss=0, abort_flag=0, wstype=1;
    int     dircg_ro=0, dircg_pe=0, dircg_ss=0;

    initparms_sis();
    grate = trise/gmax;
    half_gspoil=gspoil/2.0;
    quarter_gspoil=gspoil/4.0;
    rgdiff=getval("rgdiff");
    crushg=getval("crushg");
    wstype = getval("wstype");
    b = getval("b");
    getstr("dir", dir);
    getstr("dircg", dircg);
    getstr("gpn", gpn);

    if((dir[0]=='x') || (dir[0]=='X'))
        dir_ro=1;
    else if ((dir[0]=='y') || (dir[0]=='Y'))
        dir_pe=1;
    else if ((dir[0]=='a') || (dir[0]=='A')) {
        dir_ro=1;
        dir_pe=1;
        dir_ss=1;
        vectorsum=1.732;
    }
}

```

```

else
    dir_ss=1;

if((dircg[0]=='x') || (dircg[0]=='X'))
    dircg_ro=1;
else if ((dircg[0]=='y') || (dircg[0]=='Y'))
    dircg_pe=1;
else if ((dircg[0]=='a') || (dircg[0]=='A')) {
    dircg_ro=1;
    dircg_pe=1;
    dircg_ss=1;
}
else
    dircg_ss=1;

/* CHECK MAXIMUM tDELTA FOR TE, AND MINIMUM TE FOR tdelta
*/
    tDELTAmax = te - p1/2.0 - rof1 - tdelta - trise;
    temin = tDELTA + tdelta + p1/2.0 + rof1 + trise;

if (tDELTA > tDELTAmax) {
    printf("SEDFWS: tDELTA too large for te.  Max tDELTA =
%f.",tDELTAmax);
    printf("  Min te = %f\n",temin);
    abort_flag=1;
}

/* CHECK MINIMUM tDELTA FOR p2 AND tdelta */
/* tDELTAmin = p2 + 2.0*rof1 + tdelta + trise; */
    tDELTAmin = 2.0*rof1 + tdelta + trise;
    if (tDELTA < tDELTAmin) {
/*    printf("SEDFWS: tDELTA too small for p2;  Min
tDELTA = %f\n",tDELTAmin); */
        printf("SEDFWS: tDELTA too small;  Min tDELTA =
%f\n",tDELTAmin);
        abort_flag=1;
    }

/* TAU1 AND TAU2 ARE THE SUMS OF ALL EVENTS IN EACH HALF-
ECHO PERIOD */
/* tau1 = (p1 + p2)/2.0 + 2.0*rof1 + tdelta + trise; */
/* tau2 = p2/2.0 + rof1 + tdelta + trise; */
    tau1 = p1/2.0 + rof1 + tdelta + trise;
    tau2 = rof1 + tdelta + trise;
    temin = (tau1 < tau2) ? 2.0*tau2 : 2.0*tau1;

```

```

    if (te < temin) {
        printf("SEDFWS: te too small for tdelta.  Minimum te =
%f\n",temin);
        abort_flag=1;
    }

/* ADDITIONAL DELAYS TO POSITION DIFFUSION GRADIENTS */
    if (tDELTAmax - tDELTA > tDELTA - tDELTAmin) {
        tB = (tDELTA - tDELTAmin)/2.0;
        /* tC = (tDELTA - tDELTAmin)/2.0;    */
        tA = te/2.0 - tau1 - tB;
        /* tD = te/2.0 - tau2 - tC;          */
        tC = 0.0005;
        tD = 0.0005;
    }
    else {
        tA = (tDELTAmax - tDELTA)/2.0;
        /* tD = (tDELTAmax - tDELTA)/2.0;    */
        tB = te/2.0 - tau1 - tA;
        /* tC = te/2.0 - tau2 - tD;          */
        tC = 0.0005;
        tD = 0.0005;
    }

    if (tA < 0) {
        printf("SEDFWS: tA cannot be negative.");
        abort_flag=1;
    }

    if (tB < 0) {
        printf("SEDFWS: tB cannot be negative.");
        abort_flag=1;
    }

/*if (tC < 0) { */
/*     printf("SEDFWS: tC cannot be negative."); */
/*     abort_flag=1; */
/*     } */

/*if (tD < 0) { */
/*     printf("SEDFWS: tD cannot be negative."); */
/*     abort_flag=1; */
/*     } */

/* RELAXATION DELAY */
    seqtime = te + p1/2.0 + rof1 + at;
    if ((ws[0]=='y') || (ws[0]=='Y'))

```

```

    seqtime = seqtime + 3*(psat + tspoil + trise +
2.0*rofl);
    predelay = tr - seqtime;
    if (predelay < 0.0) {
        printf("SEDFWS: Requested tr too short.  Min tr =
%f\n",seqtime);
        abort_flag=1;
    }

    if (abort_flag == 1) {
        abort(1);
    }

/* COMPUTE b VALUES *****/

    gmr = 26750/199.35*sfrq;      /* gmr = gyromagnetic
ratio */
    /* gdiff=(sqrt(b/(gmr*gmr*tdelta*tdelta*(tDELTA-
tdelta/3.0))))/vectorsum; */
    gdiff=(sqrt(b/(gmr*gmr*(tdelta*tdelta*(tDELTA-
tdelta/3.0)+rgdiff*(tdelta*tdelta-
2*tDELTA*tdelta+rgdiff*tDELTA-
7/6*rgdiff*tdelta+8/15*rgdiff*rgdiff)))/vectorsum;

bmax=(vectorsum*gmax)*(vectorsum*gmax)*(gmr*gmr*(tdelta*tde
lta*(tDELTA-tdelta/3.0)+rgdiff*(tdelta*tdelta-
2*tDELTA*tdelta+rgdiff*tDELTA-
7/6*rgdiff*tdelta+8/15*rgdiff*rgdiff)));

    printf("Gradient: %7.4f  Grad vector sum: %7.3f  tdiff:
%7.3f  ",gdiff,gdiff*vectorsum,tDELTA-tdelta/3);
    printf("gmax: %7.3f  bmax: %7.3f  GradTrise req: %7.6f
SysTrise for gdiff:
%7.6f\n",gmax*vectorsum,bmax,rgdiff,gdiff*0.000378/60+0.000
022);
    if (gdiff>gmax) {
        text_error("ERROR:  max gradient exceeded");
        abort(1);
    }
    if (gdiff*0.000378/60+0.000022>rgdiff) {
        printf("Requested gdiff rise time exceeds system
capabilities, eg. rgdiff: %7.6f  systems: %7.6f\n", rgdiff,
gdiff*0.000378/60+0.000022);
    }

/* PULSE SEQUENCE *****/

```

```

/* PHASE CYCLE, 16 TRANSIENT
EXORCYCLE******/
mod4(ct,v4); /* v4 = 0123012301230123 */
hlv(v4,v3); /* v3 = 0011223300112233 */
hlv(v3,v1); /* v1 = 0000111122223333 */
add(v1,v4,v2); /* v2 = 0123123023013012 */
mod2(v4,v4); /* v4 = 0101010101010101 */
dbl(v4,v4); /* v4 = 0202020202020202 */
add(v4,v1,oph); /* oph = 0202131320203131 */
mod4(v1,v1);
mod4(v2,v2);
mod4(oph,oph);

/* Relaxation delay
******/
status(A);
delay(predelay - 3*tdelta-3*trise-0.3);

oblique_gradient(dircg_ro*crushg,dircg_pe*crushg,dircg_ss*c
rushg,0.0,0.0,0.0);
delay(tdelta);
zero_all_gradients();
delay(trise + 0.0005);
/*
oblique_gradient(dir_pe*gdiff,dir_ro*gdiff,dir_ss*gdiff,0.0
,0.0,0.0); */
/* delay(tdelta);
*/
/* zero_all_gradients();
*/
/* delay(trise + 0.1);
*/
/*
oblique_gradient(dir_pe*gdiff,dir_ro*gdiff,dir_ss*gdiff,0.0
,0.0,0.0); */
/* delay(tdelta);
*/
/* zero_all_gradients();
*/
/* delay(trise + 0.1);
*/

/* Optional water suppression
******/

if ((ws[0]=='y') || (ws[0]=='Y')) {

```

```

    obspower(satpwr);
    obsoffset(wsfrq);

    shapedpulse(satpat,psat,zero,rof1,rof1);

    if (wstype == 1) {

oblique_gradient(quarter_gspoil,quarter_gspoil,quarter_gspo
il,0.0,0.0,0.0);
        delay(tspoil);
        zero_all_gradients();
        delay(trise);

        shapedpulse(satpat,psat,zero,rof1,rof1);

oblique_gradient(half_gspoil,half_gspoil,half_gspoil,0.0,0.
0,0.0);
        delay(tspoil);
        zero_all_gradients();
        delay(trise);

        shapedpulse(satpat,psat,zero,rof1,rof1);

oblique_gradient(gspoil,gspoil,gspoil,0.0,0.0,0.0);
    }
    else {
        oblique_gradient(gspoil,gspoil,0.0,0.0,0.0,0.0);
        delay(tspoil);
        zero_all_gradients();
        delay(trise);

        shapedpulse(satpat,psat,zero,rof1,rof1);

oblique_gradient(0.0,gspoil,gspoil,0.0,0.0,0.0);
        delay(tspoil);
        zero_all_gradients();
        delay(trise);

        shapedpulse(satpat,psat,zero,rof1,rof1);

oblique_gradient(gspoil,0.0,gspoil,0.0,0.0,0.0);
    }
    delay(tspoil);
    zero_all_gradients();
    delay(trise);
    }
    obsoffset(tof);

```

```

/* Optional Inversion-Recovery pulse */
  if (ir[0] == 'y') {
    obspower(tpwri);
    shapedpulse(pipat,pi,v1,rof1,rof1);
    delay(ti);
  }

/* 90 degree pulse
*****/
  obspower(tpwr1);
  shaped_pulse(plpat,p1,v1,rof1,rof1);

/* First half-TE period and diffusion gradient
*****/
  delay(0.0005);

  if((gpn[0]=='p') || (gpn[0]=='P')) {

obl_shapedgradient("linear_ramp_up","linear_ramp_up","linear_ramp_up",rgdiff,dir_ro*gdiff,dir_pe*gdiff,dir_ss*gdiff,1,WAIT);
    delay(tdelta-rgdiff);

obl_shapedgradient("linear_ramp_down","linear_ramp_down","linear_ramp_down",rgdiff,dir_ro*gdiff,dir_pe*gdiff,dir_ss*gdiff,1,WAIT);
  }
  else {

obl_shapedgradient("linear_ramp_up","linear_ramp_up","linear_ramp_up",rgdiff,-dir_ro*gdiff,-dir_pe*gdiff,-dir_ss*gdiff,1,WAIT);
    delay(tdelta-rgdiff);

obl_shapedgradient("linear_ramp_down","linear_ramp_down","linear_ramp_down",rgdiff,-dir_ro*gdiff,-dir_pe*gdiff,-dir_ss*gdiff,1,WAIT);
  }
  zero_all_gradients();
  delay(tB + trise);

/* 180 degree pulse
*****/
  /* obspower(0); */
  /* shaped_pulse(p2pat,p2,v2,rof1,rof1); */

```

```

        /* Second half-TE period and diffusion gradient
        *****/
        delay(tC);

        if((gpn[0]=='p') || (gpn[0]=='P')) {

obl_shapedgradient("linear_ramp_up","linear_ramp_up","linear_ramp_up",rgdiff,-dir_ro*gdiff,-dir_pe*gdiff,-dir_ss*gdiff,1,WAIT);
                delay(tdelta-rgdiff);

obl_shapedgradient("linear_ramp_down","linear_ramp_down","linear_ramp_down",rgdiff,-dir_ro*gdiff,-dir_pe*gdiff,-dir_ss*gdiff,1,WAIT);
        }
        else {

obl_shapedgradient("linear_ramp_up","linear_ramp_up","linear_ramp_up",rgdiff,dir_ro*gdiff,dir_pe*gdiff,dir_ss*gdiff,1,WAIT);
                delay(tdelta-rgdiff);

obl_shapedgradient("linear_ramp_down","linear_ramp_down","linear_ramp_down",rgdiff,dir_ro*gdiff,dir_pe*gdiff,dir_ss*gdiff,1,WAIT);
        }
        zero_all_gradients();
        delay(trise + tD);

        /* Acquire echo
        *****/
}

```

Appendix B - Source Code for Lung Microstructure and Anisotropy Experiments

B1 Pulse Sequence for Determining Mouse Lung Microstructure

```
#ifndef LINT
static char SCCSid[] = "@(#)semsdw.c 13.1 10/10/97
Copyright (c) 1991-1995 Varian Assoc., Inc. All Rights
Reserved";
#endif
/*
 * Varian Assoc., Inc. All Rights Reserved.
 * This software contains proprietary and confidential
 * information of Varian Assoc., Inc. and its contributors.
 * Use, disclosure and reproduction is prohibited without
 * prior consent.
 */
/*****
*****
SEDFWS.C
Spin-echo diffusion spectroscopy sequence with optional
CHESS water suppression
010104 deleted acquire command. This added or subtracted a
delay so that echo was not centered. This caused a
1st order phase shift.
000511 Add ir option. Can be used to find null point for
STIR imaging. Suppress water with diffusion.
991001 Add option of putting gradients for water
suppression on in two directions and alternating the
axis so all three are orthogonal. Usage is wstype = 1
or 2 where 1 is the 1-2-4 height from earlier.
990903 Added the option to turn on all gradients at once
for diffusion. Direction referred to as 'a' for all.
Allows 1.732x gradient height by vector sum. Added
notification of gmax and bmax.
990813 phase cycling changed to 4 transient EXORCYCLE of
Bodenhausen (1977) with subsequent increment in p1 to
```

give 16 transient cycling. The previous phase cycling was from the imaging sequence and inappropriate.

990812 CHESS gradient height changed to 1-2-4, and on in all three directions to get a higher maximum spoiler by vector addition. Different heights suggested by Moonen and van Zijl.

990811 abort_flag created so all timing errors are listed at one time

990329 created from semsdw.c by Jon Sehy water suppression and b calculation from presstd2.c gradient direction code from Victor Song

080601 retrofitted the code for diffusion measurements using 3He by using one independently set crusher gradient scaled down expression for "b", use one 90 degree pulse only and the second gradient negative, making "b" variable real. -Emir Osmanagic

```
*-*-*-*-*-*-*-*-*-*-*-*-*-*-*-*-*-*-*-*-*-*-*-*-*-*-*-*-*-*-*
*-*-*-*-*-*-*-*-*
```

```
RF    ----- [90] ----- [180] -----
- |** ACQ **|-
      < - - - - - - - - - - - te - - - - - - - - - - -
- - - >
```

```
GDIFD
_____ //////////////\_____ //////////////\_____
_____
      <tA><tDelta> <tB>      <tC><tDelta>
<tD>
      < - - - - - tDELTA - - >
```

```
*-*-*-*-*-*-*-*-*-*-*-*-*-*-*-*-*-*-*-*-*-*-*-*-*-*-*-*-*-*-*
*-*-*-*-*-*-*-*-*
```

```
#include <standard.h>

pulsesequence()
{
    /* INTERNAL VARIABLE DECLARATIONS
    *****/
    double  predelay, seqtime, tA, tB, tC, tD, rgdiff, crushg;
    double  temin, tDELTAmax, tDELTAmin, tau1, tau2, b;
```

```

double
grate,gmr, half_gspoil, quarter_gspoil, vectorsum=1, bmax;
char    dir[MAXSTR], dircg[MAXSTR], gpn[MAXSTR];
int
dir_ro=0, dir_pe=0, dir_ss=0, abort_flag=0, wstype=1;
int     dircg_ro=0, dircg_pe=0, dircg_ss=0;

initparms_sis();
grate = trise/gmax;
half_gspoil=gspoil/2.0;
quarter_gspoil=gspoil/4.0;
rgdiff=getval("rgdiff");
crushg=getval("crushg");
wstype = getval("wstype");
b = getval("b");
getstr("dir", dir);
getstr("dircg", dircg);
getstr("gpn", gpn);

if((dir[0]=='x') || (dir[0]=='X'))
    dir_ro=1;
else if ((dir[0]=='y') || (dir[0]=='Y'))
    dir_pe=1;
else if ((dir[0]=='a') || (dir[0]=='A')) {
    dir_ro=1;
    dir_pe=1;
    dir_ss=1;
    vectorsum=1.732;
}
else
    dir_ss=1;

if((dircg[0]=='x') || (dircg[0]=='X'))
    dircg_ro=1;
else if ((dircg[0]=='y') || (dircg[0]=='Y'))
    dircg_pe=1;
else if ((dircg[0]=='a') || (dircg[0]=='A')) {
    dircg_ro=1;
    dircg_pe=1;
    dircg_ss=1;
}
else
    dircg_ss=1;

```

```

/* CHECK MAXIMUM tDELTA FOR TE, AND MINIMUM TE FOR tdelta
*/
    tDELTAmax = te - p1/2.0 - rof1 - tdelta - trise;
    temin = tDELTA + tdelta + p1/2.0 + rof1 + trise;

    if (tDELTA > tDELTAmax) {
        printf("SEDFWS: tDELTA too large for te.  Max tDELTA =
%f.",tDELTAmax);
        printf("  Min te = %f\n",temin);
        abort_flag=1;
    }

/* CHECK MINIMUM tDELTA FOR p2 AND tdelta */
/* tDELTAmin = p2 + 2.0*rof1 + tdelta + trise; */
    tDELTAmin = 2.0*rof1 + tdelta + trise;
    if (tDELTA < tDELTAmin) {
        /* printf("SEDFWS: tDELTA too small for p2;  Min
tDELTA = %f\n",tDELTAmin); */
        printf("SEDFWS: tDELTA too small;  Min tDELTA =
%f\n",tDELTAmin);
        abort_flag=1;
    }

/* TAU1 AND TAU2 ARE THE SUMS OF ALL EVENTS IN EACH HALF-
ECHO PERIOD */
/* tau1 = (p1 + p2)/2.0 + 2.0*rof1 + tdelta + trise; */
/* tau2 = p2/2.0 + rof1 + tdelta + trise; */
    tau1 = p1/2.0 + rof1 + tdelta + trise;
    tau2 = rof1 + tdelta + trise;
    temin = (tau1 < tau2) ? 2.0*tau2 : 2.0*tau1;
    if (te < temin) {
        printf("SEDFWS: te too small for tdelta.  Minimum te =
%f\n",temin);
        abort_flag=1;
    }

/* ADDITIONAL DELAYS TO POSITION DIFFUSION GRADIENTS */
    if (tDELTAmax - tDELTA > tDELTA - tDELTAmin) {
        tB = (tDELTA - tDELTAmin)/2.0;
        /* tC = (tDELTA - tDELTAmin)/2.0; */
        tA = te/2.0 - tau1 - tB;
        /* tD = te/2.0 - tau2 - tC; */
        tC = 0.0005;
        tD = 0.0005;
    }
    else {
        tA = (tDELTAmax - tDELTA)/2.0;

```

```

        /* tD = (tDELTAmax - tDELTA)/2.0;    */
    tB = te/2.0 - tau1 - tA;
    /* tC = te/2.0 - tau2 - tD;            */
    tC = 0.0005;
    tD = 0.0005;
}

if (tA < 0) {
    printf("SEDFWS: tA cannot be negative.");
    abort_flag=1;
}

if (tB < 0) {
    printf("SEDFWS: tB cannot be negative.");
    abort_flag=1;
}

/*if (tC < 0) { */
/*    printf("SEDFWS: tC cannot be negative."); */
/*    abort_flag=1; */
/*    } */

/*if (tD < 0) { */
/*    printf("SEDFWS: tD cannot be negative."); */
/*    abort_flag=1; */
/*    } */

/* RELAXATION DELAY */
seqtime = te + p1/2.0 + rof1 + at;
if ((ws[0]=='y') || (ws[0]=='Y'))
    seqtime = seqtime + 3*(psat + tspoil + trise +
2.0*rof1);
predelay = tr - seqtime;
if (predelay < 0.0) {
    printf("SEDFWS: Requested tr too short.  Min tr =
%f\n",seqtime);
    abort_flag=1;
}

if (abort_flag == 1) {
    abort(1);
}

/* COMPUTE b VALUES *****/

    gmr = 26750/199.35*sfrq;    /* gmr = gyromagnetic
ratio */

```

```

/* gdiff=(sqrt(b/(gmr*gmr*tdelta*tdelta*(tDELTA-
tdelta/3.0))))/vectorsum; */
gdiff=(sqrt(b/(gmr*gmr*(tdelta*tdelta*(tDELTA-
tdelta/3.0)+rgdiff*(tdelta*tdelta-
2*tDELTA*tdelta+rgdiff*tDELTA-
7/6*rgdiff*tdelta+8/15*rgdiff*rgdiff)))/vectorsum;

bmax=(vectorsum*gmax)*(vectorsum*gmax)*(gmr*gmr*(tdelta*tdelta-
tdelta/3.0)+rgdiff*(tdelta*tdelta-
2*tDELTA*tdelta+rgdiff*tDELTA-
7/6*rgdiff*tdelta+8/15*rgdiff*rgdiff));

printf("Gradient: %7.4f  Grad vector sum: %7.3f  tdiff:
%7.3f  ",gdiff,gdiff*vectorsum,tDELTA-tdelta/3);
printf("gmax: %7.3f  bmax: %7.3f  GradTrise req: %7.6f
SysTrise for gdiff:
%7.6f\n",gmax*vectorsum,bmax,rgdiff,gdiff*0.000378/60+0.000
022);
if (gdiff>gmax) {
text_error("ERROR:  max gradient exceeded");
abort(1);
}
if (gdiff*0.000378/60+0.000022>rgdiff) {
printf("Requested gdiff rise time exceeds system
capabilities, eg. rgdiff: %7.6f  systems: %7.6f\n", rgdiff,
gdiff*0.000378/60+0.000022);
}

/* PULSE SEQUENCE *****/

/* PHASE CYCLE, 16 TRANSIENT
EXORCYCLE*****/
mod4(ct,v4); /* v4 = 0123012301230123 */
hlv(v4,v3); /* v3 = 0011223300112233 */
hlv(v3,v1); /* v1 = 0000111122223333 */
add(v1,v4,v2); /* v2 = 0123123023013012 */
mod2(v4,v4); /* v4 = 0101010101010101 */
dbl(v4,v4); /* v4 = 0202020202020202 */
add(v4,v1,oph); /* oph = 0202131320203131 */
mod4(v1,v1);
mod4(v2,v2);
mod4(oph,oph);

/* Relaxation delay
*****/
status(A);

```

```

        delay(predelay - 3*tdelta-3*trise-0.3);

oblique_gradient(dircg_ro*crushg,dircg_pe*crushg,dircg_ss*crushg,0.0,0.0,0.0);
        delay(tdelta);
        zero_all_gradients();
        delay(trise + 0.0005);
        /*
oblique_gradient(dir_pe*gdiff,dir_ro*gdiff,dir_ss*gdiff,0.0,0.0,0.0);    */
        /* delay(tdelta);
*/
        /* zero_all_gradients();
*/
        /* delay(trise + 0.1);
*/
        /*
oblique_gradient(dir_pe*gdiff,dir_ro*gdiff,dir_ss*gdiff,0.0,0.0,0.0);    */
        /* delay(tdelta);
*/
        /* zero_all_gradients();
*/
        /* delay(trise + 0.1);
*/
        /*
        /* Optional water suppression
        *****/

        if ((ws[0]=='y') || (ws[0]=='Y')) {
        obspower(satpwr);
        obsoffset(wsfrq);

        shapedpulse(satpat,psat,zero,rof1,rof1);

        if (wstype == 1) {

oblique_gradient(quarter_gspoil,quarter_gspoil,quarter_gspoil,0.0,0.0,0.0);
        delay(tspoil);
        zero_all_gradients();
        delay(trise);

        shapedpulse(satpat,psat,zero,rof1,rof1);

oblique_gradient(half_gspoil,half_gspoil,half_gspoil,0.0,0.0,0.0);

```

```

        delay(tspoil);
        zero_all_gradients();
        delay(trise);

        shapedpulse(satpat,psat,zero,rof1,rof1);

oblique_gradient(gspoil,gspoil,gspoil,0.0,0.0,0.0);
    }
    else {
        oblique_gradient(gspoil,gspoil,0.0,0.0,0.0,0.0);
        delay(tspoil);
        zero_all_gradients();
        delay(trise);

        shapedpulse(satpat,psat,zero,rof1,rof1);

oblique_gradient(0.0,gspoil,gspoil,0.0,0.0,0.0);
        delay(tspoil);
        zero_all_gradients();
        delay(trise);

        shapedpulse(satpat,psat,zero,rof1,rof1);

oblique_gradient(gspoil,0.0,gspoil,0.0,0.0,0.0);
    }
    delay(tspoil);
    zero_all_gradients();
    delay(trise);
}
obsoffset(tof);
/* Optional Inversion-Recovery pulse */
    if (ir[0] == 'y') {
        obspower(tpwri);
        shapedpulse(pipat,pi,v1,rof1,rof1);
        delay(ti);
    }

    /* 90 degree pulse
******/
    obspower(tpwr1);
    shaped_pulse(plpat,p1,v1,rof1,rof1);

    /* First half-TE period and diffusion gradient
******/
    delay(0.0005);

    if((gpn[0]=='p') || (gpn[0]=='P')) {

```



```

r_ramp_up",rgdiff,dir_ro*gdiff,dir_pe*gdiff,dir_ss*gdiff,1,
WAIT);
        delay(tdelta-rgdiff);

obl_shapedgradient("linear_ramp_down","linear_ramp_down","l
inear_ramp_down",rgdiff,dir_ro*gdiff,dir_pe*gdiff,dir_ss*gd
iff,1,WAIT);
    }
    zero_all_gradients();
    delay(trise + tD);

    /* Acquire echo
*****/
}

```

B2 Pulse Sequence for Demonstrating Anisotropy

```

#ifndef LINT
static char SCCSid[] = "@(#)semsdw.c 13.1 10/10/97
Copyright (c) 1991-1995 Varian Assoc.,Inc. All Rights
Reserved";
#endif
/*
 * Varian Assoc.,Inc. All Rights Reserved.
 * This software contains proprietary and confidential
 * information of Varian Assoc., Inc. and its contributors.
 * Use, disclosure and reproduction is prohibited without
 * prior consent.
 */
/*****
*****
SEDFWS.C
Spin-echo diffusion spectroscopy sequence with optional
CHESS water suppression
010104 deleted acquire command. This added or subtracted a
delay so that echo was not centered. This caused a
1st order phase shift.
000511 Add ir option. Can be used to find null point for
STIR imaging. Suppress water with diffusion.
991001 Add option of putting gradients for water
suppression on in two directions and alternating the

```

axis so all three are orthogonal. Usage is wstype = 1 or 2 where 1 is the 1-2-4 height from earlier.

990903 Added the option to turn on all gradients at once for diffusion. Direction referred to as 'a' for all. Allows 1.732x gradient height by vector sum. Added notification of gmax and bmax.

990813 phase cycling changed to 4 transient EXORCYCLE of Bodenhausen (1977) with subsequent increment in p1 to give 16 transient cycling. The previous phase cycling was from the imaging sequence and inappropriate.

990812 CHESS gradient height changed to 1-2-4, and on in all three directions to get a higher maximum spoiler by vector addition. Different heights suggested by Moonen and van Zijl.

990811 abort_flag created so all timing errors are listed at one time

990329 created from semsdw.c by Jon Sehy water suppression and b calculation from presstd2.c gradient direction code from Victor Song

080601 retrofitted the code for 3He by using one independently set crusher gradient scaled down expression for "b", use one 90 degree pulse only and the second gradient negative, making "b" variable real -Emir Osmanagic

081125 removed unused variables and calculations - Emir Osmanagic

091016 3D sequence (3-dir 2-grad pulses) with dir='xxx'/'xyz'/'zzz'.- Emir Osmanagic

-
 --*-*-*-*-*-*-*

```
RF    ----- [90] -----
- |** ACQ **|-
      < - - - - - - - - - - te - - - - -
- - - >
```

```
GDIFF _____ //////////////\ _____
                      \\\\\\\\\\\
                      <tdelta> <tdelta>
```

<tDELTA >

```

                                hint: tdelta=tDELTA
*-*-*-*-*-*-*-*-*-*-*-*-*-*-*-*-*-*-*-*-*-*-*-*-*-*-*-*-*-*-*-*-*-*-*-*-*
*-*-*-*-*-*-*-*-*-*-**/

#include <standard.h>

pulsesequence()
{
    /* INTERNAL VARIABLE DECLARATIONS
    *****/
    double  predelay, seqtime, rgdiff, crushg, gspoil=30;
    double  temin, tDELTAmax, tDELTAmin, tau1, tau2, b;
    double
grate, gmr, half_gspoil, quarter_gspoil, vectorsum=1, bmax;
    char    dir1[MAXSTR], dir2[MAXSTR], dir3[MAXSTR];
    int
dir_ro1=0, dir_pe1=0, dir_ss1=0, dir_ro2=0, dir_pe2=0, dir_ss2=0
, dir_ro3=0, dir_pe3=0, dir_ss3=0, wstype=1;

    initparms_sis();
    grate = trise/gmax;
    half_gspoil=gspoil/2.0;
    quarter_gspoil=gspoil/4.0;
    rgdiff=getval("rgdiff");

    wstype = getval("wstype");
    b = getval("b");
    crushg = getval("crushg");
    getstr("dir1", dir1);
    getstr("dir2", dir2);
    getstr("dir3", dir3);

    if(dir1[0]=='x')
        dir_ro1=1;
    else if (dir1[0]=='y')
        dir_pe1=1;
    else
        dir_ss1=1;

    if(dir2[0]=='x')
        dir_ro2=1;
    else if (dir2[0]=='y')
        dir_pe2=1;
    else
        dir_ss2=1;

```

```

    if(dir3[0]=='x')
        dir_ro3=1;
    else if (dir3[0]=='y')
        dir_pe3=1;
    else
        dir_ss3=1;

    /* CHECK MAXIMUM tDELTA FOR TE, AND MINIMUM TE FOR tdelta
    */
        tDELTAmax = te - p1/2.0 - tdelta;
        temin = tDELTA + tdelta + p1/2.0 + rof1;

        if (tDELTA > tDELTAmax) {
            abort_message("SEDFWS: tDELTA too large for te. Max
tDELTA = %f.",tDELTAmax);
            abort_message("  Min te = %f\n",temin);
        }

    /* CHECK MINIMUM tdelta FOR rgdiff */
        if (tdelta < 2*rgdiff) {
            abort_message("tdelta too small for rgdiff. Min tdelta
= %f.",2*rgdiff);
            abort_message("  rgdiff = %f.",rgdiff);
        }

    /* CHECK MINIMUM tDELTA FOR tdelta */
        tDELTAmmin = tdelta;
        if (tDELTA < tDELTAmmin) {
            /* abort_message("SEDFWS:tDELTA too small for p2; Min
tDELTA = %f\n",tDELTAmmin); */
            abort_message("SEDFWS: tDELTA too small; Min tDELTA
= %f\n",tDELTAmmin);
        }

    /* TAU1 AND TAU2 ARE THE SUMS OF ALL EVENTS IN EACH HALF-
ECHO PERIOD */
        tau1 = p1/2.0 + rof1 + tdelta;
        tau2 = rof1 + tdelta;
        temin = (tau1 < tau2) ? 2.0*tau2 : 2.0*tau1;
        if (te < temin) {
            abort_message("SEDFWS: te too small for tdelta.
Minimum te = %f\n",temin);

```

```

    }

/* RELAXATION DELAY */
    seqtime = te + p1/2.0 + rofl + at;
    if ((ws[0]=='y') || (ws[0]=='Y'))
        seqtime = seqtime + 3*(psat + tspoil + trise +
2.0*rofl);
    predelay = tr - seqtime;
    if (predelay < 0.0) {
        abort_message("SEDFWS: Requested tr too short. Min
tr = %f\n",seqtime);
    }

/* COMPUTE b VALUES *****/

    gmr = 26750/199.35*sfrq;      /* gmr = gyromagnetic
ratio */
    gdifff=(sqrt(b/(gmr*gmr*(tdelta*tdelta*(tDELTA-
tdelta/3.0)+rgdifff*(tdelta*tdelta-
2*tDELTA*tdelta+rgdifff*tDELTA-
7/6*rgdifff*tdelta+8/15*rgdifff*rgdifff)))))/vectorsum;

bmax=(vectorsum*gmax)*(vectorsum*gmax)*(gmr*gmr*(tdelta*tde
lta*(tDELTA-tdelta/3.0)+rgdifff*(tdelta*tdelta-
2*tDELTA*tdelta+rgdifff*tDELTA-
7/6*rgdifff*tdelta+8/15*rgdifff*rgdifff)));

    printf("Gradient: %6.4f; Grad vector sum: %6.4f; tdiff:
%6.3f; ",gdifff,gdifff*vectorsum,tDELTA-tdelta/3);
    printf("gmax: %6.2f; bmax: %6.1f; GradTrise req: %7.6f;
SysTrise for gdifff: %7.6f; tDELTAmin:
%7.5f;\n",gmax*vectorsum,bmax,rgdifff,gdifff*0.0002575/60+0.0
00007,tDELTAmin);
    if (gdifff>gmax) {
        text_error("ERROR: max gradient exceeded");
        abort_message("");
    }
    if (gdifff*0.0002575/60+0.000007>rgdifff) {

```

```

    printf("Requested gdiff rise time exceeds system
capabilities, eg. rgdiff: %7.6f  systems: %7.6f\n", rgdiff,
gdiff*0.0002575/60+0.000007);
    }

```

```

/* PULSE SEQUENCE *****/

```

```

    /* PHASE CYCLE, 16 TRANSIENT
EXORCYCLE*****/

```

```

    mod4(ct,v4); /* v4 = 0123012301230123 */
    hl v(v4,v3); /* v3 = 0011223300112233 */
    hl v(v3,v1); /* v1 = 0000111122223333 */
    add(v1,v4,v2); /* v2 = 0123123023013012 */
    mod2(v4,v4); /* v4 = 0101010101010101 */
    dbl(v4,v4); /* v4 = 0202020202020202 */
    add(v4,v1,oph); /* oph = 0202131320203131 */
    mod4(v1,v1);
    mod4(v2,v2);
    mod4(oph,oph);

```

```

    /* Relaxation delay
******/
    status(A);
    delay(predelay - 3*tdelta-0.3);
    obl_gradient(crushg,crushg,crushg);
    delay(tdelta);
    zero_all_gradients();
    delay(0.0005);

```

```

    /* Optional water suppression
******/

```

```

    if ((ws[0]=='y') || (ws[0]=='Y')) {
    obspower(satpwr);
    obsoffset(wsfrq);

    shapedpulse(satpat,psat,zero,rofl,rofl);

```

```

    if (wstype == 1) {

```

```

    obl_gradient(quarter_gspoil,quarter_gspoil,quarter_gspoil);
    delay(tspoil);
    zero_all_gradients();
    delay(trise);

```

```

    shapedpulse(satpat,psat,zero,rofl,rofl);

```

```

obl_gradient(half_gspoil, half_gspoil, half_gspoil);
    delay(tspoil);
    zero_all_gradients();
    delay(trise);

    shapedpulse(satpat, psat, zero, rof1, rof1);
    obl_gradient(gspoil, gspoil, gspoil);
}
else {
    obl_gradient(gspoil, gspoil, 0.0);
    delay(tspoil);
    zero_all_gradients();
    delay(trise);

    shapedpulse(satpat, psat, zero, rof1, rof1);
    obl_gradient(0.0, gspoil, gspoil);
    delay(tspoil);
    zero_all_gradients();
    delay(trise);

    shapedpulse(satpat, psat, zero, rof1, rof1);
    obl_gradient(gspoil, 0.0, gspoil);
}
delay(tspoil);
zero_all_gradients();
delay(trise);
}
obsoffset(tof);
/* Optional Inversion-Recovery pulse */
    if (ir[0] == 'y') {
        obspower(tpwri);
        shapedpulse(pipat, pi, v1, rof1, rof1);
        delay(ti);
    }

    /* 90 degree pulse
*****/
    obspower(tpwrl);
    shaped_pulse(plpat, p1, v1, rof1, rof1);

    delay(0.00001);

    /* First positive-TE period and diffusion gradient
*****/

```

```

obl_shapedgradient("linear_ramp_up",rgdiff,dir_ro1*gdiff,di
r_pe1*gdiff,dir_ss1*gdiff,WAIT);
    delay(tdelta-2*rgdiff);

obl_shapedgradient("linear_ramp_down",rgdiff,dir_ro1*gdiff,
dir_pe1*gdiff,dir_ss1*gdiff,WAIT);
    zero_all_gradients();

    /* First negative-TE period and diffusion gradient
*****/
    obl_shapedgradient("linear_ramp_up",rgdiff,-
dir_ro1*gdiff,-dir_pe1*gdiff,-dir_ss1*gdiff,WAIT);
    delay(tdelta-2*rgdiff);
    obl_shapedgradient("linear_ramp_down",rgdiff,-
dir_ro1*gdiff,-dir_pe1*gdiff,-dir_ss1*gdiff,WAIT);
    zero_all_gradients();

    /* Second positive-TE period and diffusion gradient
*****/

obl_shapedgradient("linear_ramp_up",rgdiff,dir_ro2*gdiff,di
r_pe2*gdiff,dir_ss2*gdiff,WAIT);
    delay(tdelta-2*rgdiff);

obl_shapedgradient("linear_ramp_down",rgdiff,dir_ro2*gdiff,
dir_pe2*gdiff,dir_ss2*gdiff,WAIT);
    zero_all_gradients();

    /* Second negative-TE period and diffusion gradient
*****/
    obl_shapedgradient("linear_ramp_up",rgdiff,-
dir_ro2*gdiff,-dir_pe2*gdiff,-dir_ss2*gdiff,WAIT);
    delay(tdelta-2*rgdiff);
    obl_shapedgradient("linear_ramp_down",rgdiff,-
dir_ro2*gdiff,-dir_pe2*gdiff,-dir_ss2*gdiff,WAIT);
    zero_all_gradients();

    /* Third positive-TE period and diffusion gradient
*****/

obl_shapedgradient("linear_ramp_up",rgdiff,dir_ro3*gdiff,di
r_pe3*gdiff,dir_ss3*gdiff,WAIT);
    delay(tdelta-2*rgdiff);

obl_shapedgradient("linear_ramp_down",rgdiff,dir_ro3*gdiff,
dir_pe3*gdiff,dir_ss3*gdiff,WAIT);

```

```

zero_all_gradients();

/* Third negative-TE period and diffusion gradient
*****/
    obl_shapedgradient("linear_ramp_up",rgdiff,-
dir_ro3*gdiff,-dir_pe3*gdiff,-dir_ss3*gdiff,WAIT);
    delay(tdelta-2*rgdiff);
    obl_shapedgradient("linear_ramp_down",rgdiff,-
dir_ro3*gdiff,-dir_pe3*gdiff,-dir_ss3*gdiff,WAIT);
    zero_all_gradients();

    delay(0.00001);

/* Acquire echo
*****/
}

```

Vita

Emir Osmanagić

- Date of Birth** March 31, 1970
- Place of Birth** Sarajevo, Bosnia
- Degrees** Ph.D., Mallinckrodt Institute of Radiology, School of Medicine, Electrical and Systems Engineering, School of Applied Science, Washington University, St. Louis, August 2011
- M.Sc., Electrical and Systems Engineering, School of Applied Science, Washington University, St. Louis, May 2001
- B.Sc., Electrical Engineering, School of Applied Science, Washington University, St. Louis, May 1997
- Affiliations** Student Member of ISMRM
- Licenses** Professional Engineer in the State of Missouri
- Teaching**
- | | |
|-------------------------------------|-----------|
| Introduction to Electrical Circuits | 2002-2004 |
| Microelectronics | 2004-2006 |
| Introduction to Electrical Circuits | 2007 |
| Engineering Mathematics | 2008-2011 |
- Publications**
- Wang, W., Nguyen, N.M., Yablonskiy, D.A., Sukstanskii, A.L., Osmanagic, E., Atkinson, J.J., Conradi, M.S., and Woods, J.C. Imaging lung microstructure in mice with hyperpolarized ^3He diffusion MRI. *Magn Reson Med* 65: 620-626, 2011
- Osmanagic, E., Sukstanskii, A.L., Quirk, J.D., Woods, J.C., Pierce, R.A., Conradi, M.S., Weibel, E.R., and Yablonskiy, D.A. Quantitative assessment of lung microstructure in healthy mice using an MR-based ^3He lung morphometry technique. *J Appl Physiol* 109: 1592-1599, 2010

Osmanagic, E., Sukstanskii, A.L., Quirk, J.D., Woods, J.C., Conradi, and Yablonskiy, D.A. Anisotropic Nature of ³He Gas Diffusion in Mice Lungs. Conference of ISMRM, 2010

Osmanagic, E., Wood, D., Kilpatrick, F.B., VanSant, A.K. Parallel Affinity Chromatography Device, Software, Hardware and Operation. Journal of Laboratory Automation, 2002

Osmanagic, E., Kilpatrick, F.B., VanSant, A.K. Protein Purification and Extraction using Magnetic Beads vs. Custom Built 24-probe Sonication Device. Journal of Laboratory Automation, 2003

Employment	Biotechnology LIMS Lead	Monsanto Inc.	2009-2011
	Director of Engineering	Virbac AH	2007-2008
	Associate Technical Director	Pfizer Inc.	2003-2007
	Senior Automation Manager	Monsanto Inc.	2000-2003
	Instrumentation Engineer	Monsanto Inc.	1997-2000

August 2011